

**TRIBOLOGICAL CHARACTERIZATION OF ROLES OF NANOPARTICLES
IN LUBRICATION**

A Dissertation

by

WEI DAI

Submitted to the Office of Graduate and Professional Studies of
Texas A&M University
in partial fulfillment of the requirements for the degree of

DOCTOR OF PHILOSOPHY

Chair of Committee,	Hong Liang
Committee Members,	Alan Palazzolo
	Timothy J. Jacobs
	Philip R. Hemmer
Head of Department,	Andreas A. Polycarpou

December 2017

Major Subject: Mechanical Engineering

Copyright 2017 Wei Dai

ABSTRACT

This research investigates the tribological performance and rheological properties of nanoparticles as lubricant additives. Experimental approach combined with analysis were used to study the chemical and physical interactions between nanoparticles and lubricating system. Three areas of investigation were carried out as summarized in the following.

Tribological performance and rheological properties of α -ZrP ($\text{Zr}(\text{HPO}_4)_2 \cdot \text{H}_2\text{O}$) and V_2O_5 nanoparticles were investigated as lubricant additives. α -ZrP showed 50% reduction in friction and 30% in wear compared to the conventional additives ZDDP. Spectroscopic characterization indicated that the tribofilm consists of iron oxide, zirconium oxide, and zirconium phosphates. Through Raman spectrum and EDS analysis, it was found that V_2O_5 involved tribochemical reaction during rubbing. Vanadium intermetallic alloy (V-Fe-Cr) was found to enhance the antiwear performance. This research revealed that nanoparticles could be effective additives to improve tribological performance.

Tribofilms play vital roles in protecting lubricated surfaces in mechanical systems in motion. Strategically-selected-illuminative nanoparticles of NaYF_4 were added to a base oil in order to enable their tracking. Electrical conductivity was monitored during sliding that was found to be linked to the state of the interface and the tribofilm. This work discovered three stages to form a tribofilm: running in, reactive, and growth. Interestingly, the formation of a tribofilm was more dominated by frictional

force than applied load. This is significant because we can now use alternative strategies to generate quality tribofilms.

For the lubricating dynamics, the physical interaction between the nanoparticles and lubricating systems were investigated. Mechanisms of interfacial interaction between the shark skin and water have yet to be fully understood. In the present research, diamond particles worked as tracking particles in fluid. The shark-skinned surface with 90 degree orientation scale showed a more uniform distribution of diamond particles, which indicated to a lower gradient of velocity. Less momentum transfer between adjacent layers of fluid leads to a lower drag. Eventually, a viscosity map of shark-skinned surface with different scale orientation was created. It will facilitate the design of shark-skinned surface with better performance. The understanding generated in this study could be used as guideline for future study in surface design and texturing.

DEDICATION

To my beloved family.

ACKNOWLEDGEMENTS

I would like to express the deepest appreciation to my advisor, Dr. Hong Liang, for her guidance, consistent support and encouragement. She inspired my creativity and taught me to think critically. Many thanks also go to my committee members, Dr. Palazzolo, Dr. Jacobs, and Dr. Hemmer, for their sights and support throughout this research.

I am grateful to the financial support from Texas A&M University, Texas Engineering Experiment Station, Turbomachinery Laboratory, Shell Technology Center and Cameron.

I would also like to thank all the members of Surface Science Group for their assistance and suggestions: Dr. Huaping Xiao, Dr. Sunghan Kim, Dr. Hyunho Choi, Dr. Carlos Sanchez, Kyungjun Lee, Yunyun Chen, Lian Ma, Eugene Chen, and Yuan Yue.

Thanks also go to the department faculty and staff for making my time at Texas A&M University a great experience.

Finally, I would like to thank my parents for their support and to my wife for her patience and love.

CONTRIBUTORS AND FUNDING SOURCES

Contributors

Part 1, faculty committee recognition

This work was supervised by a dissertation committee consisting of Professor Hong Liang, Alan Palazzolo and Timothy Jacobs of the Department of Mechanical Engineering and Professor Philip Hemmer of the Department of Electrical Engineering.

Part 2, student/collaborator contributions

The materials NaYF₄ for Chapter V was provided by Yunyun Chen of the Department of Materials Science. The materials and characterization for Chapter VI was provided by Masfer Alkahtani of the Department of Physics. Raman characterization for Chapter III was provided by Alexander Sinyukov of the Department of Physics. Part of the tribotest and AFM were provided by Kyungjun Lee and Lian Ma of the Department of Mechanical Engineering.

All other work conducted for the dissertation was completed by the student under the advisement of Professor Hong Liang of Department of Mechanical Engineering.

Funding Sources Section

Graduate study was supported by a scholarship from Texas A&M University and the Gamechanger Project from Shell Technology Center.

TABLE OF CONTENTS

	Page
ABSTRACT	ii
DEDICATION	iv
ACKNOWLEDGEMENTS	v
CONTRIBUTORS AND FUNDING SOURCES.....	vi
TABLE OF CONTENTS	vii
LIST OF FIGURES.....	x
LIST OF TABLES	xiv
CHAPTER I INTRODUCTION	1
1.1 Conventional Liquid Lubricants	1
1.1.1 Components of liquid lubricants	2
1.1.2 Chemical Structures of Additives.....	5
1.2 Novel Nano Lubricants	21
1.2.1 Effects of chemical composition of nanoparticles on lubricating performance.....	25
1.2.2 Effects of particle size	35
1.2.3 Effects of morphology of nanoparticles	37
1.3 Performance characteristics of lubricants	43
CHAPTER II MOTIVATIONS AND OBJECTIVES.....	48
2.1 Tribological performance and rheological properties of nanoparticles	49
2.2 Investigation of lubricating kinetics	49
2.3 Investigation of lubricating dynamics	49
CHAPTER III MATERIALS AND METHODS.....	51
3.1 Materials.....	51
3.1.1 Synthesis of α -ZrP.....	51

3.1.2 Synthesis of V ₂ O ₅	52
3.1.3 Fabrication of Shark-skin-like surface	54
3.2 Tribological evaluation	56
3.2.1 Tribological evaluation of α -ZrP.....	56
3.2.2 Tribological evaluation of V ₂ O ₅	56
3.2.3 Tribological evaluation of NaYF ₄	57
3.3 Rheological evaluation.....	58
3.3.1 Rheological evaluation of nanoparticles	58
3.3.2 Rheological evaluation of shark-skin-like surface	58
3.4 Methods of lubricating kinetics and dynamics.....	60
3.4.1 Wear track characterization.....	60
3.4.2 Lubrication kinetics.....	61
3.4.3 Lubrication dynamics	62
CHAPTER IV TRIBOLOGICAL PERFORMANCES AND MECHANISMS OF LUBRICATION USING NANOPARTICLES AS ADDITIVES	64
4.1 Roles of α -ZrP in oil lubrication	64
4.1.1 Friction reduction	69
4.1.2 Wear Reduction.....	71
4.1.3 Lubricating mechanisms.....	73
4.2 Roles of V ₂ O ₅ in oil lubrication	78
4.2.1 Friction reduction	79
4.2.2 Wear Reduction.....	82
4.2.3 Mechanisms.....	85
4.3 Summary	93
CHAPTER V IN SITU CHARACTERIZATION OF NANOPARTICLE- ENHANCED GROWTH OF TRIBOFILMS	95
5.1 Tribofilm formation.....	95
5.2 The performance of a tribofilm	97
5.2.1 Friction reduction	97
5.2.2 Wear reduction	100
5.2.3 Sliding-induced redistribution of nanoparticles	102
5.3 Tribochemical interaction	104
5.4 Kinetics of tribofilm formation	107
5.5 Summary	115
CHAPTER VI MECHANISMS OF FLUID-DRAG REDUCTION VIA 3D- PRINTED SHARK SKINS	117
6.1 Morphological characteristics	117
6.2 Fluidic performance	119
6.3 The mechanism of drag reduction.....	121

6.4 Summary	130
CHAPTER VII CONCLUSION AND RECOMMENDATION	131
7.1 Conclusion.....	131
7.2 Future Recommendation	134
REFERENCES.....	135

LIST OF FIGURES

	Page
Figure 1.1 Types of mineral oils: (a) straight paraffin, (b) branched paraffin, (c) naphthene and (d) aromatic	3
Figure 1.2 Statistics of nanoparticles worked as lubricant additives	27
Figure 1.3 The formation of adsorption layer using MoS ₂ nanoparticles (Adapted from (88)).....	29
Figure 1.4 Tribological performance comparison based on different chemical composition: (a) MFC (b) MFR (c) MWR	33
Figure 1.5 Schematic transmission processes of nanoparticles with different size (Adapted from (63)).....	36
Figure 1.6 Tribological performance of nanopartilces with different size: (a) MFC, (b) MFR, (c) MWR	37
Figure 1.7 Statistics of the nanoparticles morphology	38
Figure 1.8 Tribological performances of nanoparticles with different morphology	39
Figure 1.9 The three main friction mechanisms of multilayered IF NP (redraw from (131)): (A) sliding(133), (B) rolling(134), (C) exfoliation(135, 136)	41
Figure 1.10 A typical setup of Ostwald viscometer	45
Figure 1.11 The typical setup of rheometer: (a) concentric cylinders (b) cone and plate (c) parallel plate	45
Figure 1.12 A typical Stribeck curve	47
Figure 2.1 Research flow chart	48
Figure 3.1 TEM images of sheet like V ₂ O ₅	53
Figure 3.2 Raman spectrum of sheet like V ₂ O ₅	53
Figure 3.3 Design and dimensions of shark-skin-like surface: single scale of sharkskin: (a) a simplified model of shark-skinned surface (b) a smooth surface for comparison (c) a textured surfaces with parallel shark-skin scale orientation (0 degree) (d) a textured surface with shark skin mix scale	

orientation (45 degree) (e) a textured surfaces with perpendicular shark-skin scale orientation (90 degree).....	55
Figure 3.4 The schematic illustration of the rheometer.....	58
Figure 3.5 A new design of surface viscosity measurement.....	60
Figure 3.6 The setup of the contact resistance measurement.....	61
Figure 3.7 Setup of a home-made confocal laser scanning microscope.....	63
Figure 4.1 Friction coefficient changing with sliding distance.....	70
Figure 4.2 Optical image of wear scar and wear track: (a) (d) base oil; (b) (e) base oil + ZDDP; (c) (f) base oil + α -ZrP.....	71
Figure 4.3 SEM image of wear track: (a) base oil, (b) base oil + ZDDP, (c) base oil + α -ZrP.....	72
Figure 4.4 Volume of wear track.....	73
Figure 4.5 AFM height images, phase images and linear scan profiles of the wear track: (a)(d)(g) base oil; (b)(e)(h) base oil + ZDDP; (c)(f)(i) base oil + α -ZrP.....	75
Figure 4.6 XPS spectrum of base oil + α -ZrP wear track. (a) C 1s, (b) O 1s, (c) Fe 2p, (d) Zr 3d and (e) P 2p.....	76
Figure 4.7 Schematic tribofilm composition of ZDDP and α -ZrP.....	77
Figure 4.8 Stribeck curve of light mineral oil samples with different concentration V_2O_5	82
Figure 4.9 Surface morphology and profile of wear tracks from different (a) light mineral oil (b) light mineral oil with 0.05 wt% V_2O_5 (c) light mineral oil with 0.1 wt% V_2O_5 (d) light mineral oil with 0.2 wt% V_2O_5	84
Figure 4.10 Volume of wear tracks from light mineral oil with different V_2O_5 concentrations.....	85
Figure 4.11 Raman Spectrum of wear tracks from different samples.....	86
Figure 4.12 Deconvolution results of Raman spectrum from different wear tracks: (a) Base oil, (b) Base oil + 0.05 wt% V_2O_5 , (c) Base oil + 0.1 wt% V_2O_5 (d) Base oil + 0.2 wt% V_2O_5	89

Figure 4.13 EDS scan area of wear track from Base oil + 0.2 wt% V ₂ O ₅	91
Figure 4.14 EDS spectrum of wear track from Base oil + 0.2 wt% V ₂ O ₅	91
Figure 4.15 Illustration of the lubricating mechanism of V ₂ O ₅	93
Figure 5.1 Friction coefficient and contact resistance change during the sliding process: (a) base oil (b) base oil + 1 wt% NaYF ₄	97
Figure 5.2 Correlation between the friction coefficient and contact resistance: (a) base oil (b) base oil + 1 wt% NaYF ₄	99
Figure 5.3 SEM images and cross section profile of wear track from samples with different NaYF ₄ concentration. (a) base oil (d) base oil + 0.3 wt% NaYF ₄ (g) base oil + 0.6 wt% NaYF ₄ (j) base oil + 1 wt% NaYF ₄ . (b)(e)(h)(k) and (c)(f)(i)(l) show the center and edge images of the corresponding wear tracks under higher magnification.	101
Figure 5.4 The wear volume of wear tracks of base oil containing NaYF ₄ with various concentrations.	102
Figure 5.5 Confocal scanning microscope images of wear track of base oil + 1 wt% NaYF ₄ after different sliding distance: (a) 0 h (b) 0.5 h (c) 3 h.	103
Figure 5.6 EDS spectrum of wear track of base oil + 1 wt% NaYF ₄ (a) SEM image of wear track (b) EDS spectrum.....	104
Figure 5.7 Raman spectrum of the wear track (a) deconvolution of base oil wear track spectrum (b) deconvolution of base oil + 1 wt% NaYF ₄ wear track spectrum (c) wear track spectrum of base oil after sliding for 0.5h, 1h, 2h and 3h (d) wear track spectrum of base oil +1 wt% NaYF ₄ after sliding for 0.5h, 1h, 2h and 3h.....	105
Figure 5.8 NaYF ₄ derived tribochemical reaction rate as a function of input mechanical power.	110
Figure 5.9 The formation and removal of tribofilm in the reactive regime	111
Figure 5.10 NaYF ₄ contact pressure and shear stress as a function of sliding time. (b) NaYF ₄ 3D plot of contact pressure, shear stress and reaction rate changing with sliding time.	113
Figure 5.11 Illustration of three periods during the sliding process: (a) Running in stage: contact resistance < 1 Ω (b) Reactive stage: 1 Ω < contact resistance < 100 Ω (c) Growing stage: contact resistance > 100 Ω.....	115

Figure 6.1 3D printed shark-skinned surfaces with different scale orientation: (a) smooth, (b) parallel (0 degree), (c) mix (45 degree), and (d) perpendicular (90 degree).....	119
Figure 6.2 Viscosity of water flowing over different shark-skinned surfaces under different shear rate	121
Figure 6.3 Diamond particle distribution on shark-skinned surface with different scale orientation after the viscosity test under 400 s^{-1} : (a) smooth, (b) parallel (0 degree), (c) mix (45 degree), and (d) perpendicular (90 degree).....	123
Figure 6.4 3D diamond particles distribution on textured surface with different shark skin orientation after the viscosity test under 400 s^{-1} : (a) smooth, (b) parallel (0 degree), (c) mix (45 degree), and (d) perpendicular (90 degree) ..	124
Figure 6.5 Line scan profile of diamond particle distribution on surfaces with different scale orientation after the viscosity test under 400 s^{-1}	125
Figure 6.6 Diamond particle distribution uniformity comparison of textured surface with different shark skin orientation after the viscosity test under 400 s^{-1} : (a) smooth, (b) parallel (0 degree), (c) mix (45 degree), and (d) perpendicular (90 degree).....	126
Figure 6.7 The viscosity reduction effect of shark-skinned surface compared with smooth surface under various S^+ number: (a) parallel, (b) mix and (c) perpendicular.	128
Figure 6.8 The viscosity map of shark-skinned surface with different shark skin orientation (from 0 degree to 180 degree)	129

LIST OF TABLES

	Page
Table 1.1 Examples and molecular structures of synthetic oil.....	4
Table 1.2 Examples and molecular structures of friction modifiers	7
Table 1.3 Examples and molecular structures of anti-wear additives.....	8
Table 1.4 Examples and molecular structures of viscosity modifiers.....	10
Table 1.5 Examples and molecular structures of corrosion inhibitors	12
Table 1.6 Examples and molecular structures of oxidation inhibitors	14
Table 1.7 Examples and molecular structures of pour point depressants	16
Table 1.8 Examples and molecular structures of dispersants.....	18
Table 1.9 Examples and molecular structures of detergents	21
Table 1.10 Summary of nanolubricant additives	24
Table 1.11 Different types of nanoparticles as lubricant additives	26
Table 1.12 Summary of lubrication mechanisms of nanocomposites.....	30
Table 1.13 Summary of lubrication mechanisms of metallic nanoparticles	31
Table 1.14 metal oxides and mechanisms of lubrication	32
Table 1.15 Rare earth compounds and the associated lubrication mechanism	32
Table 1.16 Correlations between chemical composition and tribological performance ..	35
Table 1.17 Correlations between size and tribological performance	37
Table 1.18 Correlations between morphology and tribological performance.....	43
Table 1.19 Correlations between aspect ratio and tribological performance	43
Table 4.1 Properties of tribofilm formed by different additives	66
Table 4.2 Surface roughness parameters of the wear track.	74

Table 4.3 Raman spectrum Peak position comparison of literature and current research	89
---	----

CHAPTER I

INTRODUCTION¹

This chapter provides the background information and basic knowledge related to this research. Firstly, a review of conventional liquid lubricants and their additives was conducted. Secondly, introduction to nanoparticles as novel lubricant additives was introduced. Finally, properties of lubricants and basics of lubrication were briefly introduced.

1.1 Conventional Liquid Lubricants

The function of lubricants is to control the friction and wear in a lubricating system containing machine elements such as gears and bearings. Lubricants are also used to prevent corrosion and to scavenge heat, dirt, and wear debris. In addition, they are used to transfer force or energy in hydraulic systems. Selection of an appropriate lubricant depends on factors include cost, environment, health, safety, system needs, and others. For a given mechanical system, minimizing the number of lubricants used generally simplifies maintenance and reduces the chances of applying the wrong lubricant. Inventory storage and handling are also reduced. This article discusses about

¹ Part of this chapter is reproduced by permission from “Roles of nanoparticles in oil lubrication” by Wei Dai, Bassem Kheireddin, Hong Gao, and Hong Liang. *Tribology International*, 102 (2016): 88-98. (Copyright © 2016 Elsevier, all rights reserved); and from ASM Handbook, Volume 18: *Friction, Lubrication, and Wear Technology* by Wei Dai and Hong Liang. (Copyright © 2017 ASM International, all rights reserved)

the basic properties of lubricants in order to assist scientists and engineers to gain knowledge and understand principles behind selection of lubricants.

1.1.1 Components of liquid lubricants

Liquid lubricants are primarily composed of a base oil (90 ~95%) and additives (5~10%). The majority of a base oil is hydrocarbons that provides the physical properties of lubricants. Additives provide the chemical and tribological characteristics of lubricants. Base oils include mineral oil and synthetic oil. Mineral oil is distilled and refined from the crude oil. It is inexpensive and widely applied in industry. Synthetic oil is artificially fabricated aiming improved performance. Based on their chemical composition and process history, base oil has two basic categories, mineral oil (crude oil based) and synthetic oil. They are applied to unique working conditions.

1.1.1.1 Mineral oil

Mineral oil works under moderate temperatures. The chemical composition of mineral oil is complex and it could not be described by a certain formula. However, they can be classified from molecular structure which contained straight chains and cyclic carbon chains. Based on their majority chemical forms, types of mineral oil are threefold: paraffinic, naphthenic and aromatic, as shown in Figure 1.1 [1]. Paraffinic oil shows straight or branched long chain hydrocarbons. Naphthenic oil includes cyclic hydrocarbon structure without any unsaturated bonds. Aromatic oil contained benzene

ring structure. The type of mineral oil will determine their physical properties, such as viscosity-temperature and viscosity-pressure relationship.

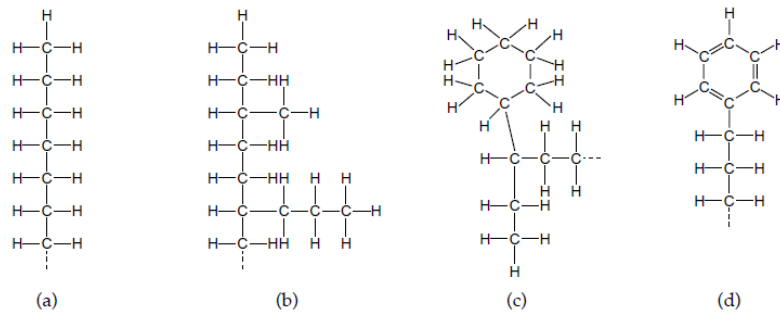


Figure 1.1 Types of mineral oils: (a) straight paraffin, (b) branched paraffin, (c) naphthene and (d) aromatic

1.1.1.2 Synthetic oil

Synthetic oil is designed to work under extreme conditions (very high or very low temperatures) or significantly improve the tribological performance under moderate conditions. Synthetic oil has several types based on their molecular structure as shown in Table 1.1. Esters are products of reaction between alcohol and acid. Due to the strong bonds among esters, they are more stable than ordinary hydrocarbons under the elevated temperature (200~250°C). Ester lubricants primarily contained diester, silicate ester, polyglycol ester[2], fluoro ester, neopentyl polyol ester[3] and aliphatic ester[4]. Due to their high thermal stability and oxidation resistance, they mainly worked as hydraulic fluid in aircraft and gas turbine industry. Synthetic cycloaliphatic hydrocarbons worked as traction lubricants under extreme environment. They possess very high viscosity under high contact pressure or high shear and mainly applied in machining and textile

industry. Polyglycol possesses very high oxidation stability, which makes it to be an ideal lubricant for components working under elevated temperature. Another advantage of polyglycols is no stain effect, which is suitable for textile industry. Silicones are chemically inert, which leads to high thermal stability and anti-oxidation property. Therefore they can working under extremely temperature while other lubricants fail to do. Low load carrying capability under thin film lubrication is a disadvantage. Organohalogens have high anti oxidation property and are employed under a wide temperature range. Cost of organohalogens are much higher than others. They are mainly applied in computer head-disk.

Table 1.1 Examples and molecular structures of synthetic oil

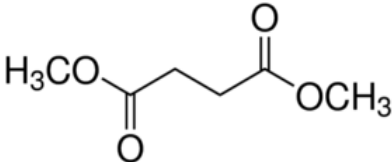
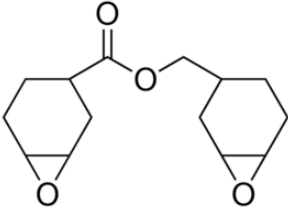
Category	Example	Molecular Structure
esters	DBE-4 dibasic ester	 <chem>COC(=O)CCCCCCCC(=O)OC</chem>
cycloaliphatic	3,4-epoxycyclohexylmethyl 3,4-epoxycyclohexanecarboxylate	 <chem>COC(=O)C1CC2OC2CC1C3CC4OC4CC3</chem>

Table 1.1 Continued.

polyglycols	Poly(ethylene glycol) bis(carboxymethyl) ether	
silicones	Silicone oil	
organohalogens	Chlorofluorocarbons	

1.1.2 Chemical Structures of Additives

There are many reports about additives used to improve properties and performance of lubricants[5, 6]. Common additives are, anti-wear additives, corrosion inhibitor, detergents and dispersants, friction modifier, oxidation inhibitor, pour point depressants, viscosity modifier, among many others. Basically, those additives can be categorized into five types: anti-wear, deposit control, film-forming, miscellaneous, and viscosity modification. There are variety of additives into each categories. For example, the deposit control includes antioxidants (e.g. amine and phenol derivatives, copper and boron antioxidants, sulfur and phosphorus compounds), metal salts of organic acids, metal-free dispersants, and zinc dithiophosphate. These additives make lubricants to

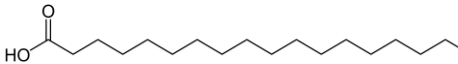
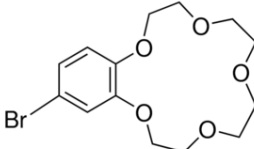
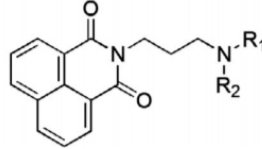
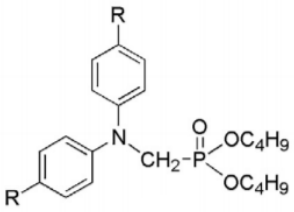
work cleaner through preventing precipitates from oxidation, wear, and other friction-induced reactions [6]. Below lists a few widely used ones.

1.1.2.1 Friction modifier

Friction modifier is the type of additives to reduce friction. Friction modifiers include organic, for example, amides, carboxylic acids, crown ethers, imides, phosphoric acid, and their derivatives. They can be used to form a film, dry or wet, to reduce friction. Table 1.2 shows example and molecular structures of friction modifiers. Most friction modifiers are long-chain molecules with a polar end group and a nonpolar hydrocarbon chain. The polar end group physically adsorbs itself on the metal surface, whereas the hydrocarbon chain increases the strength of lubricant film through association. Friction modifiers have a finite life related to their oxidative and thermal stability. Friction modifiers are commonly used in gasoline engine oils, automatic transmission fluids, tractor hydraulic fluids, power steering fluids, shock absorber fluids, and metalworking fluids. In passenger car applications with federal government mandated fuel economy, the lubricant suppliers use these additives as a competitive marketing tool. In automatic transmission fluids and limited slip axle lubricants, friction modifiers are used to control torque application through clutch and band engagements. Fatty acid derivatives are the most commonly used friction modifiers. In the case of fatty alcohol and fatty acid families, the friction-modifying properties are a function of the length and nature of the hydrocarbon chain and the nature of the functional group. Long and linear-chain materials are better friction modifiers than

short and branched chain materials. Fatty acids are better than fatty amides, which in turn are better than fatty alcohols. Saturated acids that contain a 13 to 18 carbon chain are generally preferred.

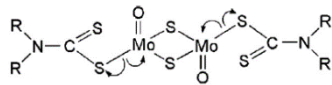
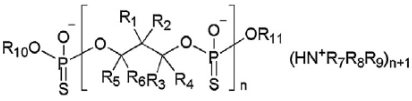
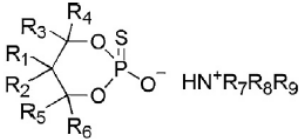
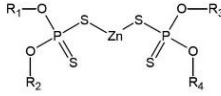
Table 1.2 Examples and molecular structures of friction modifiers

Category	Example	Molecular structure
amides	Fatty acid amide[7]	$R_1-(CH_2)_n-C(=O)-NH_2$
fatty acids	Stearic acid	
crowns ethers	bromobenzo-15-crown-5[8]	
imides	Aromatic imides[9]	
phosphonic acid	Phosphonic acid derivatives[10]	

1.1.2.2 Anti-wear additives

Anti-wear additives are used to prevent asperity seizure, in particular under extreme-pressure. Organosulfur, organo-phosphorus, sulfur-nitrogen, and phosphorus-nitrogen compounds can form an interfacial layer with shear strength[11, 12]. In addition, the lubricating process often faces problems like grease stringiness, lubricant adherence, fluid leakage, surface adsorption, and corrosion. Miscellaneous additives are thus added to resolve the problems. They are tackifiers[13], antimisting agents[14], seal swelling agents[15], antimicrobial chemical[5, 6], surfactants[16], and corrosion inhibitors[17, 18].

Table 1.3 Examples and molecular structures of anti-wear additives

Category	Example	Molecular structure
Organosulfur	MoDTC	
organo-phosphorus	Phosphorus based additives[19]	
phosphorus-nitrogen compounds	amine salts of thiophosphoric acids[20]	
Dithiophosphoric acid derivatives	ZDDP	

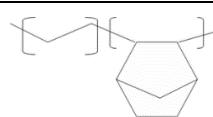
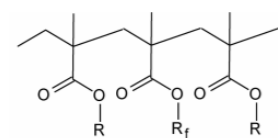
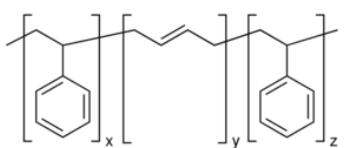
They are primarily used in gasoline and diesel engine oils and in industrial lubricants. Table 1.3 shows example and molecular structures of anti-wear additives. Antiwear agents are commonly used in engine oils, automatic transmission fluids, power steering fluids, and tractor hydraulic fluids. In gasoline engine oils, the ASTM sequence IIIE and VE engine tests are used to determine the effectiveness of antiwear additives. The general effectiveness of these additives in metalworking fluids is determined by the use of Timken, fourball, and Falex tests.

1.1.2.3 Viscosity modifiers

Viscosity modifiers are primarily used in multigrade engine oils, gear oils, automatic transmission fluids, power steering fluids, greases and some hydraulic fluids. Mineral oils, which are effective lubricants at low temperatures, become less effective lubricants at high temperatures. At high temperatures, their film-forming ability (in the hydrodynamic lubrication regime) diminishes, because of a drop in viscosity. Prior to the use of viscosity improvers and the introduction of multigrade oils, this problem was partly overcome through seasonal oil changes. The principal function of a viscosity improver is to minimize viscosity variations with temperature. Viscosity modifiers are typically added to a low-viscosity oil to improve its high-temperature lubricating characteristics. Olefin copolymers (OCP), polymethacrylates (PMA), hydrogenated styrene-diene (STD) polymers are the common types of viscosity modifiers used in modern lubricants. Table 1.4 shows example and molecular structures of viscosity modifiers. Thickening efficiency and shear stability are two important considerations

when selecting a polymer for use as a viscosity modifier. The thickening efficiency of a polymer is a direct function of its molecular weight. On an equal weight basis, a high molecular weight polymer provides higher viscosity than a low molecular weight polymer. Shear stability, the ability of the polymer to withstand the mechanical shearing forces encountered during use, is inversely related to its molecular weight; the lower the molecular weight, the higher the shear stability. A number of tests are available for measuring the viscosity-improving properties and the shear stability of polymers in a finished oil.

Table 1.4 Examples and molecular structures of viscosity modifiers

Category	Example	Molecular structure
Olefin copolymers	Cyclic olefin copolymer	
polymethacrylates	General structure of functionalized PMA copolymer[21]	
hydrogenated styrene-diene	Hydrogenated polystyrene-co-butadiene[22]	

1.1.2.4 Corrosion inhibitors

Rust and corrosion represent the damage done to metal surfaces by the attack of atmospheric oxygen and acidic products. The rust and corrosion rate, which is usually low, increases greatly in the presence of water and polar impurities. Internal combustion engines contain all the elements necessary to promote these types of surface damage. Air is entrained in the oil and fuel, and water and organic acids form during the combustion and decomposition processes. Rust and corrosion inhibitors provide a barrier between the metal surface and these harmful elements. These inhibitors are of two types: those that neutralize acids and those that form protective films. The film formers attach themselves strongly to the metal surface and form an impenetrable protective film. The film formation can occur through either physical adsorption or chemical reaction. The first mechanism involves the formation of densely packed protective layers of a somewhat transient nature and the second, a more permanent protective film resulting from a chemical reaction between the inhibitor and the metal surface. Long-chain amines, basic sulfonates, carboxylic acid derivatives, and thiadiazole and triazole derivatives are the most commonly used rust and corrosion inhibitor types. Table 1.5 shows the examples and molecular structures of corrosion inhibitors. These additives have major uses in engine oils, gear oils, metalworking fluids, and greases. Thiadiazole and triazole derivatives are especially useful in protecting against nonferrous or yellow metal corrosion. A number of ASTM-specified tests are used for hydraulic and metalworking fluids. For engine oils, the ASTM sequence engine test is used to assess the corrosion-inhibiting ability of the lubricant.

Table 1.5 Examples and molecular structures of corrosion inhibitors

Category	Example	Molecular structure
Long chain amines	Poly(ethylene glycol) diamine	
carboxylic acid derivatives	Alkenylsuccinic acid	
sulfonates	Calcium dodecylbenzene sulfonate	
Thiadiazole derivatives	3-anilino-5-imino-4- phenyl-1,2,4- thiadiazoline[23]	

1.1.2.5 Oxidation inhibitor

All modern lubricants, by virtue of being hydrocarbon based, are susceptible to oxidation[24, 25]. Each type of base stock (mineral or synthetic) has a stable threshold, beyond which stabilizers or oxidation inhibitors are needed to retard oxidation. Adequately refined base oils contain some sulfur- and nitrogen-base "natural" inhibitors. Under mild conditions, these inhibitors are sufficient to protect lubricants

against oxidation. However, most modern uses require supplemental inhibitors to protect lubricants under increasingly hostile conditions. An increase in temperature affects the oxidation process most profoundly, with the rates of oxidation approximately doubling with every 10-degree rise in temperature. Wear metals can further enhance the rate of oxidation [26]. If this process is not controlled, the lubricant decomposition will lead to oil thickening, sludge formation, and the formation of varnish, resin, and corrosive acids [27, 28]. Oxidation inhibitors can be classified as hydroperoxide decomposers and radical scavengers, depending on the mode of their controlling action. Sulfur- and phosphorus-containing inhibitors, such as sulfides, dithiocarbamates, phosphites, and dithiophosphates, act as hydroperoxide decomposers. Nitrogen- and oxygen-containing inhibitors, such as arylamines and phenols, act as radical scavengers [24, 25]. Table 1.6 shows example and molecular structures of oxidation inhibitors. Oxidation inhibitors are used in almost all lubricants. Gasoline and diesel engine oils and automatic transmission fluids account for 60% of the total use. High operating temperature and high air exposure applications require a high level of oxidation protection. Zinc dialkyl dithiophosphates are the primary inhibitor type, followed by aromatic amines, sulfurized olefins, and phenols. A number of tests are used to assess the oxidation stability of a lubricant under conditions of accelerated oxidation. The ASTM sequence IIIE (viscosity increase), sequence VE (sludge and varnish formation), and CRC L-38 (bearing corrosion) tests are used for engine oils. The CRC L-60 test is used for gear oils, and ASTM D 943 and ASTM D 2272 tests are used for turbine oils.

Table 1.6 Examples and molecular structures of oxidation inhibitors

Category	Example	Molecular structure
Zinc dialkyl dithiophosphates	ZDDP	
aromatic amines	1-Naphthylamine	
sulfurized olefins	Saturated dialkyl polysulfides[29]	
phenols	4-aminophenol[30]	

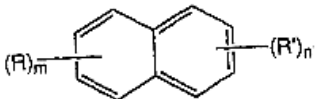
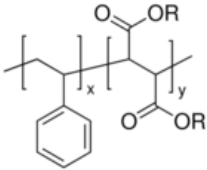
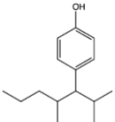
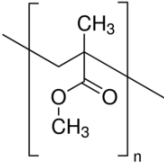
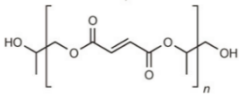
1.1.2.6 Pour point depressants

The pour point is the lowest temperature at which a fuel or an oil will pour when cooled under defined conditions. In general, the pour point is indicative of the amount of wax (straight-chain paraffins) in an oil. At low temperatures, wax tends to separate as crystals with a lattice-type structure. These crystals can trap a substantial amount of oil via association, inhibit oil flow, and ultimately hinder proper lubrication of the equipment. Base oil suppliers remove most of the wax during petroleum refining. However, complete dewaxing of the base oils is not practical because of process

limitations, economics, and the desirable presence of wax, which offers a high viscosity index character[31]. Additives called pour-point depressants are used to enable mineral oils to function efficiently at low temperatures. Current practice favors mild dewaxing in combination with the use of pour-point depressants. A good pour-point depressant can lower the pour point by as much as 40 °C (70 °F). These additives are commonly used in applications that require the use of mineral oil, usually below 0 °C (32 °F). Pour-point depressants have virtually no effect on either the temperature at which the wax crystals start to precipitate (cloud point) or the amount of wax that separates. They essentially act as wax-crystal modifiers and function by altering the crystal size. Most commercial pour-point depressants are organic polymers. Commercial pour-point depressants include alkylated bicyclic aromatics, styrene esters, polymethacrylates, polyfumarates, polyfumarates, oligomerized alkylphenols, dialkaryl esters of phthalic acid, ethylene- vinyl acetate copolymers, and other mixed hydrocarbon polymers. Polymethacrylates and polyfumarates are the most commonly used chemical types. Table 1.7 shows example and molecular structures of pour point depressants. High molecular weight polymethacrylate derivatives can act both as viscosity modifiers and pour-point depressants. When this chemistry is used for viscosity improvement, the need for a pour-point depressant is minimized. Pour-point depressants are used at treatment levels of 1 % or lower. In nearly all cases, there is an optimum concentration above and below which the pour-point depressants become less effective. Pour-point depressants are used in crankcase engine oils, automatic and power transmission fluids, automotive gear oils, tractor fluids, hydraulic fluids, and circulating oils. The

performance of a pour-point depressant is determined in each base stock by using one or more of the following tests: ASTM D 97, pour point of petroleum oil; ASTM 3829, borderline pumping; and ASTM D 2602, apparent viscosity at low temperature using cold-cranking simulation.

Table 1.7 Examples and molecular structures of pour point depressants

Category	Example	Molecular structure
alkylated bicyclic aromatics	Alkylnaphthalene[32]	
styrene esters	Poly(styrene-co-maleic acid), partial isobutyl ester	
alkylphenol	Nonylphenol	
Polymethacrylate	Poly(methyl methacrylate)	
polyfumarates	Poly(propylene fumarate)[33]	

1.1.2.7 Dispersants

Dispersants are additives that are used to suspend oil-insoluble resinous oxidation products and particulate contaminants in the bulk oil. By doing so, they minimize sludge formation, particulate-related abrasive wear, viscosity increase, and oxidation-related deposit formation. A dispersant molecule contains an oleophilic hydrocarbon moiety and a polar functional group. The polar group, usually oxygen- or nitrogen-based, attaches itself to the oxidation products and sludge particles, while the oleophilic hydrocarbon group keeps the particles suspended in oil [27]. The hydrocarbon radical is either oligomeric or polymeric, and is usually aliphatic in nature. It contains from 70 to 200 or more carbon atoms to ensure good oil solubility, with a polybutenyl alkyl group being the most commonly used hydrocarbon group. The chemical classes that are suitable for dispersants include alkenylsuccinimides, succinate esters, high molecular weight amines, mannich bases, and phosphonic acid derivatives. Commercially, polybutenylsuccinic acid derivatives are the most commonly used dispersant types. Table 1.8 shows the examples and molecular structures of dispersants. The dispersants are primarily used in gasoline engine oils, diesel (heavy-duty and railroad) engine oils, natural gas engine oils, and aviation piston engine oils. Dispersants are also used in automatic transmission fluids and gear lubricants. The gasoline and heavy-duty diesel engine oils account for 75 to 80% of the total dispersant use. Succinimide and succinate-ester (pentaerythritol esters of polyisobutenylsuccinic anhydride) types are used both in gasoline and diesel engine oils. High molecular weight amine are used in gasoline engine oils only. Succinimide dispersants also find use in

automatic transmission fluids, power steering fluids, and, on a limited basis, in gear oils. In gasoline and diesel engine oils, the effectiveness of a dispersant is assessed on the basis of its ability to disperse lamp black or used engine oil sludge in laboratory screen tests and its performance in various ASTM sequence dynamometer engine tests, as well as fleet testing.

Table 1.8 Examples and molecular structures of dispersants

Category	Example	Molecular structure
mannich	Polybutenylhydroxybenzyl-polyethylenepolyamine	
Phosphonic acid	Bis-hydroxypropyl phosphonate	
Succinimide	Succinimide	
Succinate-ester	Diethyl succinate	

1.1.2.8 Detergents

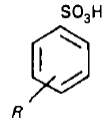
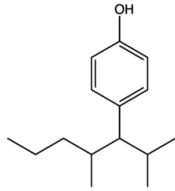
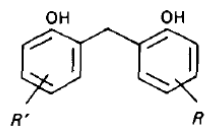
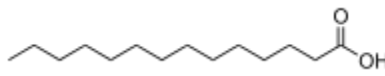
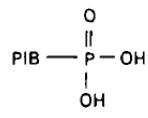
Detergents perform functions that are similar to those of dispersants.

Additionally, detergents neutralize acidic combustion and oxidation products, and hence,

control rust, corrosion, and resinous build-up in the engine. Detergents are metal salts of organic acids. The quantity of metal can either equal or exceed the stoichiometric amount necessary for complete neutralization of the acid function. When the metal is present in a stoichiometric amount, the detergents are referred to as neutral; when excess metal is present, they are referred to as either basic or overbased. Detergents are described chemically in terms of their soap content, the degree of overbasing, and the total base number (TBN), which is expressed as mg KOH/g of additive. The soap content refers to the amount of neutral salt and reflects cleaning ability, or detergency. The degree of overbasing describes the ratio of equivalents of metallic base to equivalents of acid substrate. The TBN of the detergent indicates its acid neutralizing ability. Detergents, like dispersants, contain a surface-active polar group and an oleophilic hydrocarbon radical with an appropriate number of carbon atoms to ensure good oil solubility. Metal sulfonates, phenates, carboxylates, salicylates, and phosphonates are common examples of the polar groups that are present in detergent molecules. Alkylbenzenesulfonic acids, alkylphenols, sulfur-coupled and methylene-coupled alkylphenols, carboxylic acids, and alkylphosphonic acids are the commonly used detergent substrates. Table 1.9 shows example and molecular structures of detergents. Basic detergents can be considered neutral detergents that contain the excess base in an associated form. Detergents are used in lubricants to keep oil insoluble by-products of combustion and oil oxidation in suspension. Depending on the end use of the lubricant, insoluble by-products can be coke, acidic decomposition products, or deposit forming resinous products[27, 28]. Detergents control the buildup of

these undesirable contaminants by keeping the equipment surfaces clean and by neutralizing the acidic products of lubricant oxidation and decomposition. They keep the equipment surfaces clean, both by forming a protective film on the metal surfaces through adsorption and by suspending the deposit-forming species in the bulk oil through association [31]. Detergents can act as oxidation inhibitors, depending on the nature of the functional group. For example, phenates, sulfurized phenates, and salicylates possess oxidation-inhibiting properties, presumably because of the presence of the phenolic functional group. Detergents are primarily used in crankcase lubricants. Gasoline and diesel engine oils account for over 75% of the total detergent consumption. Detergent treatment levels in engine lubricant formulations are fairly high; marine diesel engine lubricants contain the highest detergent concentrations. Marine engines use high-sulfur fuel, which leads to acidic combustion products (sulfuric acid) and, therefore, need the high base reserve in "basic" detergents for neutralization. Detergents have additional use in automatic transmission fluids and tractor hydraulic fluids. However, their use in these applications is not to control deposits, but to modify the frictional properties of the fluid.

Table 1.9 Examples and molecular structures of detergents

Category	Example	Molecular structure
Alkylbenzenesulfonic acids	Alkylbenzenesulfonic acid	
alkylphenols	Nonylphenol	
sulfur-coupled and methylene-coupled alkylphenols	Methylene-coupled alkylphenol	
carboxylic acids	Myristic acid	
alkylphosphonic acids	Polyisobutylenephosphonic acids	

1.2 Novel Nano Lubricants

In mechanical systems, consistent performance and energy saving demand eco-friendly and highly efficient lubricants. In today's market, 90% of lubricants are composed of hydrocarbon molecules and the rest are additives governing their behavior. For decades, organic phosphorous and sulfide compounds have played important roles in friction modification and wear resistance [34]. Lubrication mechanism stems from the physical and chemical interactions between lubricant molecules, material surfaces, and

environment. In recent years, nanoparticles have started to play more important roles as lubricant additives for their potential in emission reduction and improving fuel economy. Their characteristic size, normally less than 100 nm, will allow them to enter the contact region. In comparison with organic additives, nanoparticles are considered thermal stable at elevated temperatures that makes them favorable as lubricant additives.

There are some reports about lubrication mechanisms of nanolubricants. When nanoparticles were used as friction modifiers, they displayed four behaviors[34]: rolling of nanospheres[35-37]; tribofilm formation as results of tribochemical reactions[38-42]; mending effect because of the minimal size[43]; and polishing[44]. In addition, nanoparticles could be used as additives in diesel and biodiesel[45-48]. They were effective in improving fuel efficiency, engine performance, exhaust emission, combustion, and evaporation characteristics at different operating conditions. Moreover, nanorefrigerants were able to reduce energy consumption and enhance heat transfer rate[49-52].

The aforementioned reviews raised several questions: How can one optimize the tribological performance of nanolubricants? What are the characteristics of nanoparticles that are important to lubrication? Can we quantize their effects? During the review of literature of several hundreds of publications, we found that each study has been based on unique conditions, such as base stock, additive concentration, nanomaterials and their surface functionalization, workpiece materials, test parameters, lubrication regimes, etc, among many others. There is no one standard condition that can be used for fair comparison. The majority reports have been based on steel-steel contact. The non-steel

metals will not be the focus due to lack of statistically sufficient data to conduct a fair comparison. In order to make the best use of available data for better comparison and prediction, we applied the following strategy for this review study. First, frictional performance. We chose the minimum friction coefficient reached (MFC) and maximum friction reduction (MFR) in order to reveal fuel efficiency. Using such an approach the lubrication regimes from boundary to hydrodynamic will be discussed together. Second, wear performance. We selected the maximum wear reduction percentage (MWR) to exhibit anti-wear capability, regardless of the working conditions. In this case, most wear studies were conducted in the boundary and mixed lubrication regimes that we do not separate in order to maintain sufficient data for statistic analysis. Thirdly, statistic analysis was conducted based on the experimental results collected from about 70 papers that were related to nanolubricant additives, as listed in Table 1.10. Correlation between the parameters and performance was calculated using the JMP software. Using this approach, not only we could identify the key factors such as chemical composition and morphology to improve the tribological performance, but also we could establish a relationship between the key factors and lubrication mechanisms. In this study we defined morphological parameters as the molecular structure and shape of nanoparticles. In addition, we defined the size as a separate factor that belonged to the physical properties of nanoparticles. This review is more than a replenishment of the current knowledge. As a result, it substantially facilitates our fundamental understanding in nanolubrication that enables us to design nanolubricants with superior tribological performance.

Table 1.10 Summary of nanolubricant additives

Nanoparticle	Reference
Ag doped MoS ₂ nanoparticles	[53]
Ag nanoparticle	[54, 55]
Al ₂ O ₃	[56, 57]
Al ₂ O ₃ and CuO	[58]
Al ₂ O ₃ /SiO ₂ composite	[59]
Al ₂ O ₃ /TiO ₂ nanocomposites	[60]
Bismuth nanoparticles	[61]
BN	[62]
Calcium carbonate nanoparticles	[63]
CeO ₂	[64]
Cu	[65-69]
Cu nanoparticles in serpentine powders	[70]
Cu/SiO ₂ nanocomposites	[71]
CuO	[72]
CuO, TiO ₂ and nanodiamond	[73]
CuS	[74]
Diamond and SiO ₂	[75]
diamond nanoparticles	[76]
Fe, Cu, Co NPs	[77]
Fe ₃ O ₄ magnetic nps	[78]
fullerene-like MoS ₂ nanoparticles	[79]
graphene and MoS ₂ comparison	[80]
h-BN	[81]
hydroxides NPs (Mg/Al/Ce LDHs)	[82]
IF-MoS ₂ nanoparticles	[83, 84]
IF-WX ₂	[85]
La doped Mg/Al layered double hydroxide (LDH)	[86]
LaF ₃	[87]
MoS ₂	[88-92]
MoS ₂ and SiO ₂	[93]
Diamond and graphene	[94]
nano-Cu/graphene oxide composites	[95]
nano-PTFE	[96]
Ni	[97]
NiMoO ₂ S ₂	[98]
Ni based nanolubricants	[99]
OA/La-TiO ₂	[100]

Table 1.10 Summary of nanolubricant additives, continued.

Pd	[101]
Pd and Au nanoparticles	[102]
PTFE	[103, 104]
Rhenium doped MoS ₂	[105]
SA/CeBO ₃	[106]
serpentine ultrafine powders	[107]
serpentine, La(OH) ₃ and their composites	[108]
single wall carbon nanohorns (SWCNH) and TiO ₂	[109]
SiO ₂	[110]
Sn and Fe nanoparticles	[111]
TBP-LaF ₃	[112]
TiO ₂	[113-116]
TiO ₂ , CuO, Al ₂ O ₃ , MWNTs	[117]
Titanium nanoparticle	[118]
Zeolite	[119]
ZnAl ₂ O ₄	[120]
ZnO	[121]
ZnO and CuO	[122]
ZrO ₂	[123]
ZrP	[124]

1.2.1 Effects of chemical composition of nanoparticles on lubricating performance

Nanoparticles with various chemical compositions possess different chemical and physical properties, affecting the interaction between lubricants and surfaces. There are three questions to be answered. Which elements are favorable for nanolubrication? What are lubrication mechanisms of the specific element (the role it played) in each lubricating regime? How important is the chemical composition in determining a nanolubricant's tribological performance? As discussed earlier, we focus on three aspects, the minimum friction coefficient (MFC), maximum friction reduction (MFR)

and maximum wear reduction (MWR). Through this literature review and statistical correlation coefficient analysis, we aim to reveal insight from nanolubricants.

Based on the Table 1.10, we divided reported nanoparticles into seven types based on their characteristic chemical elements: carbon and its derivatives, metals, metal oxide, sulfides, rare earth compounds, nanocomposites and others. Detailed information about each category is listed in Table 1.11. For carbon and its derivatives, molecular structures (sheet, tube, onion) played a dominant role in determining their tribological behavior. The effects of carbon-containing additives would not be elaborated in this section. For metals and metal oxides, the majority elements were located in the transition metal group. For sulfides, the representative one was MoS₂, others included WS₂, CuS, and NiMoO₂S₂. For rare earth elements, Y, La, and Ce were considered as favorable elements for lubricant additives. For nanocomposites, they were the combinations of the aforementioned several categories. Others included CaCO₃, ZnAl₂O₄, Zeolite, ZrP, SiO₂, PTFE, Hydroxide, BN, serpentine, among others.

Table 1.11 Different types of nanoparticles as lubricant additives

Types	Nanoparticles
Carbon and its derivatives	Graphene, diamond, SWCNT, MWNTs
Metals	Sn, Fe, Bi, Cu, Ag, Ti, Ni, Co, Pd, Au
Metal oxide	ZrO ₂ , TiO ₂ , Fe ₃ O ₄ , Al ₂ O ₃ , ZnO, CuO
Sulfides	WS ₂ , CuS, MoS ₂ , NiMoO ₂ S ₂
Rare earth compounds	LaF ₃ , CeO ₂ , La(OH) ₃ , Y ₂ O ₃ , CeBO ₃
Nanocomposites	Cu/SiO ₂ , Cu/graphene oxide, Al ₂ O ₃ /SiO ₂ , serpentine/La(OH) ₃ , Al ₂ O ₃ /TiO ₂
Others	CaCO ₃ , ZnAl ₂ O ₄ , Zeolite, ZrP, SiO ₂ , PTFE, Hydroxide, BN, serpentine

Among all listed, some compounds were more popular than others. Based on all the literature we collected (in Table 1.10), the number of reports about one particularly type was plotted in a pie chart as shown in Figure 1.2. As seen that the majority of nanolubricants consisted of metal oxides, metals and sulfides. In order to elucidate the lubrication mechanism, we only discussed the correlation between the chemical elements and tribological behavior, irrespective of other nanoparticles characteristics, morphology wise. The correlation coefficient was calculated using JMP software. It measured the strength of the relationship between two parameters. A positive/negative correlation coefficient means that the two parameters are positively/negatively related. If the absolute value of correlation coefficient is close to 1, two parameters are strongly related. Conversely, if the absolute value of correlation coefficient is close to 0, two parameters weakly related.

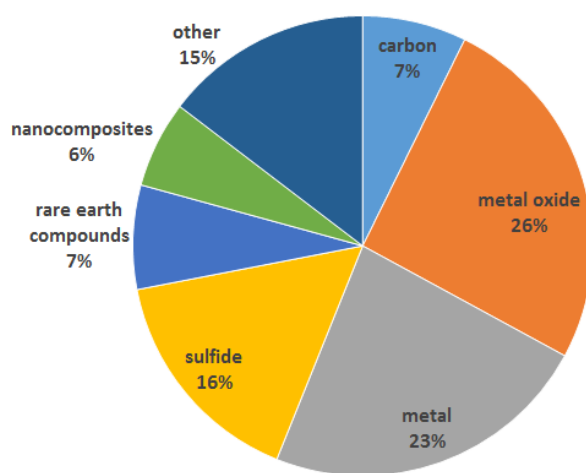


Figure 1.2 Statistics of nanoparticles worked as lubricant additives

1.2.1.1 Sulfide

Metal sulfides have been used in lubrication industry for decades, including solid and liquid lubricant additives. Lubrication mechanisms of MoS₂ have been studied extensively. Apart from their laminar structure, sulfur played an important role in the interaction between particles and lubricant molecules. Under the heat generated by friction and high contact pressure, tribochemical reaction would take place between nanoparticles and their environments (substrate, lubricants, atmosphere, among other). As a result, a tribofilm was formed on the friction surface. It is expected that different substrates would have tribofilms of various chemical composition. The unique properties of a tribofilm include hardness, adhesion, and roughness, often outperformed their substrate. The presence of a tribofilm facilitated adsorption [88]. The adsorption layer is composed of MoS₂, lubricants, and their chemically bonded compounds. A complex of –S-Mo-S-OCOR was produced after nano-MoS₂ reacted with lubricants to form fiber-like substances. Subsequently, some lubricant molecules would be anchored in this network to form adsorption film as illustrated in Figure 1.3. The tribofilm formed a metal surface played an important role in their excellent tribological performance [93]. In the same report, a tribofilm on magnesium alloy was found to be composed of MoO₃ and MgS verified by XPS spectrum.

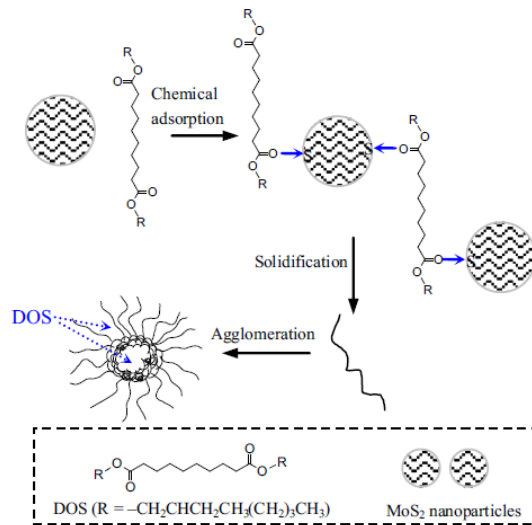


Figure 1.3 The formation of adsorption layer using MoS₂ nanoparticles (Adapted from [88]).

1.2.1.2 Nanocomposites

Nanocomposites have been reported to be used as lubricant additives. Due to the synergetic effects of more than one type of nanoparticles, composites usually show superior performance than the individual one. Lubrication mechanisms associated with nanocomposites are listed in Table 1.12. It is worth to mention that Silica (SiO₂) is one of the most common nanocomposites as lubricant additives. Nanoparticles are inherently not miscible in oil. Silane is a widely used coupling agent to improve dispersion of nanoparticles. The surface properties of nanoparticles alter from hydrophilic to lipophilic, that is favorable for tribological performance.

Table 1.12 Summary of lubrication mechanisms of nanocomposites

Nanocomposites	Lubrication mechanism
Al ₂ O ₃ /TiO ₂ nanocomposites[60]	Friction mode change: from sliding movement to rolling movement
Cu/SiO ₂ nanocomposites[71]	1. Formation of tribofilm: tribofilm composed of FeS, FeSO ₄ and SiO ₂ . 2. surface repairing effect of Cu nanoparticles released from the composite
Cu/Graphene oxide nanocomposite[95]	Synergic effect of Cu and graphene oxide.
Al ₂ O ₃ /SiO ₂ nanocomposites[59]	Synergic effect of Al ₂ O ₃ and SiO ₂
Serpentine/La(OH) ₃ nanocomposites[108]	Tribofilm formed containing Fe, Si, and O. La worked as a catalyst accelerating tribochemical interactions.

1.2.1.3 Metals

Metallic nanoparticles have the unique chemical and physical properties as lubricant additives [65]. For example, Cu has low shear stress and is softer than ceramics (oxides). It has been used as lubricant additive. Lubrication mechanisms of metallic nanoparticles could be grouped into the following: a) formation of a tribofilm or an adsorption film. These films could change the surface properties and separate two contacting surfaces, yielding promising tribological performance; b) with the addition of nanoparticles, they rolled within two sliding surfaces resulting decreased friction and wear; c) nanoparticles would be compacted on the wear track due to heat and pressure generated during friction process. This phenomenon was called sintering or repair effect. The representative metal nanoparticles and associated lubrication mechanisms are listed in Table 1.13.

Table 1.13 Summary of lubrication mechanisms of metallic nanoparticles

Nanoparticles	Mechanisms
Sn and Fe[111]	Sn is effective on friction reduction; Fe is effective on antiwear performance. A tribofilm was formed on the wear track with low shear stress and hardness result in promising performance (low friction and wear).
Bi[61]	A protective film was formed through particle's sintering effect. The film separates contacting surfaces and leads to lower friction.
Ag[54]	A protective film was formed by deposition of Ag nanoparticles. The soft metal film possesses low shearing stress and avoids the steel-steel contact from severe failure through wear.
Cu[69]	Formation of a self-repairing film on a wear track.
Pd and Au[102]	Formation of a transfer film containing Pd and Au resulting separation counter faces
Ni[97]	A protective film was formed by the deposition of Ni nanoparticles.
Cu[68]	Formation of a copper protective film separates two contact surfaces. The film has lower elasticity and certain hardness on the wear track increased the elastic deformation and reduces wear.
Fe, Cu, Co[77]	Formation of an ultrathin copper film with lower shear strength. It reduced the friction force. Nanoparticles roll within two sliding surfaces.
Pd[101]	Formation of a protective film composed of Pd providing low shear strength.

1.2.1.4 Oxides

Various metal oxides have been applied as lubricant additives, including TiO₂, CuO, Fe₃O₄, ZnO and Al₂O₃. Their lubrication mechanisms are similar to metallic nanomaterials, including tribofilms or adsorption film formation, rolling effect and sintering or repair effect. Proposed mechanisms of lubrication are listed in Table 1.14.

Table 1.14 metal oxides and mechanisms of lubrication

Nanoparticles	Lubrication mechanism
TiO ₂ [118]	1. Friction modification: nanoparticles roll within two sliding surfaces 2. surface repairing effect
CuO and Al ₂ O ₃ [58]	Tribo sintering effect of CuO
La doped TiO ₂ [100]	A boundary lubricating film was formed that was composed of iron oxide and titanium oxide.
Fe ₃ O ₄ [78]	Friction mode change: nanoparticles roll
ZnO[121]	Deposition of ZnO on wear track
ZnO and CuO[122]	Tribofilm formation with low surface roughness and more compact on the wear track
Al ₂ O ₃ [56]	Friction mode change: nanoparticles roll

1.2.1.5 Rare earth compounds

The tribological behavior of rare earth elements on lubrication has been studied extensively. The most popular elements were La and Ce. They could be either applied as lubricant additives, or be doped into other nanoparticles, such as TiO₂. Their lubrication mechanisms mainly included the formation of tribofilm or adsorption film. The associated lubrication mechanisms are listed in Table 1.15.

Table 1.15 Rare earth compounds and the associated lubrication mechanism

Nanoparticles	Lubrication mechanism
LaF ₃ [87]	Formation of tribofilm composed of Fe ₂ O ₃ , FeF ₃ and LaF ₃ .
LaF ₃ [112]	Formation of adsorption film containing LaF ₃
CeBO ₃ [106]	1. Formation of tribofilm composed of B ₂ O ₃ , CeO ₂ and Fe ₂ O ₃ 2. formation of adsorption film
CeO ₂ [64]	Formation of tribofilm composed of Ce ⁴⁺ , TiO ₂ , Ce ³⁺ , FeS(FeS ₂), iron oxide and other organic compounds

Figure 1.4 shows the tribological performance of nanoparticles in terms of minimum friction coefficient (MFC), maximum friction reduction (MFR), and maximum wear reduction (MWR). According to the results, sulfides exhibited the lowest MFC and the highest MFR and MWR. In this case, sulfur was believed to be the most important element for improving tribological performance. Despite the effectiveness, the high content of sulfur is a major drawback and would be discarded in the near future due to the environmental concern[89]. The role of morphological parameters on lubrication of MoS₂ would be discussed in the following section.

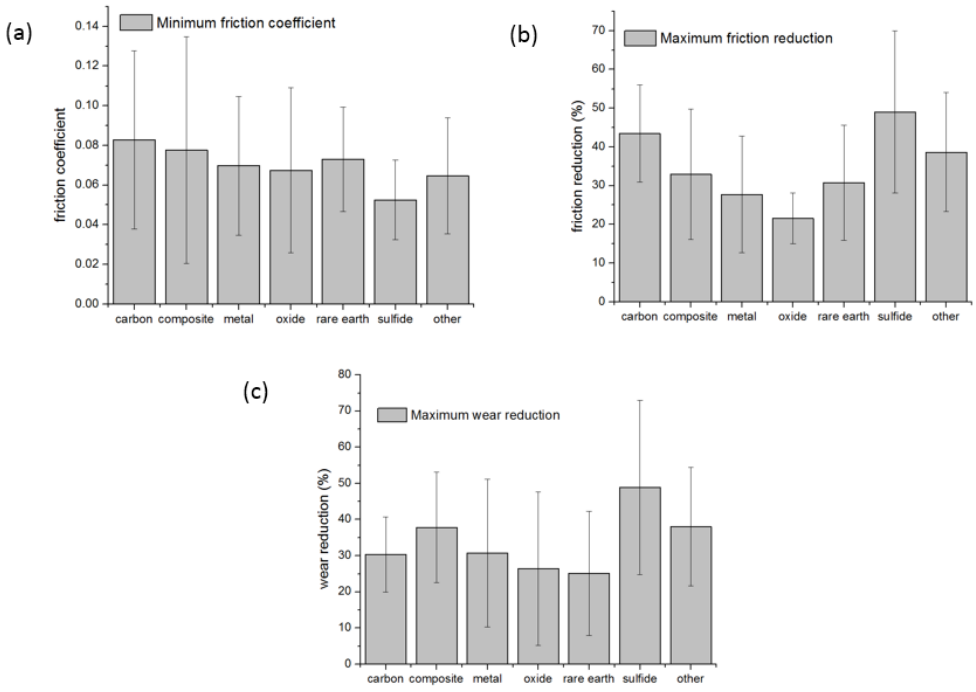


Figure 1.4 Tribological performance comparison based on different chemical composition: (a) MFC (b) MFR (c) MWR

Rare earth compounds showed similar MFC and MFR with composite nanoparticles. But for MWR, composite outperformed rare earth compounds. In the case of nanocomposites, the favorable elements were Cu, Al (Fe may come from the substrate). In the case of rare earth elements, the favorable elements were La and Ce. Considering the chemical composition and physical property of a tribofilm, the metal elements seemed to be more beneficial than rare earth elements.

Metals outperformed oxides. Lubrication mechanisms of metal nanoparticles included tribofilm formation and adsorption film formation. During lubrication, it was desirable to avoid oxidation of metal nanoparticles in order to ensure their chemical activity. The activity was important for the formation of tribofilms. Oxides were chemically inertial than pure metal particles. Lubrication mechanisms reported included rolling contact and adsorption film formation.

According to the statistical correlation data listed in Table 1.16, chemical composition showed a relatively higher correlation with MWR (0.21), compared to MFC(0.13) and MFR(0.16). It means the effects of chemical elements is subtle on frictional performance while is more related to wear resistance. Chemical composition played an important role in determining the properties of tribofilm, which might affect the antiwear performance indirectly. The effects of chemical composition on tribological performance lied on the properties of a tribofilm. The physical and chemical properties of a tribofilm were critical to nanolubrication. Regardless there is few paper found reporting properties of a tribofilm. It is believed that contact angle, adhesion, hardness,

modulus, thickness, roughness, and micron and crystal structure are all relevant to triboperformance. Future study on this aspect is recommended.

Table 1.16 Correlations between chemical composition and tribological performance

Correlations	Chemical composition	MFC	MFR (%)	MWR (%)
Chemical composition	1.0000	-0.1609	0.1301	0.2169

1.2.2 Effects of particle size

Characteristic size of nanoparticles, such as the diameter of a spherical or tubular particle, or the thickness of a lamellar, is less than 100 nm. The small size allows them easily enter into the contact interface for load bearing and lubricating. Furthermore, a high surface-to-volume ratio enables them to react with their environment. In this section, we discussed the effects of size on tribological performance.

Optimized particle size is closely related with working conditions. A report has been found that for CaCO₃ nanoparticles[63], larger sizes exhibited optimal performance under higher frequency (different lubrication regime), while smaller ones were more suitable for higher load and lower frequency(Figure 1.5). In case of IF-MoS₂ [79], once the proper recirculation occurred, nanoparticles of various sizes exhibited a similar behavior. This indicated a feeding effect of the nanoparticles in the contact region. Smaller nanoparticles showed a high probability to penetrate into the interface[125], yielding much lower friction coefficient than larger nanoparticles.

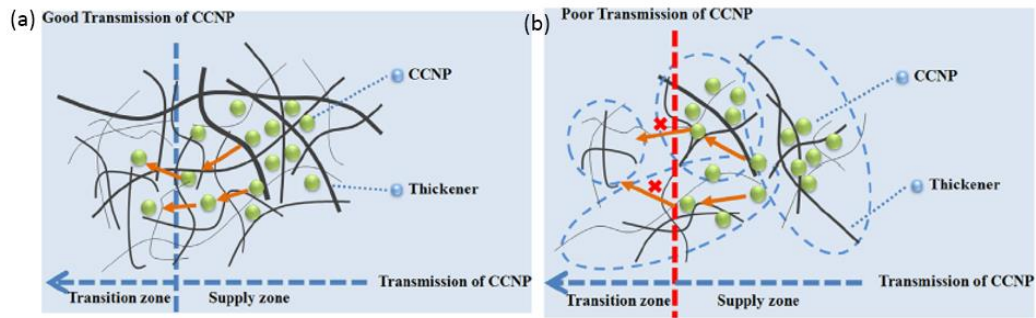


Figure 1.5 Schematic transmission processes of nanoparticles with different size (Adapted from [63]).

To summarize the published data, Figure 1.6 showed the tribological performance of nanoparticles with different sizes in terms of MFC, MFR and MWR. Table 1.17 showed the correlations between size and tribological performance. According to the calculated correlation coefficient, size exhibited relatively low correlation with friction and wear performance. The correlation coefficients with MFC, MFR and MWR are around 0.1. With the combination of data analysis and literature review, nanoparticles size has a subtle effect on tribological performance.

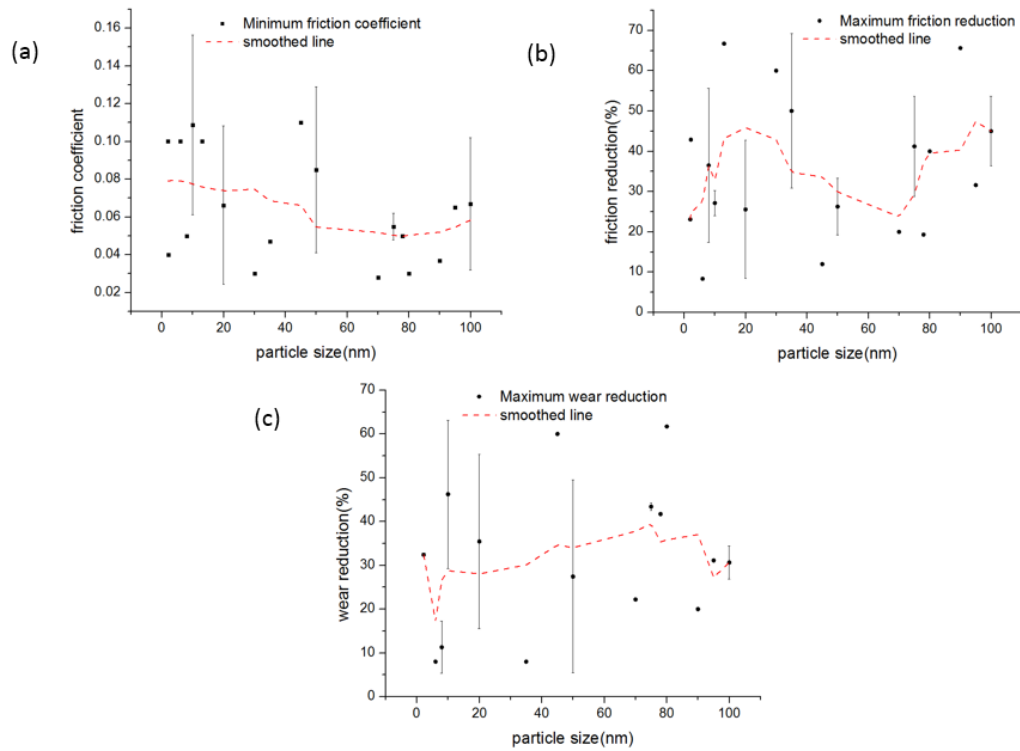


Figure 1.6 Tribological performance of nanoparticles with different size: (a) MFC, (b) MFR, (c) MWR

Table 1.17 Correlations between size and tribological performance

correlation	Size	MFC	MFR (%)	MWR (%)
Size	1.0000	-0.1002	0.1535	0.1303

1.2.3 Effects of morphology of nanoparticles

Considering the morphology of nanoparticles in Table 1.10, there are 5 types: granular, onion, sheet, spherical, and tube. The statistics of nanoparticles morphology is shown in Figure 1.7.

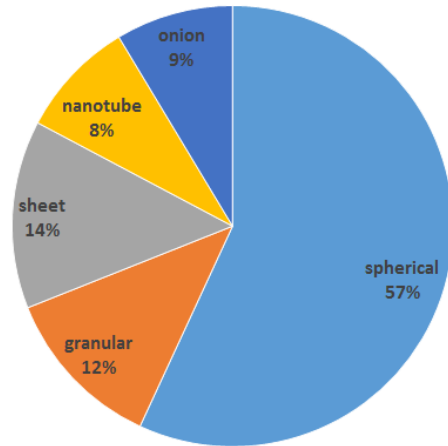


Figure 1.7 Statistics of the nanoparticles morphology

In Figure 1.7, the majority of nanoparticles' morphologies are spherical, followed by granular, sheet, onion and nanotube. After nucleation, the crystal structures of particles tend to evolve to minimize the surface energy when they reach the equilibrium state. If the surface energy is isotropic, sphere will be the ideal solution [126-128]. Onion, sheet and spherical morphology showed superior tribological performance than others as shown in Figure 1.8.

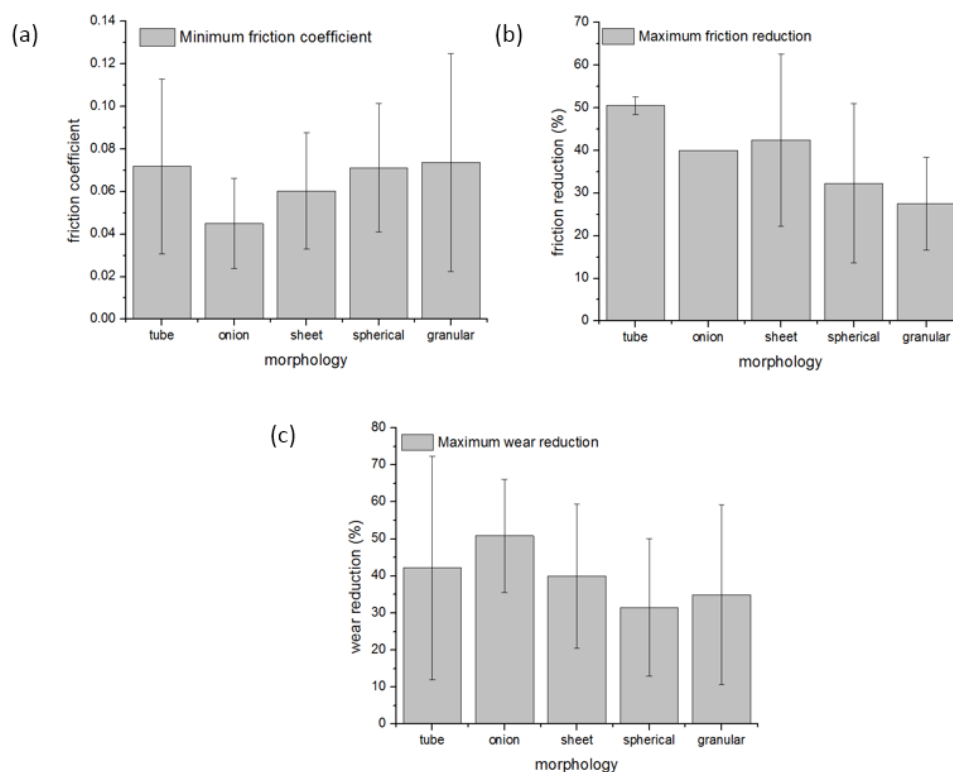


Figure 1.8 Tribological performances of nanoparticles with different morphology

Onion morphology is described as the spherical shape outside and lamellar structure inside. The stability of onion morphology is crucial to the particles tribological performance. If the onion morphology is stable, it is more close to spherical morphology. Otherwise, it will exfoliate and turn to be a sheet like morphology[129]. Its structure-performance relationship has been studied extensively[79, 83, 85, 88, 130]. The advantages of onion structure lied in the absence of dangling bonds and the spherical shape [85]. The spherical shape was favorable in rolling mechanisms. Furthermore, the number of atoms in each particle was not the same in two adjacent layers, which will facilitate the generation of dislocation. The absence of dangling bonds

promoted chemically inertial, which would weaken the interaction between the particle and environment. In this case, fewer particles would stick on the substrate. Moreover, from the chemical reaction point of view, the dangling bonds showed higher tendency to be passivated by the environment, which resulted in friction. The lubrication mechanism would be dominated by rolling other than sliding.

The lubrication mechanism of IF NP are threefold: rolling, sliding, and exfoliation[131]. Rolling friction means NPs will roll between two sliding surfaces, which requires the spherical shape and stable structure. For the sliding friction, which also requires stable structure and low adhesion to the sliding surface. For the exfoliation mechanism, the multilayered IF NP will provide low friction and wear due to the movement between the adjacent layers. Under low contact pressure, rolling friction dominated. Sliding occurred at slightly higher contact pressure, while exfoliation ruled under high contact pressure. M. Kalin [90] and coworkers proposed the lubrication mechanism of MoS₂ was attributed to the exfoliation and deformation of nanotube in boundary-lubrication regime. Rapport[132] proposed that the lubrication mechanism of IF-WS₂ depended on the different lubrication regimes. When the thickness of the film was in the size of nanoparticles, the spherical outer shape would preserve. The sliding-rolling contact should be the dominate lubrication mechanism. If film thickness was less than nanoparticle size, a transferred film would be formed. The inner sheet-like structure was believed to dominate. MoS₂ with defects was highlighted with better lubrication performance[83]. IF- MoS₂ with defect would enable exfoliation of external layer under external pressure. The contact pressure needed to exfoliate the external layer of perfect

crystalline structure was much higher than structure with defects. The exfoliated layer could work as a third-body friction. The ideal situation was more like a rolling friction effect. In fact, its performance was closely related with time (gradually exfoliation). Different cycles determined. Friction coefficient gradually decrease could be observed.

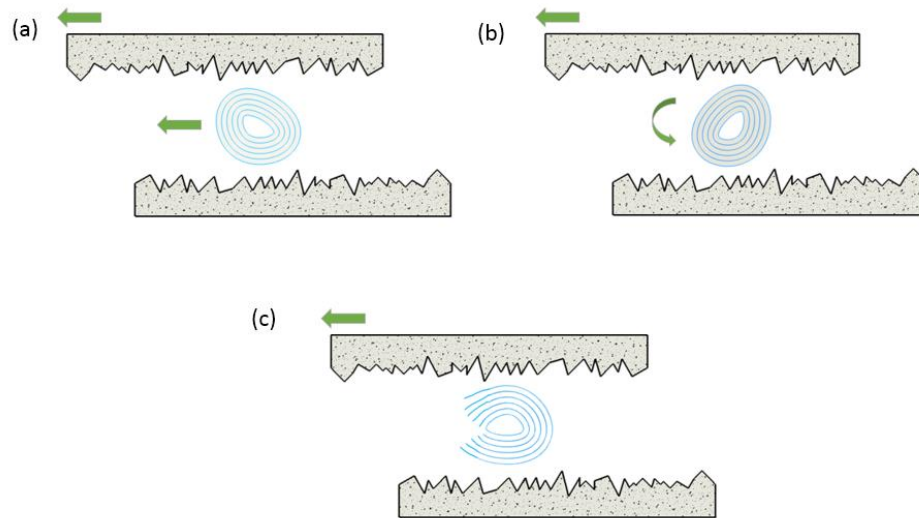


Figure 1.9 The three main friction mechanisms of multilayered IF NP (redraw from [131]): (A) sliding[133], (B) rolling[134], (C) exfoliation[135, 136]

The crystal structure of the particles played important roles in lubrication.

Tribological performance of well crystallized and poorly crystallized IF-MoS₂ particles have been compared[83]. The better lubricating property of poorly crystallized particles was attributed to their tendency to exfoliate forming a tribofilm composed of sheet-like particles on the surface.

The sheet like particle include Graphene[137], MoS₂ nanoplatelets[138], BN, Y₂O₃[139] and ZrP[124]. In fact there are two types of interactions considered in order to understand the lubrication mechanisms of the sheet like nanoparticles[140].

Interaction between the adjacent layer plays a critical role in determine the frictional behavior of nanoparticles. For Graphene, MoS₂, due to their weak interlayer van der Waals force, two adjacent layers are easily exfoliated under a shear force. Sliding movement of adjacent layer will lead to lower friction. For other 2D nanoparticles which exhibits relatively strong interlayer van der Waals force[124], including Y₂O₃ and ZrP, it is difficult for them to exfoliate. Authors proposed that nanoparticles align with the fluid, which will reduce the fluid drag. Another interaction related with the outer layer and the substrate, which is an example of the surface energy of the basal plane as well as the property of the environment.

The number of layers and the interlayer spacing are reported to affect tribological performance. When the number of layers decreased, it will raise other issues, including the puckering and wrinkle effect, inclination angles[139], interlayer spacing[141]. ZrP, with lower interlayer spacing, provided promising effect in reducing friction in boundary lubrication regime.

To summarize, Table 1.18 showed the correlations between morphology and tribological performance. Morphology exhibited a high correlation coefficient with MFR, which indicated its effect on frictional performances. However, the low correlation coefficient with MWR leads to subtle effect on antiwear behavior. Alternatively, we could calculate the correlation coefficient and matrix between aspect ratio and tribological performance, as listed in Table 1.19 shows. It provided a similar trend with morphology relationship.

Table 1.18 Correlations between morphology and tribological performance

correlation	Morphology	MFC	MFR (%)	MWR (%)
Morphology	1.0000	0.0823	-0.3012	0.0001

Table 1.19 Correlations between aspect ratio and tribological performance

correlation	Aspect ratio	MFC	MFR (%)	MWR (%)
Aspect ratio	1.0000	-0.0808	0.2653	0.0556

1.3 Performance characteristics of lubricants

Viscosity is one of the most important properties of liquid lubricants, which influences their rheological properties and tribological performance. If we imagine the liquid is a deck of cards, viscosity is a measure of the resistance between adjacent cards during flowing. Dynamic viscosity is defined as the shear stress per unit velocity gradient in the flow direction.

$$\eta = \tau / \gamma \quad (1-1)$$

Where η is dynamic viscosity, τ is shear stress and γ is velocity gradient.

Kinematic viscosity is defined as the ratio of dynamic viscosity to density.

$$\text{Kinematic viscosity} = \text{Dynamic viscosity} / \text{Density} \quad (1-2)$$

Viscosity of Newtonian fluid is constant under different velocity gradient. Some liquid lubricants with relatively simple molecular structure fall into this category. Others are non-Newtonian fluid. In SI system, units of shear stress and velocity gradient are N/m^2 (Pa) and s^{-1} , respectively. So the unit of dynamic viscosity is Pa.s or Ns/m^2 . Other commonly used units are centipoise (cP) and reyn, which follows that:

$$1 \text{ reyn} = 68.95 \times 10^5 \text{ cP} = 68.95 \times 10^3 \text{ poise} = 68.95 \times 10^2 \text{ Pa.s} = 68.95 \times 10^5 \text{ mPa.s} \quad (1-3)$$

For kinematic viscosity, unit in SI system is m^2s^{-1} . In practical use, kinematic viscosity are usually quoted in centistokes (cS):

$$1 \text{ cS} = 1 \times 10^{-2} \text{ stoke} = 1 \text{ mm}^2\text{s}^{-1} \quad (1-4)$$

In order to measure the viscosity of lubricants, two types of instruments are employed. One is the Ostwald viscometer, which measures the viscosity of Newtonian fluid. A given amount of fluid flows out of a container via a narrow capillary tube and the flowing time multiplies by a calibration factor to determine its viscosity. Figure 1.10 shows a typical setup of the Ostwald viscometer. The other one is rheometer, which measures the viscosity of non-Newtonian fluid. Fluid is added into the gap between the upper plate and lower plate. Shear stress is measured and fluid velocity gradient is controlled by the rotational speed of upper plate. Basically, there are three types of rheometer: concentric cylinders, cone and plate, and parallel plates, which corresponds to different fluid viscosity range. Concentric cylinders usually measure the fluid with very low to medium viscosity. For the fluid viscosity ranging from very low to high (like soft solids), cone or parallel plate are more suitable. Typical setup of three rheometer models are shown in Figure 1.11.

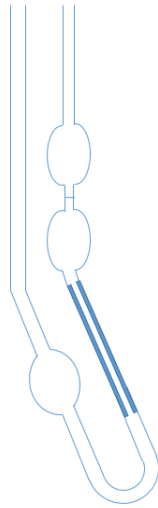


Figure 1.10 A typical setup of Ostwald viscometer

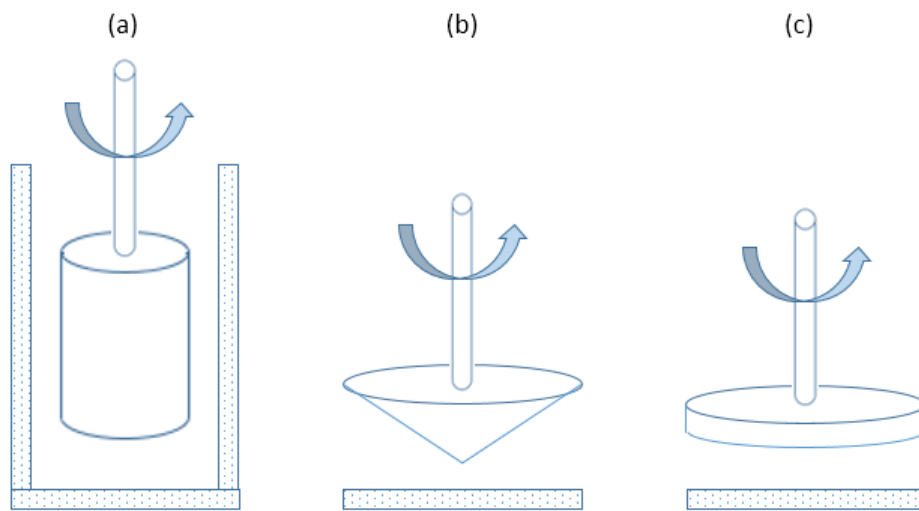


Figure 1.11 The typical setup of rheometer: (a) concentric cylinders (b) cone and plate (c) parallel plate

In order to categorize the frictional performance of lubricants under different working conditions (Load, velocity, and viscosity), Stribeck curve is present to describe the correlation between friction and Sommerfeld number in 1902. Standard Sommerfeld

number is the dimensionless characteristic number in fluid bearing design. It is defined in the following equation:

$$\text{Sommerfeld number} = (r/c)^2 \eta N/P \quad (1-5)$$

Where r is the shaft radius, c is the radial clearance, η is the absolute viscosity, N is the shaft rotating speed and P is the load per unit area. To extend the concept to a general surface contact (not just bearing contact), the simplified Sommerfeld number was adopted, which is:

$$\text{Simplified Sommerfeld number} = \eta N/P \quad (1-6)$$

Where η is the absolute viscosity, v is the sliding velocity and P is the load. A typical Stribeck curve could be found in Figure 1.12. Three lubrication regimes could be divided based on the lambda value (λ). λ is defined as:

$$\lambda = h_{\min}/(R_{q1}^2 + R_{q2}^2)^{0.5} \quad (1-7)$$

Where h_{\min} is the minimum oil film thickness between the surfaces, R_{q1} and R_{q2} are surface roughness of the two counterparts respectively. $(R_{q1}^2 + R_{q2}^2)^{0.5}$ is the composite surface roughness. When λ is far less than 1, which means two surfaces are closely contact with each other. High friction coefficient will occur in this regime because of the interference of surface asperities. When the oil film thickness is comparable with composite surface roughness ($1 \leq \lambda \leq 3$), it indicates the mix lubrication regimes. Friction coefficient will gradually decrease with the increase of Sommerfeld number. Higher Sommerfeld number will give rise to thicker oil film, which in turn weaken the interference effect of surface asperities. When the two surfaces are

completely separated by a relatively thick oil film ($\lambda > 3$), the lowest friction coefficient could be achieved.

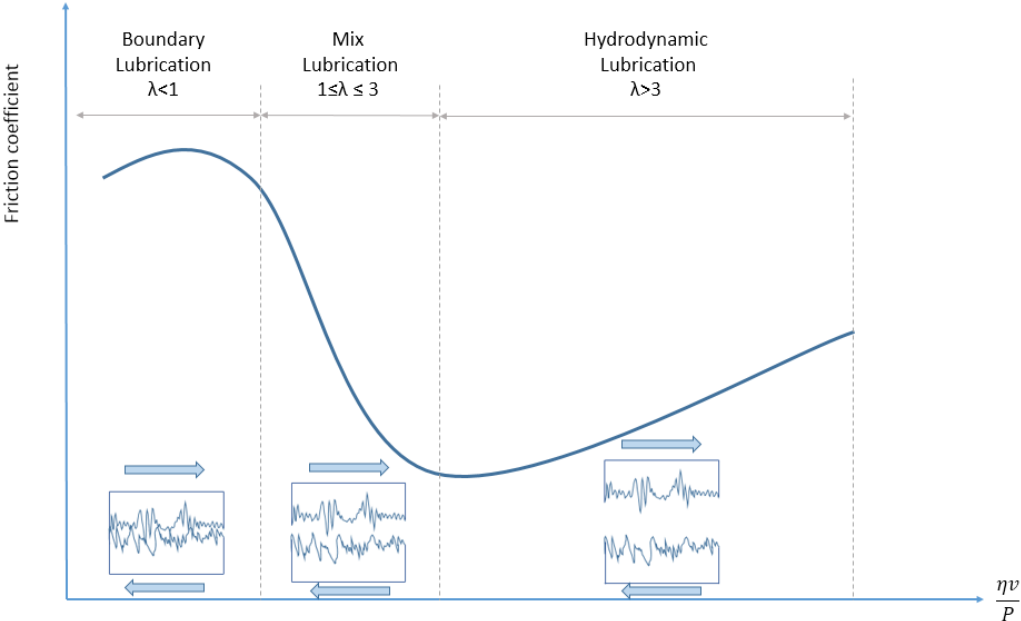


Figure 1.12 A typical Stribeck curve

CHAPTER II

MOTIVATIONS AND OBJECTIVES

As discussed in Chapter I, lubrication is essential to industries and applications involving mechanical systems in motion. Nanoparticles play important roles in overcoming frictional loss as lubricant additives. In order to improve the performance of a lubricating system, the better understanding of interfacial behavior and tribological properties of nanoparticles is highly desired. This research focuses on novel nanoparticles and their effects on tribological performance as lubricant additives. In this research, there are three major objectives: (1) Tribological performance and rheological properties of nanoparticles; (2) Investigation of lubricating kinetics; (3) Investigation of lubricating dynamics. The research approach is illustrated in Figure 2.1.

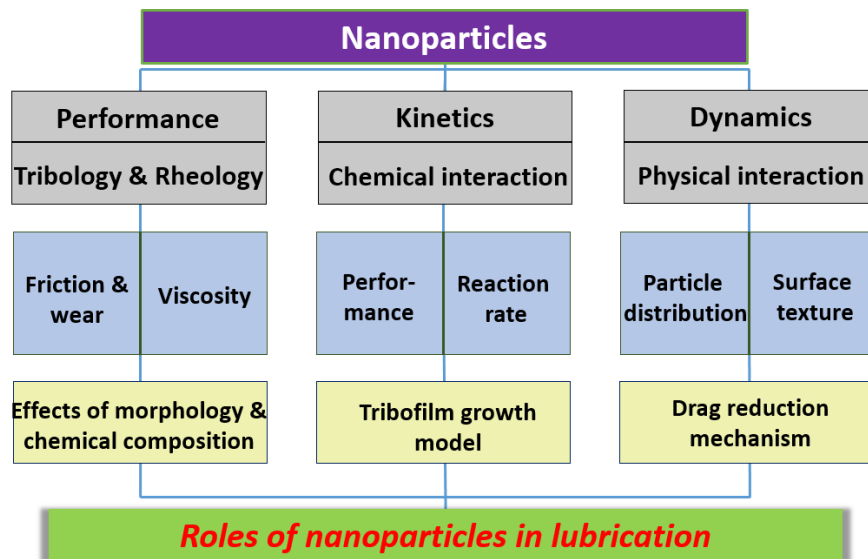


Figure 2.1 Research flow chart

2.1 Tribological performance and rheological properties of nanoparticles

Conventional lubricants are not favorable for the environment. There is a strong desire to develop environmental friendly and high efficiency lubricants. Tribological performance and rheological properties of nanoparticles in oil will be evaluated in term of friction, wear and viscosity. The mechanism of lubrication will be revealed via the characterization of wear tracks.

2.2 Investigation of lubricating kinetics

Tribofilms play an important role in lubrication. They are the products of tribochemical reactions. However, the mechanism of formation and growth of tribofilms is still unknown. There is no universal method to monitor the tribochemical reactions. A novel approach will be proposed to *in situ* characterize the formation and growth of tribofilms. The model and driving force of growth of tribofilms will be discussed as well.

2.3 Investigation of lubricating dynamics

The majority of lubricating system are closed system. The interaction between the lubricants and interfaces could not be directly observed. With the help of fluorescent nanoparticles, we are able to “see” how the lubricant works in a mechanical system. Nano diamond particles will be employed to study the lubricating mechanism of sharkskin like surfaces. The distribution of particles will be characterized using a laser

scanning microscope. The drag reduction effect of sharkskin like surfaces will be interpreted in a different perspective.

CHAPTER III

MATERIALS AND METHODS

Experiment details in the present research are provided in this chapter. Firstly, synthesis of materials and fabrication of shark-skin-like surfaces are discussed in the first section. Then the tribological and rheological evaluation are introduced successively. Finally, approaches of lubricating kinetics and dynamics are provided.

3.1 Materials

3.1.1 Synthesis of α -ZrP

The α -ZrP nanoplatelets were synthesized by hydrothermal method reported by Sun and coworkers[142], and it has been described in our previous reports[143, 144]. Zirconyl chloride octahydrate (>99.0 wt. %) was purchased from Fluka. Phosphoric acid (85 wt. % in H₂O) was purchased from Fisher-Scientific. In summary, 4.0 g of ZrOCl₂•8H₂O was mixed well with 40.0 mL 12 M H₃PO₄ in a sealed Teflon®-lined pressure vessel and heated at 200°C for 24 h. The product was washed with deionized water and isolated by centrifuging five times at 5000rpm, and dried at 70°C for 24h. To study the performance of α -ZrP, the base oil and ZDDP was kindly provided by Shell Global Solutions (US). The concentrations of nanoplatelets and ZDDP in the base oil are 0.2 wt% and 0.8 wt%, respectively, corresponding to 0.02 wt% and 0.08 wt% phosphorous content.

3.1.2 Synthesis of V₂O₅

The fabrication process of V₂O₅ particles has been reported by Pan[145]. In summary, 1mmol V₂O₅ micro powders (Sigma Aldrich) were mixed in 22.5 ml DI water. Then 2.5 ml 30% H₂O₂ (Sigma Aldrich) was dropped slowly into the solution and stirring for 2h. After that, 0.5g PEG 600 (polyethylene glycol 600) (Sigma Aldrich) was added into the transparent orange solution. Then the solution was kept in a hydrothermal vessel at 200 °C for 6h. Particles were washed with ethanol and DI water subsequently and dried at 70°C for 12 h. Finally, particles were annealed in oven at 350°C for 30 min. Figure 3.1 shows the TEM image of the particles. It appears a rectangular morphology. The length and width for those particles of V₂O₅ are 100nm and 50 nm respectively. Figure 3.2 shows the Raman spectrum of V₂O₅, which reveals the characteristic peaks at 397.7 cm⁻¹, 467.8 cm⁻¹, 522.2 cm⁻¹, 691.1 cm⁻¹, and 987.8 cm⁻¹, respectively. Light mineral oil (Sigma Aldrich) was utilized as the base oil for tribological test. It composed of hydrocarbon molecules without any lubricant additives. The density is 0.84g/mL at 25°C, and viscosity is 14.2 ~ 17 cst at 40°C and 0.18 ~ 0.2 cst at 100°C respectively. It belongs to API (American Petroleum Institute) Group I. In order to make sure the good suspension of nanoparticles, concentration of sheet like V₂O₅ was configured from 0.05% (wt) to 0.2% (wt). No surfactant was added.

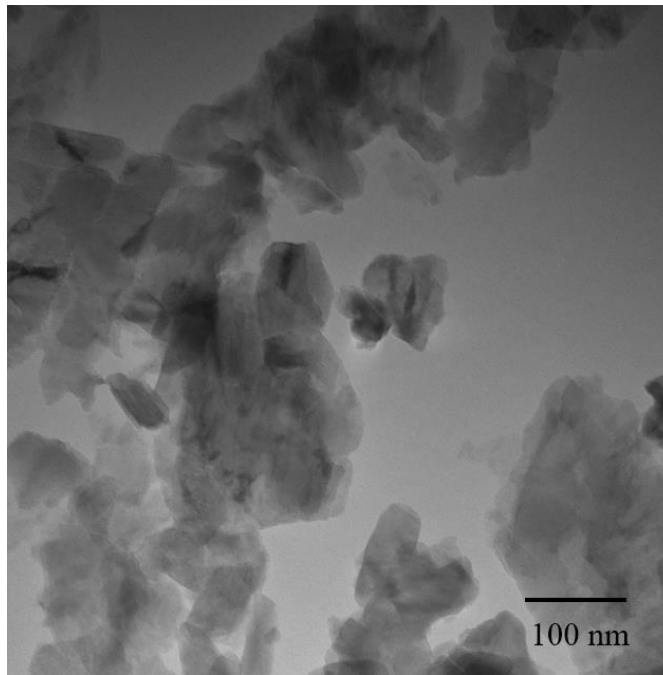


Figure 3.1 TEM images of sheet like V₂O₅

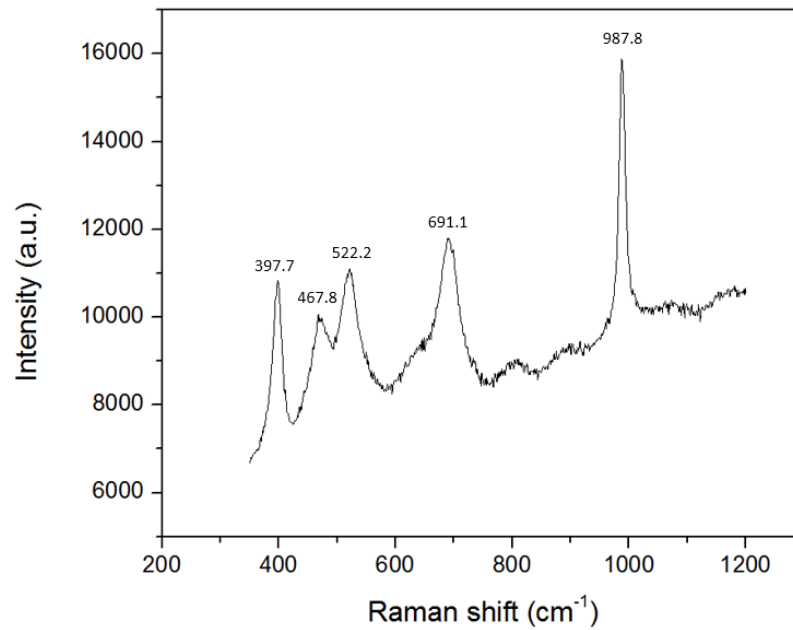


Figure 3.2 Raman spectrum of sheet like V₂O₅

3.1.3 Fabrication of Shark-skin-like surface

Performance of 3D printed shark-skin-like surfaces were studied. Design and dimensions of a single shark skin scale were illustrated in Figure 3.3. The height of ridges was 400 μm . The diameter of textured surface was 25mm. Scale orientation was defined as the angles between the ridges and fluid flow direction. To evaluate the sharkskin performance with different scale orientation, three textured surface were designed using SolidWorks (SolidWorks Corp., Waltham, MA, USA) as shown in Figure 3.3. The smooth surface was measured as well for comparison. Shark-skin-like surfaces were fabricated using a FlashForge Dreamer dual extrusion 3D printer. Nozzle size is 400 μm and layer thickness is ranging from 100 μm to 400 μm . The polymer for 3D printing is acrylonitrile butadiene styrene (ABS). Melting temperature is 105 $^{\circ}\text{C}$ and tensile strength is 34~38 GPa. Rigid surface will maintain the shape during the fluidic test. Printing temperature is around 220 $^{\circ}\text{C}$.

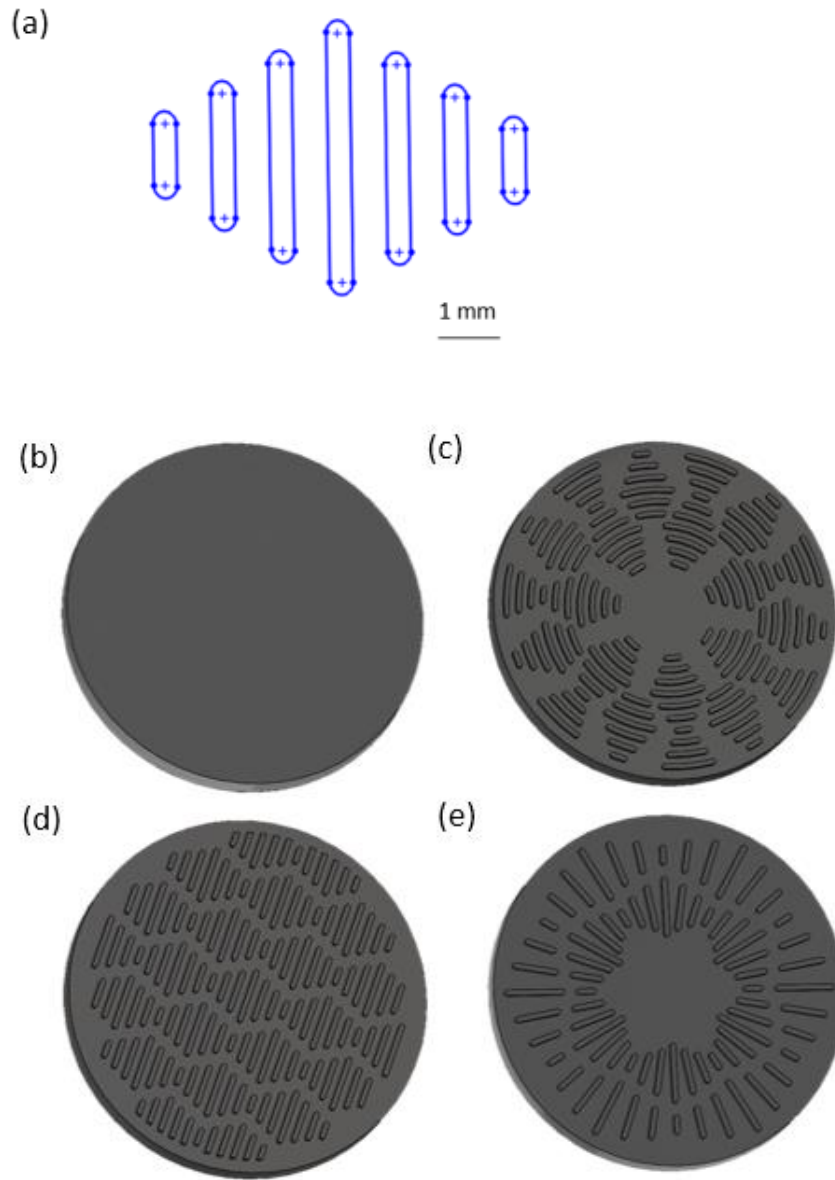


Figure 3.3 Design and dimensions of shark-skin-like surface: single scale of sharkskin: (a) a simplified model of shark-skinned surface (b) a smooth surface for comparison (c) a textured surfaces with parallel shark-skin scale orientation (0 degree) (d) a textured surface with shark skin mix scale orientation (45 degree) (e) a textured surfaces with perpendicular shark-skin scale orientation (90 degree).

3.2 Tribological evaluation

3.2.1 Tribological evaluation of α -ZrP

Tribological evaluation of α -ZrP was conducted using a pin-on-disk tribometer. Bearing steel E52100 was used as pin (ball) ($\phi=6\text{mm}$) with surface roughness Ra_1 of $1.2\ \mu\text{m}$. The same material was used as a substrate and has Ra_2 of $0.01\ \mu\text{m}$, resulting in a composite surface roughness of $1.2\ \mu\text{m}$. Reciprocating sliding motion was configured in order to evaluate the wear behavior under a 5N load (which corresponds to a maximum Hertzian pressure of 1GPa) and a 1Hz oscillation frequency. Wear track and sliding distance were set to 10mm and 5000m , respectively. The calculated oil film thickness is $0.04\ \mu\text{m}$ based on Hamrock and Dowson formula [146]. Therefore, the theoretical lambda ratio is 0.03 , which ensures boundary lubrication. Wear volume was measured using a profilometer (KLA Tencor). Each test was repeated for at least three times for statistical analysis.

3.2.2 Tribological evaluation of V_2O_5

Tribological performance of sheet like V_2O_5 was evaluated in terms of friction and wear under different working conditions. Tribology test was performed using a pin-on-disk tribometer (CSM). Both the pin and substrate materials are E52100 bearing steel. The pin is a bearing ball of 6mm diameter. Their corresponding root mean square of surface roughness are $1.2\ \mu\text{m}$ (Rq_1) and $0.01\ \mu\text{m}$ (Rq_2), respectively. As such, the composite surface roughness could be calculated as $\sqrt{Rq_1^2 + Rq_2^2} = 1.2\ \mu\text{m}$. Rotational mode was set up to evaluate the friction behavior under different loads of $0.15\sim 1\text{N}$ and

at sliding speeds ranged in 0.004~0.4m/s. Friction performance of the boundary lubrication regime, mix lubrication regime and hydrodynamic regime were provided to plot the Stribeck curve. On the other hand, wear test was conducted in the boundary lubrication regime via reciprocating sliding mode. Load and oscillation frequency was set up as 5N (1GPa) and 1 Hz, respectively. The length of wear track was 10 mm and total sliding distance was 5000m. Therefore, the maximum oil film thickness was 0.05 μm and theoretical lambda value is 0.04, which indicates the boundary lubrication regime. Wear volume was measured using a profilometer (KLA Tencor). After measuring cross-sectional area of 8 different positions of wear track, the average value could be calculated. Volume of wear track would be the product of average cross-sectional area and total length. Each test was repeated for at least three times.

3.2.3 Tribological evaluation of NaYF₄

Friction experiments of NaYF₄ were conducted using a pin-on-disk tribometer at room temperature. Both pin and substrate were made of 52100 bearing steel. The diameter of the pin was 6mm and the maximum Hertzian contact pressure was 1 GPa. The roughness of the pin and substrate were 1.2 μm and 0.01 μm , respectively. Before tribotesting, samples were cleaned using DI water and acetone in succession. The volume of liquid lubricant for each test is 200 microliter and the contact area is fully submerged throughout the experiment. Utilization of a small amount of lubricant will prove the high efficiency of NaYF₄ as additives. A reciprocating sliding motion was used for experiments and the frequency was set at 1 Hertz with the amplitude 10mm.

Sliding distance was 5000 meters and the wear volume was measured through the change in surface profile. Each test was repeated for least three times.

3.3 Rheological evaluation

3.3.1 Rheological evaluation of nanoparticles

Viscosity measurement was conducted on an AR-G2 rheometer (TA Instruments) under ambient temperature (25°C). The gap between the spindle ($\Phi=25\text{mm}$) and lower plate was 200 μm and filled with test solution. Shear rate of the spindle ranged from 1 s^{-1} to 7500 s^{-1} . Shear stress, viscosity, and other parameters were recorded in real time. Each test was repeated for at least three times.

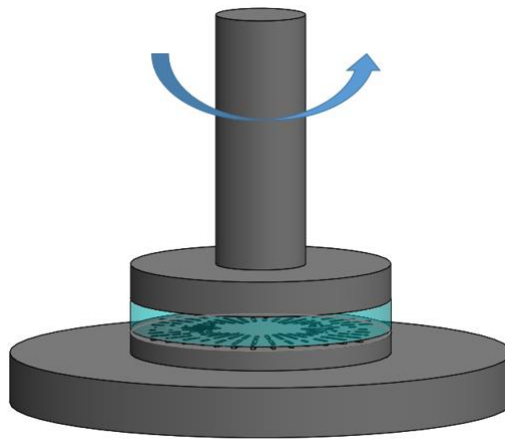


Figure 3.4 The schematic illustration of the rheometer

3.3.2 Rheological evaluation of shark-skin-like surface

Effects of drag reduction were studied through measuring the viscosity of fluid flowing over various surfaces. The viscosity of deionized (DI) water containing 0.1 wt%

diamond particles was measured using an AR-G2 rheometer (TA instruments) under the ambient temperature (25°C). DI water will avoid the interference of impurity during viscosity measurement. Diamond particles are florescent and were used as markers representing the fluidic performance. Particles were uniformly distributed in water. Textured surfaces were fixed on the lower plate. The gap between the spindle ($\Phi=25\text{mm}$) and the textured surface was set at 3 mm and was fulfilled with water. The shear rate is ranged from 0 ~ 700 s^{-1} to cover the regime from laminar flow to turbulent flow. The shear stress and other parameters were recorded simultaneously. Water viscosity was calculated as the ratio of shear stress to shear rate. Each experiments was repeated for at least three times. The schematic illustration of rheometer was shown in Figure 3.5. We found some solution would splash out of textured surface under high shear rate in the old design (Figure 3.4). In this case, liquid volume would decrease and air gap would exist between the upper spindle and textured surface, which leads to large error to the shear stress and viscosity. A new design for textured surface viscosity measurement was shown in Figure 3.5. The extra container would make sure there was a constant liquid volume during the viscosity measurement. Each test 10 ml solution was added in the container to eliminate the air gap. Under the high shear rate ($>400 \text{ s}^{-1}$), liquid level will become a cone shape due to the centrifugal force as shown in Figure 3.5.

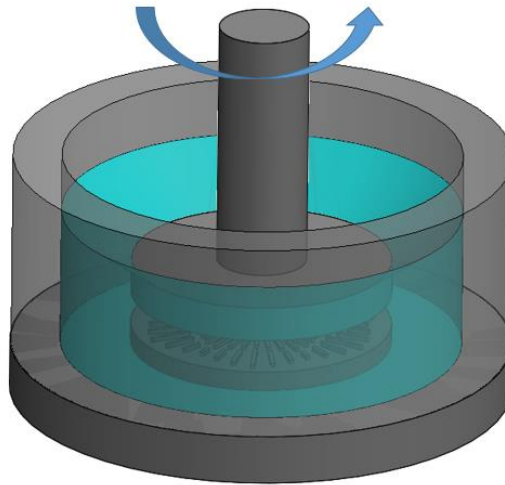


Figure 3.5 A new design of surface viscosity measurement

3.4 Methods of lubricating kinetics and dynamics

3.4.1 Wear track characterization

Wear track surfaces were carefully cleaned with ethanol and kimwipes to remove the residual oil and wear debris. In order to identify the lubrication mechanism, the wear tracks were then characterized using SEM (Vega Tescon, accelerating voltage is 10KV), profiler (KLA-Tencor P-6 Stylus). The Raman spectra was collected with iHR550 Spectrometer (HORIBA Scientific) at 532 nm with a 50x Nikon objective (NA 0.45) from the position within the wear tracks. The laser power at the sample was ~ 0.08 mW and the acquisition time for all spectra was 10s. Deconvolution of Raman spectrum is based on a multi-peak Gaussian-fitting function from Origin software. Samples were further characterized by Oxford EDS system. Raman FWHM CCD resolution is in the order of 1 nm and EDS spatial resolution is in the order of 100 nm. EDS results has been repeated at least three times in different locations to make sure the repeatability.

3.4.2 Lubrication kinetics

In this research, lubrication kinetics is correlated with the contact resistance. The electrical contact resistance between the pin and disk was monitored using a multimeter during sliding, as illustrated in Figure 3.6. The accuracy of the multi-meter is 0.1Ω for contact resistance measurement. The coefficient of friction and contact resistance were recorded simultaneously. In this measurement, experimental parameters are the same with that in wear tests.

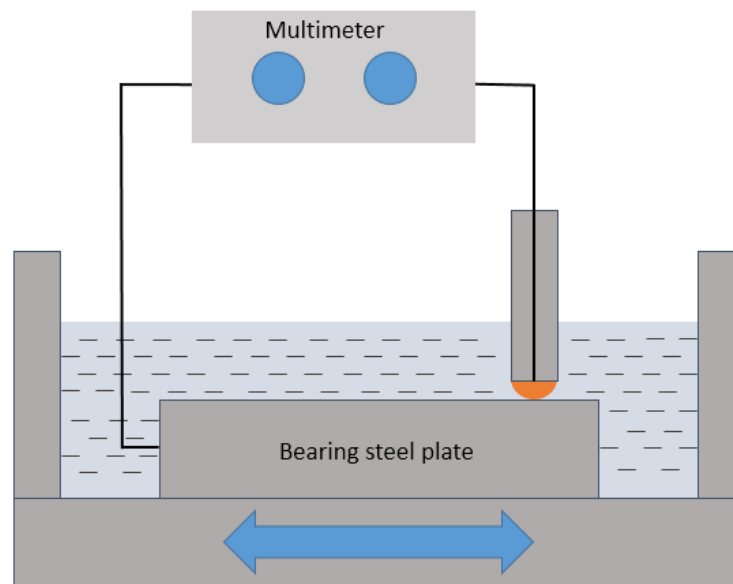


Figure 3.6 The setup of the contact resistance measurement.

Wear track of NaYF_4 was characterized *ex situ* by using a scanning electron microscope (Vega Tescon). The surface profile was obtained by using a profilometer. At least 8 different positions on the wear track was measured and the average cross-

sectional area was calculated. The wear volume is the product of the average cross-sectional area and the wear track length. The Raman spectra were obtained *ex situ* using the Spectrometer(HORIBA Scientific) at 532 nm with a 50x objective (NA 0.45) within the wear tracks. The laser power was set at ~0.08 mW with an acquisition time of 10s. Deconvolution of Raman spectrum was one through multi-peak Gaussian-fitting function using Origin software. Samples were preserved after various sliding time (0.5h to 3h) in order to study the evolution of Raman spectrum correlating to a tribofilm. Samples were characterized *ex situ* using the EDS system (Oxford).

3.4.3 Lubrication dynamics

In order to study the fluid behavior of NaYF₄ and diamond particles during sliding motion, optical images of wear track were obtained using a home-made confocal laser scanning microscope as shown in Figure 3.7. In order to scan over a large area (1mm X 1mm), it was necessary to use a low magnification microscope objective with relatively wide field of view (10x motoyota long working distance (35mm)). Samples were scanned with a 532 nm laser excitation with low power 10 mW. The optical images were collected and analyzed using a homemade spectrometer equipped with a starlight camera and a photon counter.

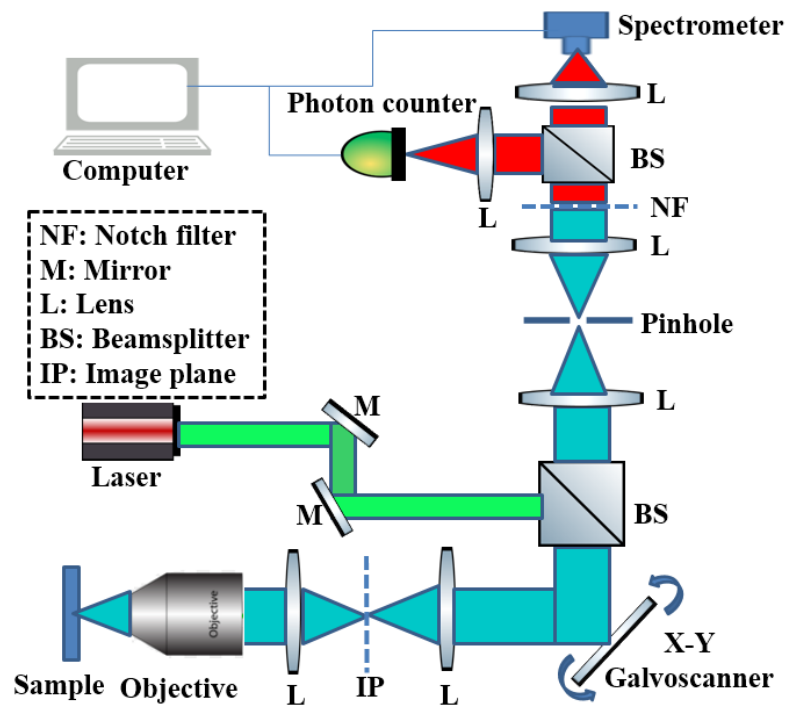


Figure 3.7 Setup of a home-made confocal laser scanning microscope.

CHAPTER IV

TRIBOLOGICAL PERFORMANCES AND MECHANISMS OF LUBRICATION USING NANOPARTICLES AS ADDITIVES²

In this chapter, the lubricating characteristics of α -ZrP and V₂O₅ nanoparticles are investigated. Tribological and rheological behavior of nanoparticles are discussed in the first section. Then wear track characterization of α -ZrP and V₂O₅ nanoparticles are introduced successively. Finally, lubricating mechanism of nanoparticles are proposed.

4.1 Roles of α -ZrP in oil lubrication

Since its discovery, Zinc dialkyl-dithiophosphate (ZDDP) has been used as the main anti-wear lubricant additive for almost a century. However, its potential poisoning to the vehicle emission catalyst raised environmental concerns and prompted the need for eco-friendly lubricants. In general, lubricant additives include antioxidants, anti-wear additives, corrosion inhibitors, dispersants, defoamants, pour point depressants, viscosity modifiers, among others [147], and are used to compensate for the deficiencies of the base oil. Among those, ZDDP has been widely used because of its antiwear characteristics[148], which is largely due to the formation of a phosphate-based

² Part of this chapter is reproduced by permission of "Formation of Anti-Wear Tribofilms via α -ZrP Nanoplatelet as Lubricant Additives" by Wei Dai, Bassem Kheireddin, Hong Gao, Yuwei Kan, Abraham Clearfield and Hong Liang, *Lubricants* 4. 3 (2016): 28. (Copyright © 2016 MDPI, all rights reserved); and from "Effects of Vanadium Oxide Nanoparticles on Friction and Wear Reduction" by Wei Dai, Kyungjun Lee, Alexander M Sinyukov and Hong Liang. *Journal of Tribology* 139.6 (2017): 061607. (Copyright © 2017 ASME, all rights reserved);

tribofilm. Phosphorous, however, has been reported to be damaging not only to the converter catalyst in engine emission, but also to the environment in general. Efforts continue to be made to find suitable alternatives or reduce its content. In addition, its low thermal stability leads to staining of metal surfaces [148]. Therefore, it is highly desirable to develop new lubricant additives with reduced phosphorous content.

In recent years, various novel lubricant additives have been developed, including nanoparticles, ionic liquids, and organic additive derivatives. Under different working conditions, those additives form tribofilms. A brief review was conducted, and a list of such additives is summarized in Table 4.1. As seen, the majority of the additives contains phosphate and sulfur compounds, which are not favorable for the environment.

In this section, the tribological performance of α -ZrP is studied and compared to ZDDP. We have recently investigated the lubricating behavior of amine intercalated α -ZrP nanoparticles and found that they reduced friction by more than 60% in a mineral oil [143, 144]. In this work, we study their effects on wear protection. The knowledge gained from this study is of great importance to the design of novel nanoparticle additives aimed at improving tribological performance.

Table 4.1 Properties of tribofilm formed by different additives.

Materi als	Base stock	Counte rpart	Chemi cal compo sition	Film thickne ss	Mecha nical propert ies	Tribolo gical perfor mance	Charac terizati on method	Refere nce
boron based additive s	5W-30	E5210 0	Ca, O, S, B, Cr and ~40 at. % Fe	15nm		friction and wear reducti on	atom- probe tomogr aphy and TEM	[149]
Phosph ate additiv es, AD and JD	trietha nolami ne aqueou s solutio n	GCr15 bearing steel	P is in the form of phosph ate or polyph osphat e; S mainly exists as FeSO4 and FeS2			friction and wear reducti on	XPS and XANE S	[150]
S- based EP additiv e and MoDT C additiv e	PAO	nc- WC/a- C(Al) carbon -based nanoco mposit e coating	WS2 or MoS2 + WS2- contain ing tribofil m		hardne ss (H)=18 .3GPa, elastic modul us (E)=21 3.1GPa	Superi or low- friction and anti- wear behavi ors	XPS and TEM	[151]

Table 4.1 Properties of tribofilm formed by different additives, continued.

attapul gite powder s(silica te compo sed of some oxide)	minera l lubrica ting oil (150S N)	52100 steel and 1045 steel	FeO, Fe2O3, FeOO H and SiOx		friction and wear reducti on	EDS and XPS	[152]
IL [P6661 4] [DEHP]	Chevro n 15W 40 and 0W30	steel- steel and silicon nitride -steel	metal phosph ates and oxides	25nm	wear reducti on	EDS, XPS and TEM	[153]
Dithioc arbama te derivat ive additiv es	HVI WH15 0	GCr15 bearing steel a nd AISI 52100 steel	organi c sulphid e, pyrite,s ulphite , - SC(=S) -N- part		better antiwe ar perfor mance and extrem e pressur e propert y	XANE S	[154]
Haloge n-free borate ionic liquids		AISI 52100 steel- steel	phosph ate based t ribofil m		friction and wear reducti on	XPS	[155]
IF- MoS2	blend of PAO 4 and PAO 40	AISI 52100 steel- steel	iron oxide and sulfide s, MoS2,	50~10 0nm	friction and wear reducti on	XPS and FIB	[79]

Table 4.1 Properties of tribofilm formed by different additives, continued.

calcium sulphate	PAO	aluminum–silicon and chromium steel	calcium carbonate and sulphur			wear reduction	ToF-SIMS	[156]
borate ester containing nitrogen	PAO	nitride AISI 52100 steel	hexagonal BN and B ₂ O ₃			friction reduced by 34% and wear reduced by 45%	XPS	[157]
oleic acid-modified serpentine UFPs	mineral base oil (500S N)	GCr15 steel ball and 1045 steel disc	Fe ₃ O ₄ , FeSi, SiO ₂ , AlFe and Fe ₃ C	500–600 nm	hardness=8 GPa within 100nm, modulus=240 GPa within 100nm	friction and wear reduction	EDS, TEM	[158]
two P- and/or S-containing additives	water-based lubricant	GCr15 bearing steel	phosphate or polyphosphate, FeSO ₄ and FeS ₂			friction and wear reduction	XPS and XANES	[159]

Table 4.1 Properties of tribofilm formed by different additives, continued.

Cu nanoparticles and hydrosilicate powders	diesel oil	Ball AISI 52100 and Disk AISI 1045	iron oxides, silicon oxides, Si–O species, graphite, organic compounds, Cu species	friction and wear reduction	EDS and XPS	[70]
--	------------	--	--	-----------------------------	-------------	------

4.1.1 Friction reduction

A significant reduction in friction was observed during pin-on-disk tribotests, as shown in Figure 4.1. In the case of the base oil (black squares), the process can be divided into three regimes. First, friction coefficient increases and reaches 0.22 at 1500m which indicates the running-in regime. It provides the highest friction coefficient throughout the process. With increasing sliding distance to 3500m, the friction coefficient decreases gradually to 0.16 due to the increase in contact area. Under a constant load, the contact pressure decreases resulting in a lower friction. Eventually, the friction coefficient stabilizes, reaching a steady state. The base oil + ZDDP did not show the improved performance as seen in the case of α -ZrP. In fact, the friction coefficient actually increased after a certain time. This is consistent with the report that the ZDDP increases friction due to the formation of a non-uniform tribofilm [160]. While in the case of base oil + α -ZrP, as labeled by blue triangles, it is clearly seen that the friction is

reduced by nearly 50% compared to the base oil + ZDDP case. We have recently reported the effective reduction of friction using sheet-like α -ZrP nanoparticles in both mineral oil and water[143]. Within the boundary lubrication regime, two surfaces are closely in contact with each other. The sheet-like particles are able to separate the surfaces, thereby avoiding direct contact. The weak van der Waals force between the discs is responsible for providing the load bearing capacity and shear force reduction. Similar results have been observed by other sheet-like particles, such as MoS₂ [161] and H-BN [162]. The present research further proves the effectiveness of nanosheets with weak interfacial bonding.

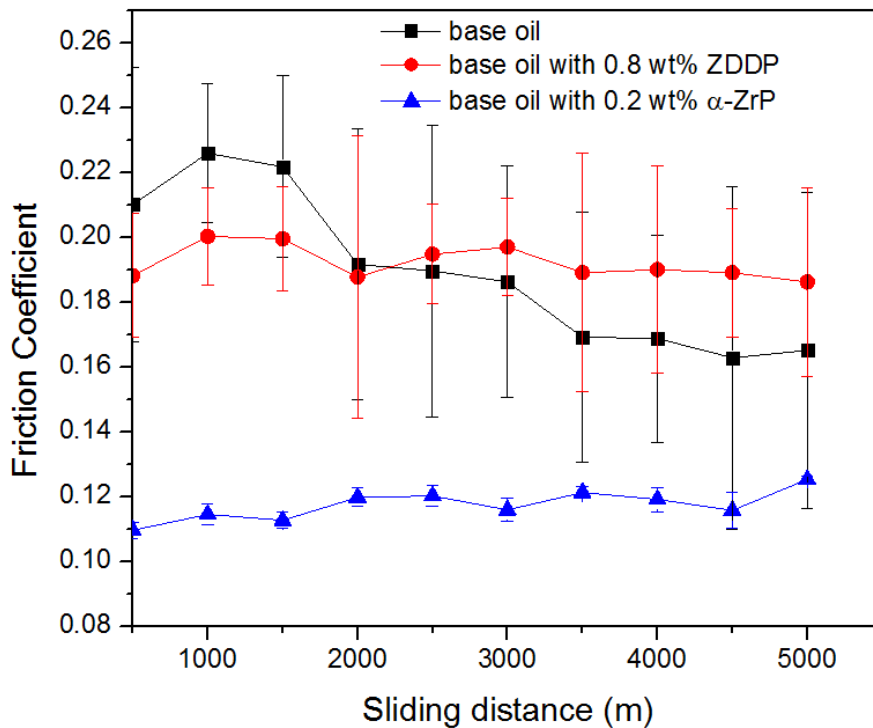


Figure 4.1 Friction coefficient changing with sliding distance

4.1.2 Wear Reduction

The wear of rubbing surfaces with various lubricants was evaluated using optical microscope. Figure 4.2 shows the optical images of the wear scar and wear track. The diameter of the wear scar matches the width of the wear track, indicating stable friction condition. A deep groove appeared on the wear scar of base oil sample with a diameter of 1.47mm. With the addition of ZDDP, wear scar diameter decreased to 1.12 mm and many scratches could be found along with the sliding direction. However, base oil + α -ZrP yielded a much smaller wear scar diameter (~ 0.27 mm).

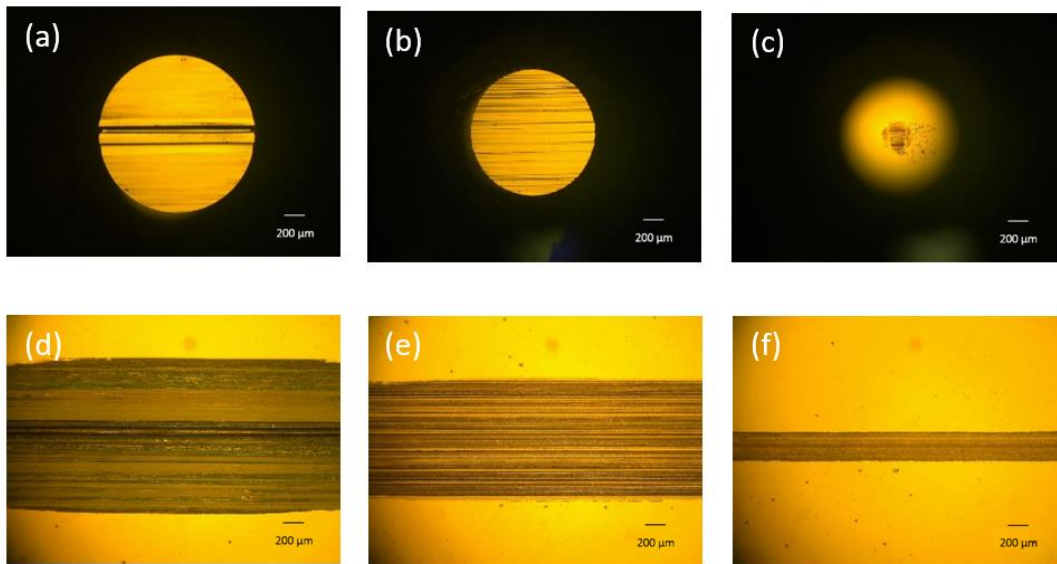


Figure 4.2 Optical image of wear scar and wear track: (a) (d) base oil; (b) (e) base oil + ZDDP; (c) (f) base oil + α -ZrP

To further study the morphology of worn surface, the wear tracks were characterized by SEM, as shown in Figure 4.3. Patch-like surface was observed in the

deep groove of base oil sample, which indicates severe adhesive and abrasive wear. With the addition of ZDDP, no deep groove was observed except some shallow scratches and pits, which suggests less wear. In contrast, the wear track of base oil + α -ZrP exhibits no obvious wear, resulting in a relatively smooth surface.

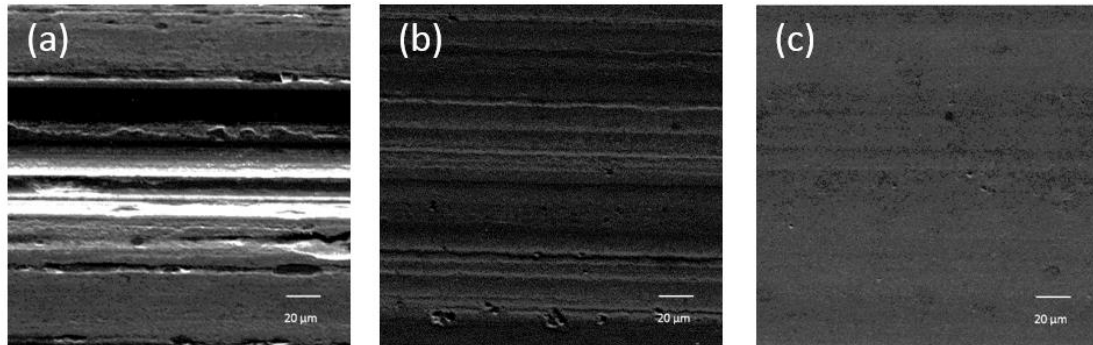


Figure 4.3 SEM image of wear track: (a) base oil, (b) base oil + ZDDP, (c) base oil + α -ZrP

To compare the antiwear properties of ZDDP and α -ZrP quantitatively, wear track volume was measured by profilometer as seen in Figure 4.4. Base oil + α -ZrP shows nearly 30% wear reduction as compared with base oil + ZDDP. Therefore, combining the friction and wear results, α -ZrP shows superior tribological performance.

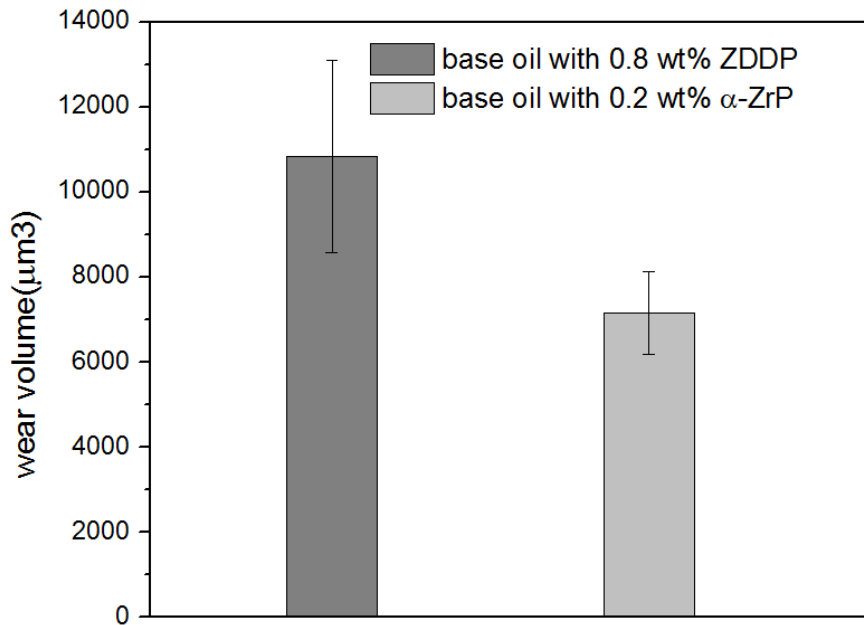


Figure 4.4 Volume of wear track

4.1.3 Lubricating mechanisms

To understand the superior tribological performance of α -ZrP, AFM was conducted on the wear track. The AFM scanning images are shown in Figure 4.5 and include: height images (Figure 4.5a-c), phase images (Figure 4.5d-f), and linear scan surface profiles across the wear track (Figure 4.5g-i). To compare the morphology of the wear track, the average surface roughness (R_a) and root mean square roughness (R_q) are listed in Table 4.2. As shown in Figure 4.5 (a), several grooves and a deep pit could be seen. The depth of the pit-like feature is about 600 nm (Figure 4.5g)). The wear track of base oil gives the highest surface roughness (271.03 nm). The height image of base oil + ZDDP shows fewer asperities than that obtained from the base oil alone with the peak-

to-valley value of 448.3 nm. This surface has a slightly reduced surface roughness of 81.47 nm. The base oil + α -ZrP, on the other hand, has the smoothest surface with no visible asperities. Its phase image shows that this surface is smoother and more uniform than that obtained from base oil + ZDDP (Figure 4.5d-f) with an average surface roughness of 40.89 nm. Based on this observation, both ZDDP and α -ZrP could effectively reduce the surface asperities during the sliding process, but the wear track obtained in base oil + α -ZrP shows significant effect on surface roughness reduction. The low and consistent friction coefficient is most likely to be related to the smooth wear track, as seen in Figure 4.1.

Table 4.2 Surface roughness parameters of the wear track.

Roughness parameter		Base oil	Base oil + ZDDP	Base oil + α -ZrP
Roughness (Sa)	Avg.	271.03 nm	81.47 nm	40.89 nm
Root mean square (Sq)		315.73 nm	97.56 nm	59.02 nm

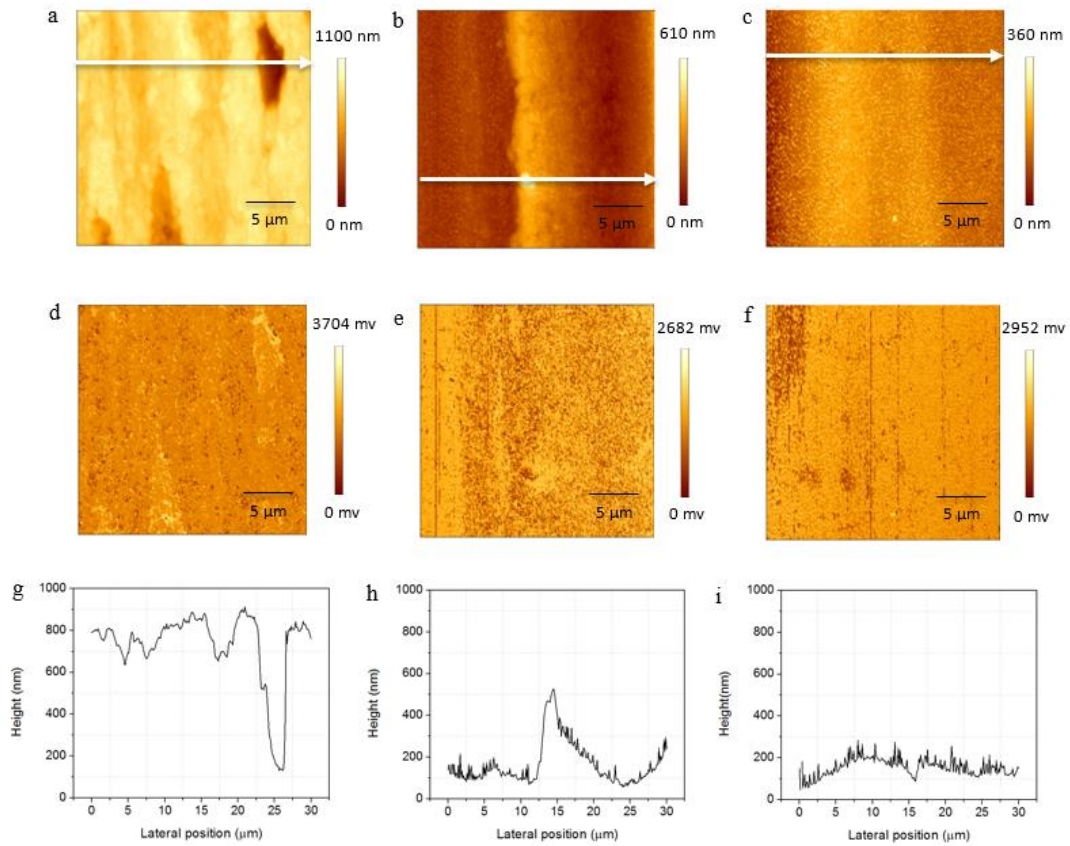


Figure 4.5 AFM height images, phase images and linear scan profiles of the wear track: (a)(d)(g) base oil; (b)(e)(h) base oil + ZDDP; (c)(f)(i) base oil + α -ZrP

In order to analyze the chemical composition of the tribofilm, XPS analysis was conducted on the wear track. Figure 4.6 shows the XPS peaks of C 1s, O 1s, Fe 2p, Zr 3d and P 2p for the tribofilms formed in base oil + α -ZrP. Peaks were deconvoluted using XPSpeak 4.1 with asymmetric Gauss-Lorentz profile after subtracting a Shirley background. The spectrum was calibrated by C 1s peak at 284.6 eV. The iron spectrum can be deconvoluted as Fe 2p_{3/2} and Fe 2p_{1/2}. Two peaks in the Zr spectrum are due to Zr 3d_{3/2} and Zr 3d_{5/2}. Combining the O 1s peak at 529.5 eV and Fe 2p peak at 711.6 eV, the

presence of Fe_2O_3 could be confirmed. The O 1s peak at 529.5 eV and Zr 3d peak at 184.5 eV prove the presence of ZrO_2 [163]. Furthermore, the P 2p peak at 133 eV and Zr 3d peak at 184.5 eV show the existence of $\text{Zr}(\text{PO}_4)_2$ [164]. ZrO_2 and $\text{Zr}(\text{PO}_4)_2$ is a result of tribochemical reaction. Thus the chemical composition of the tribofilm generated on the wear track may be composed of Fe_2O_3 , ZrO_2 and $\text{Zr}(\text{PO}_4)_2$.

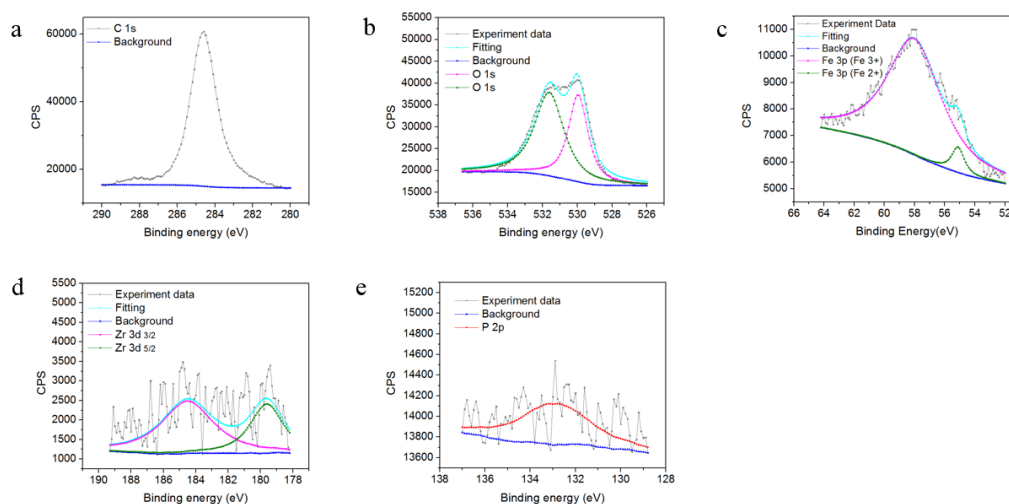


Figure 4.6 XPS spectrum of base oil + α -ZrP wear track. (a) C 1s, (b) O 1s, (c) Fe 2p, (d) Zr 3d and (e) P 2p.

In the following, the mechanisms of tribofilm formation are discussed. The sheet-like nanoparticles of α -ZrP are found to be effective in friction and wear reduction. Due to their two-dimensional nature, the particles entered into the spatial area of contacting surfaces in the boundary lubrication regime. Due to their relatively large size on the disk surface, these particles are expected to effectively carry a load while the weak van der Waals force is responsible for a low shear force. According to the XPS spectra, the

presence of a tribofilm was confirmed with the presence of tribochemical reaction products resulting from the reaction between the lubricant and steel substrate. The composition of ZDDP tribofilm has been studied extensively and its major components are iron oxide, zinc oxide, phosphate compounds and sulfides [165]. In the case of α -ZrP, due to the low phosphorous content (200 ppm), zirconium compounds played an important role in wear protection rather than phosphate compounds. ZrO_2 has been reported as lubricant additives previously, but its tribological performance is worse than ZDDP in terms of friction coefficient and wear volume [166]. In the present work, the superior antiwear performance of the tribofilm is due to the synergetic effect of Fe_2O_3 , ZrO_2 and $Zr(PO_4)_2$. The sheet-like α -ZrP is expected to effectively separate the two contacting surfaces in the boundary lubrication regime, thereby leading to less wear. Moreover, the reduced contact area indicates better load bearing capacity of the tribofilm. The summary comparison of the ZDDP and α -ZrP tribofilms is illustrated in Figure 4.7.

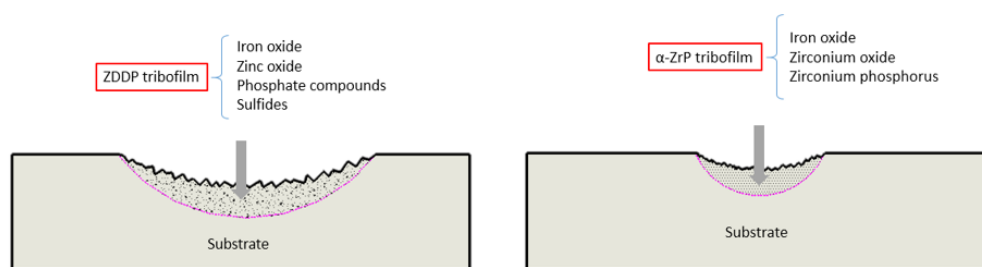


Figure 4.7 Schematic tribofilm composition of ZDDP and α -ZrP

4.2 Roles of V_2O_5 in oil lubrication

Harsh working conditions and technological developments continually call for high-performance lubricants. Additives with a variety of functions are of paramount importance to improve the lubrication performance, such as viscosity modifier, friction modifier and antiwear additives[5]. Developing high efficiency and cost-effective additives are always the goals of tribologists. New additives are always sought after in order to further improve performance and reduce environmental impacts. In an effort to overcome the limitation, the application of nanoparticles as lubricant additives has attracted great attention. Their characteristic size in nanometer length scale allows them to enter the lubrication regime easily and high surface-to-volume ratio leads to rapid chemical reactions. The promising tribological performance makes them favorable candidates for the traditional substances.

The role of nanoparticles in oil lubrication has been reviewed in our recent study [167]. Their tribological performances are found closely associated with the nanoparticles' chemical compositions, sizes, and morphologies. In addition, the correlation coefficient has been calculated to indicate how important each factor is. We found that morphology plays an important role in improving tribological performance in oil lubrication. Among the different morphologies, sheet-like particles show promising effects on friction reduction and wear resistance. The well know examples are graphene[137], MoS_2 [138], h-BN[168], ZrP[124, 169] and Y_2O_3 [139]. The relative motion between the adjacent layers promotes easy slipping between the two counterparts, which in turn provides outstanding lubrication properties.

In the present work, we study the feasibility of using V_2O_5 nanoparticles as potential lubricant additives. Vanadium has various oxide phases, such as vanadium monoxide(VO), vanadium trioxide(V_2O_3), vanadium dioxide(VO_2) and vanadium pentoxide(V_2O_5). Among those, V_2O_5 is most stable. This oxide has been extensively applied to industrial catalysts[170], battery cathodes[171], and electronic devices[172]. V_2O_5 with various nanostructures have been fabricated, including nanosheet[173], nanotube[174], nanowire[172] and nanorods[175]. We chose sheet like V_2O_5 for this study. This type V_2O_5 has a crystal structure composed of multiple V_2O_5 layers stacked via van der Waals force. Each V_2O_5 layer composed of weak V-O bonds[176]. V_2O_5 has been reported as solid lubricants which shows low friction due to the crystallographic slip system[177, 178]. In addition, nanowire V_2O_5 as part of composite coatings shows improved tribological performance[179, 180]. Sheet like V_2O_5 , however, has not been reported as a lubricant additive. In this research, we evaluate the tribological performance of sheet two-dimensional V_2O_5 and its lubricating mechanism. This material was proposed as a potentially effective lubricant additive.

4.2.1 Friction reduction

In order to study the friction performance of V_2O_5 , Stribeck curve was plotted by the coefficient of friction changing with the simplified Sommerfeld number (the ratio of the sliding speed to the load)(Figure 4.8). The standard Sommerfeld number should consider the parameter of fluid viscosity, sliding speed and contact pressure. From the aforementioned viscosity results, the maximum difference is less than 6%. The ratio of

the sliding speed to the load could substitute the standard Sommerfeld number in a tolerable error. X axis has been divided into three lubrication regimes (from left to right) based on lambda value: (I) Boundary lubrication regime ($\lambda < 1$), (II) Mix lubrication regime ($1 \leq \lambda \leq 3$), and (III) Hydrodynamic lubrication regime ($\lambda > 3$). Each regime has been differentiated by background color. In the boundary lubrication regime, the quick drop of friction coefficient could be observed with the increase of simplified Sommerfeld number in all cases. For the light mineral oil samples, friction coefficient was around 0.12. However, with the addition of 0.05 wt% V_2O_5 , friction coefficient could be reduce to 0.1. This is attributed to the effect of nanoparticle sheet-like morphology that is consistent with our previous report [6-8, 21]. In the boundary lubrication regime, surfaces of pin and disk are closely contacted. Due to the rectangular sheet-like morphology, V_2O_5 nanoparticles could lay down on the surface, which could weaken the effect of asperities and valleys. This would lead to lower contact pressure and friction reduction. When the nanoparticles concentration was 0.1 wt%, the minimum friction coefficient could be achieved, which was 25% lower than the base oil. However, 0.2 wt% V_2O_5 shows increased friction coefficient. This is attributed to the agglomeration of nanoparticles. Excessive nanoparticles piled up on the surface increased the fluid drag, which leads to higher friction force[181]. In the mix lubrication regime, the minimum friction coefficient (0.06) was achieved by light mineral oil with 0.05 wt% V_2O_5 , which is 33% lower than the base oil. Higher concentration shows deteriorate results. This could be partly explained through fluidic behavior. According to Figure 4.8, in the mix lubrication regime, relatively low Reynold number corresponds to

laminar flow. The addition of V_2O_5 could reduce the fluid viscosity, which could effectively reduce the momentum transfer between the adjacent fluid layers. In this case, friction could be reduced. Nevertheless, higher concentration would lead to aggregation. Therefore, light mineral oil with 0.1 ~ 0.2 wt% V_2O_5 did not show promising result in this regime. The friction reduction effect seems to be offset by the particles aggregation. In the hydrodynamic regime, the addition of V_2O_5 did not show the friction reduction as much as the other two lubrication regimes. This is attributed to the change of fluidic behavior by nanoparticles. Two friction surfaces were separated by a relatively thick oil film in the hydrodynamic regimes. Unlike the boundary and mix regimes, V_2O_5 would be allowed to transition and rotate freely. In hydrodynamic regime, oil film thickness is larger than 3.6 μm , which will allow free particle rotation. Furthermore, high Reynold number corresponds to turbulent flow. High aspect ratio of V_2O_5 are capable to change the streamline of fluid and makes the flow more stable. It still works under the high Sommerfield number scenario (0.6~0.7). After calculating the overall friction reduction in three regimes, light mineral oil with 0.1 wt% nanoparticles were more efficiency.

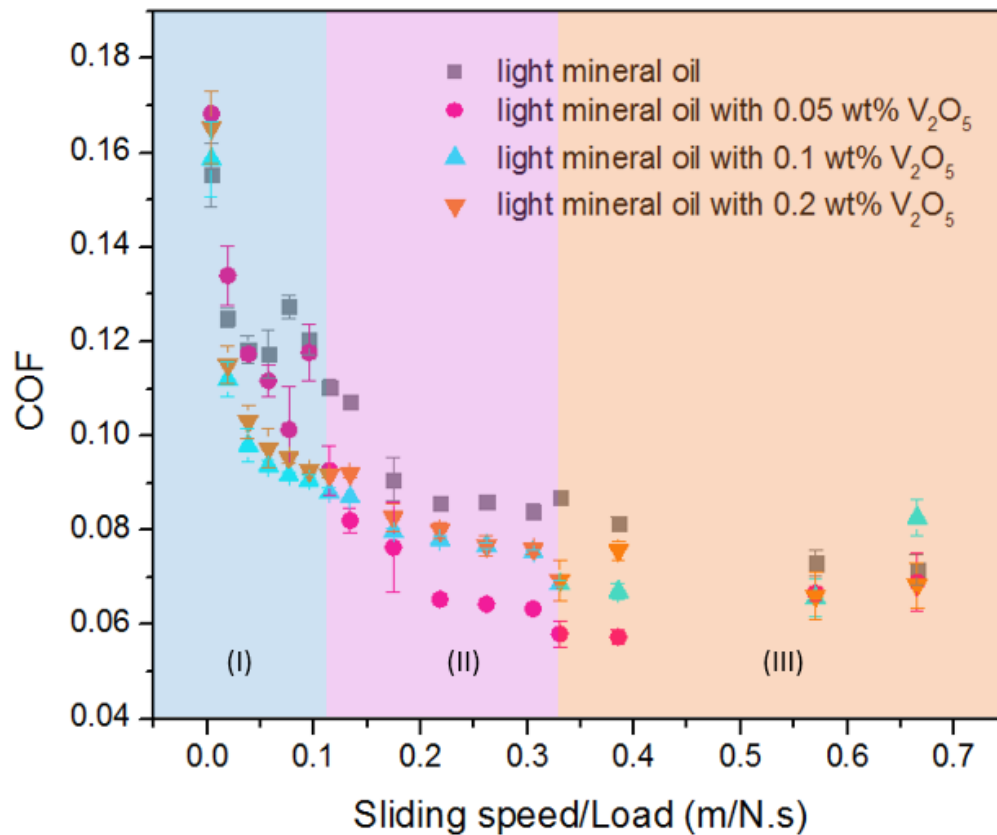


Figure 4.8 Stribeck curve of light mineral oil samples with different concentration V₂O₅

4.2.2 Wear Reduction

In order to study the wear performance, SEM imaging and profiler were conducted on the wear track of all samples. Figure 4.9 shows the surface morphology and corresponding profile of wear tracks. In the case in base oil, both adhesive wear and abrasive wear could be observed as labeled. Adhesive wear shows some debris adhered on the surface while abrasion with visible scratches. A deep groove could be seen at the center where surface underwent the highest contract pressure. Wear track width and

depth from base oil samples are 692 μm and 11 μm respectively. With the addition of 0.05 wt% V_2O_5 , less adhesive wear could be observed at the edge. Surface appeared to be smoother. Wear track width and depth were reduced to 600 μm and 9 μm respectively. The existence of V_2O_5 could effectively avoid the direct contact of friction surfaces. Sheet-like particles possess load-bearing capabilities leading to lower contact pressure. With the increase of additives concentration, shallower groove at the center of the wear track could be observed (Figure 4.9 b ~ d). Moreover, less adhesive wear was observed at the two edges of the wear track. From Figure 4.9(b) to Figure 4.9(d), concentration of V_2O_5 increased from 0.05 wt% to 0.2 wt%. Width and depth of the wear track decreased from 600 μm to 514 μm and 9 μm to 5 μm , respectively. Wear behavior of light mineral oil was greatly improved due to the existence of V_2O_5 .

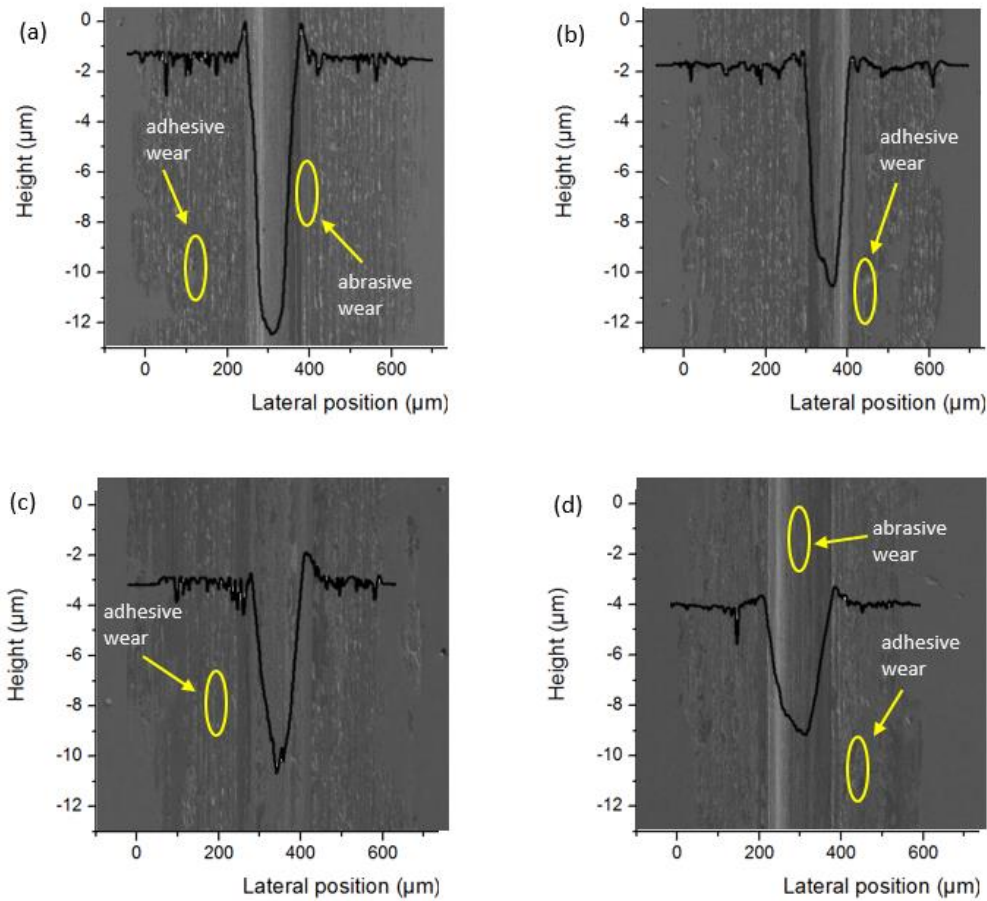


Figure 4.9 Surface morphology and profile of wear tracks from different (a) light mineral oil (b) light mineral oil with 0.05 wt% V_2O_5 (c) light mineral oil with 0.1 wt% V_2O_5 (d) light mineral oil with 0.2 wt% V_2O_5

The antiwear performance was compared qualitatively by measuring the volume of the wear tracks (Figure 4.10). With the addition of 0.05 wt% V_2O_5 , volume of the wear track slightly decreased from 0.00883 mm^3 to 0.0078 mm^3 , compared with the base oil samples. It is 11% wear reduction. With the increase of additives concentration, wear volume was further decreased to 0.00494 mm^3 , which is 44% lower than the volume of base oil sample wear track. In the case of 0.2 wt% V_2O_5 , it shows a similar behavior with the case of 0.1 wt% V_2O_5 . The wear volume is slightly decreased. It seems that 0.1

wt% is the optimized concentration for V_2O_5 in light mineral oil. Higher concentration could not improve the performance any further.

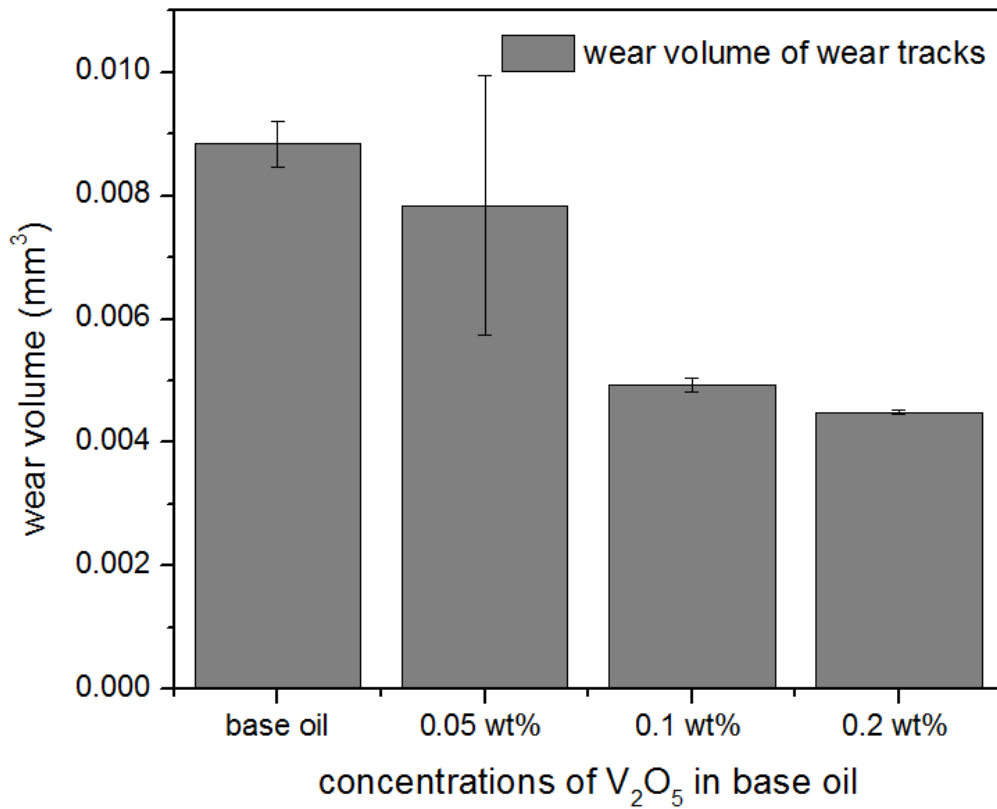


Figure 4.10 Volume of wear tracks from light mineral oil with different V_2O_5 concentrations

4.2.3 Mechanisms

In order to identify the mechanisms of lubrication of V_2O_5 in light mineral oil, Raman spectroscopy was conducted on the wear tracks. Under the heat and high pressure generated in the sliding process, tribochemical reactions might occur on the

surface and results in new molecular bonds. These bonds appear different vibrational frequencies, which corresponds to the characteristic peaks in Raman Spectrum. Figure 4.11 shows the Raman spectrum of wear tracks from different samples. It has been calibrated by a standard silicon sample. Blue line represents the data from the unworn surface. All the wear tracks have been cleaned with ethanol to avoid the residual oil before characterization.

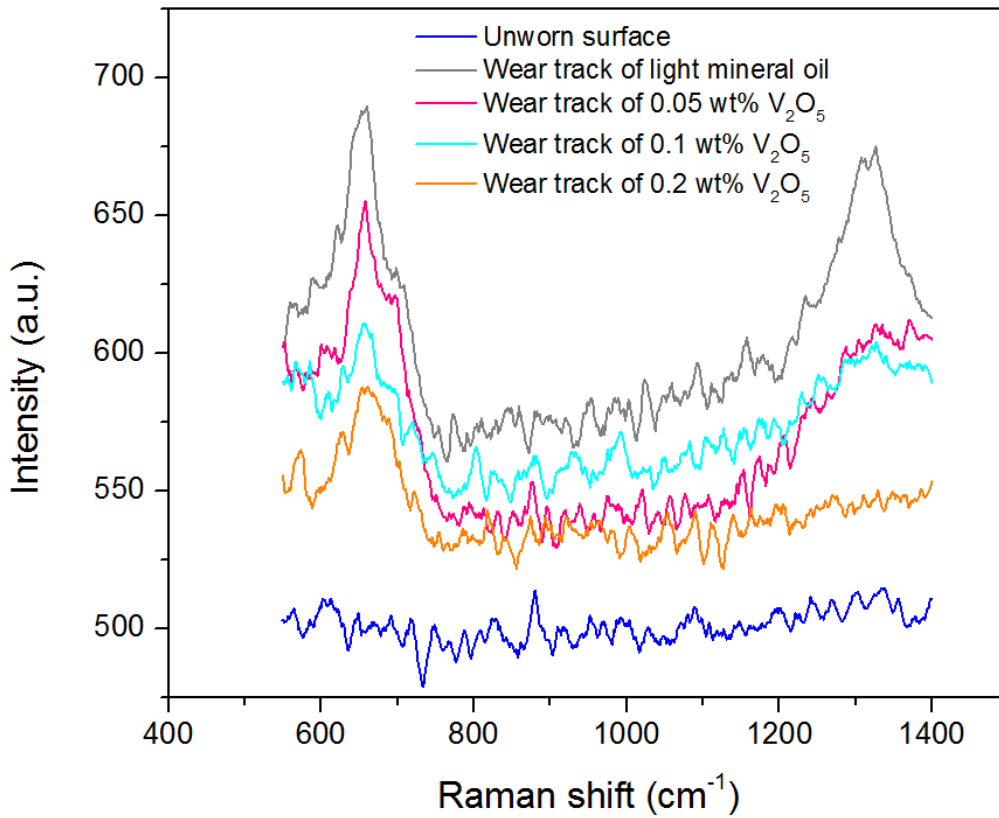


Figure 4.11 Raman Spectrum of wear tracks from different samples

The majority of bearing steel is iron with the rest of chromium, carbon, and magnesium, among others. There is no molecular bond vibration existence in metals, so no characteristic peak could be observed in Raman spectrum of steel. On the other hand, it is proved that the original surface has not been oxidized. From the spectrum of wear track from base oil samples, four characteristic peaks could be found. D band was found at 1312 cm^{-1} . Considering the low carbon content in substrate, sp³ carbon should be attributed to the base oil. Peak center at 605 cm^{-1} was attributed to Cr₂O₃[182], which indicated that the chromium in steel has been oxidized during the sliding process. In addition, peaks at 655.8 cm^{-1} and 705 cm^{-1} are attributed to the molecular vibrations of Fe₂O₃ and Fe₃O₄[183], respectively. Wear track of the base oil was mainly covered the oxides and the reactions occurred during the sliding process could be conclude as follows: $2Cr + \frac{3}{2}O_2 \rightarrow Cr_2O_3$, $3Fe + 2O_2 \rightarrow Fe_3O_4$ and $2Fe + \frac{3}{2}O_2 \rightarrow Fe_2O_3$. After adding 0.05 wt% V₂O₅, peak intensity of Fe₃O₄ and Fe₂O₃ decreased compared with the base oil spectrum, which indicates the less iron oxides deposited on the wear track. When the concentration of V₂O₅ continue increases from 0.1 wt% to 0.2 wt%, peak intensity of Fe₃O₄ and Fe₂O₃ gradually become lower. On the other hand, less sp³ carbon could be observed in the spectrum with the increase of V₂O₅ concentration as well. The deconvolution results of spectrum could be observed in Figure 4.12 and Table 4.3 provides Raman spectrum Peak position comparison of literature and current research. The four characteristic peaks of wear tracks were found to shift to different degree compare to the literature. The peak shift could be due to the elevated temperature and contact pressure induced by the sliding process. In this research, the highest contact

pressure reaches 1GPa, which might induce the stress to the molecular bond vibration. In the boundary lubrication region, asperities from the ball and the disk contacted closely, where high temperature might change the vibrational frequency of the molecular bonds during the sliding process. However, wear track from 0.02 wt% V_2O_5 shows the lowest peak shift compare to others, which means the molecular vibration has not been influenced by the pressure and temperature too much. This could be explained by the effect of nanoparticles morphology. The presence of sheet-like V_2O_5 could weaken the effect of surface asperities, thereby leading to lower contact pressure and working temperature. On the other hand, oxides including Cr_2O_3 , Fe_2O_3 and Fe_3O_4 were found upshifted while D peak was found downshifted. This might be attributed their different molecular vibrational mode and plane. It is worth to mention that the characteristic peak of V_2O_5 , such as 691.1 cm^{-1} and 987.8 cm^{-1} , has not been detected in the wear track. Reasons could be threefold: a) V_2O_5 did not involve the tribochemical reactions during the sliding process; b) concentration of V_2O_5 in base oil is too low to be detected, and c) V_2O_5 involved the tribochemical reactions and existed in the form of intermetallics, which is not sensitive to Raman.

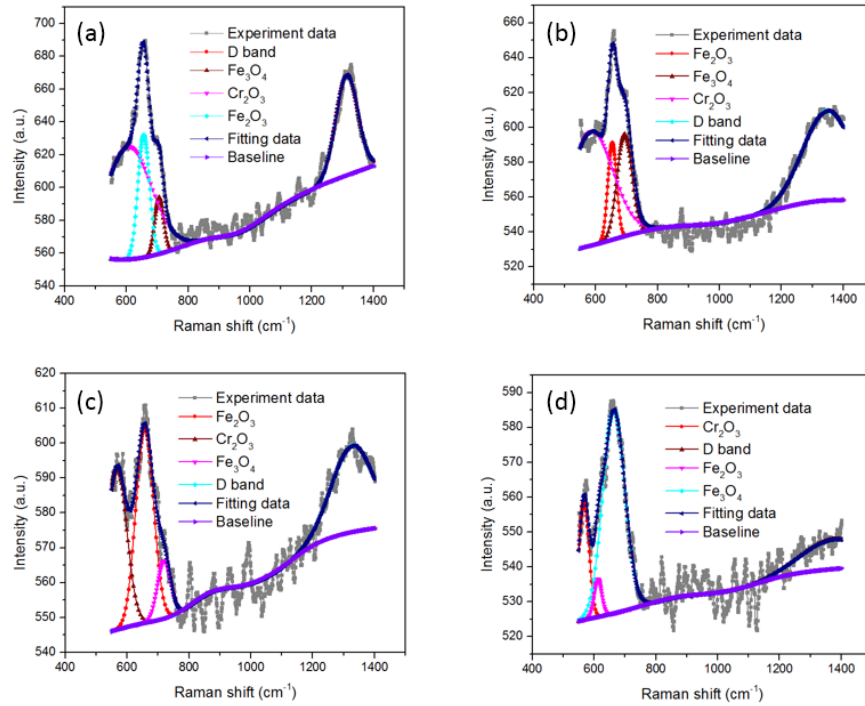


Figure 4.12 Deconvolution results of Raman spectrum from different wear tracks: (a) Base oil, (b) Base oil + 0.05 wt% V_2O_5 , (c) Base oil + 0.1 wt% V_2O_5 (d) Base oil + 0.2 wt% V_2O_5 .

Table 4.3 Raman spectrum Peak position comparison of literature and current research

Wear tracks from different samples	Raman peaks assigned to	Peak position in the literature	Peak position in current research
Base oil	Cr_2O_3	553 cm^{-1} [182, 184]	605.4 cm^{-1}
	Fe_2O_3	612 cm^{-1} [185, 186]	655.9 cm^{-1}
	Fe_3O_4	662 cm^{-1} [185, 186]	705.7 cm^{-1}
	Carbon sp ³ (D peak)	1350 cm^{-1} [187]	1312.7 cm^{-1}

Table 4.3 Raman spectrum Peak position comparison of literature and current research, continued.

Base oil + 0.05	Cr ₂ O ₃	553 cm ⁻¹ [182, 184]	586.9 cm ⁻¹
wt% V ₂ O ₅	Fe ₂ O ₃	612 cm ⁻¹ [185, 186]	653.7 cm ⁻¹
	Fe ₃ O ₄	662 cm ⁻¹ [185, 186]	692.9 cm ⁻¹
	Carbon sp ³ (D peak)	1350 cm ⁻¹ [187]	1349.3 cm ⁻¹
Base oil + 0.1	Cr ₂ O ₃	553 cm ⁻¹ [182, 184]	567.4 cm ⁻¹
wt% V ₂ O ₅	Fe ₂ O ₃	612 cm ⁻¹ [185, 186]	656.9 cm ⁻¹
	Fe ₃ O ₄	662 cm ⁻¹ [185, 186]	719.3 cm ⁻¹
	Carbon sp ³ (D peak)	1350 cm ⁻¹ [187]	1305.6 cm ⁻¹
Base oil + 0.2	Cr ₂ O ₃	553 cm ⁻¹ [182, 184]	567.1 cm ⁻¹
wt% V ₂ O ₅	Fe ₂ O ₃	612 cm ⁻¹ [185, 186]	612.3 cm ⁻¹
	Fe ₃ O ₄	662 cm ⁻¹ [185, 186]	663.6 cm ⁻¹
	Carbon sp ³ (D peak)	1350 cm ⁻¹ [187]	1347.7 cm ⁻¹

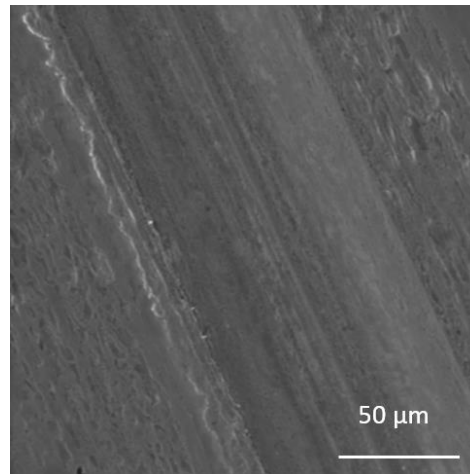


Figure 4.13 EDS scan area of wear track from Base oil + 0.2 wt% V_2O_5 .

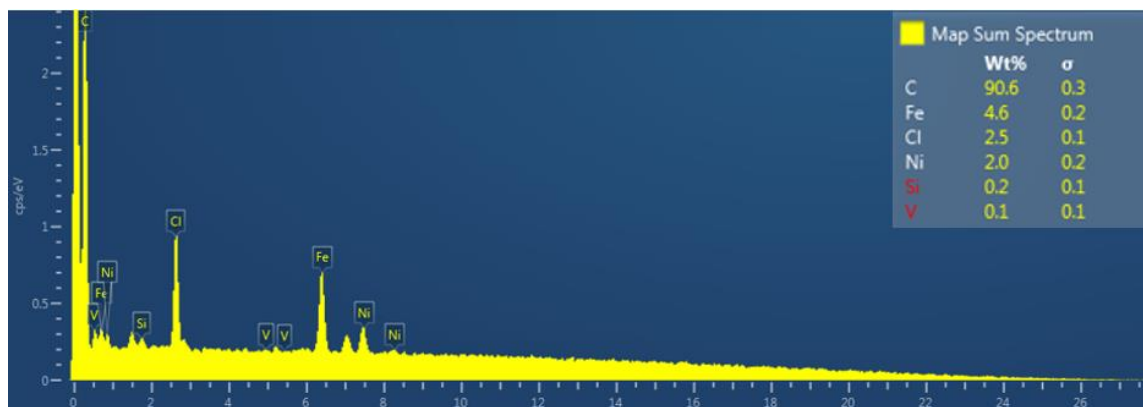


Figure 4.14 EDS spectrum of wear track from Base oil + 0.2 wt% V_2O_5 .

Effects of nanoparticles on lubrication likely involve physical and chemical interactions. Physical interaction includes the effect of particle's shape, rolling contact, sliding contact, adsorption film formation. Chemical interaction includes the tribochemical reactions. Sheet like nanoparticles were found to improve lubrication performance, such as graphene, h-BN, MoS_2 . In this case, the sheet like morphology of nano V_2O_5 should be beneficial to its antiwear properties. Other than that, V_2O_5 was

found to inhibit corrosion in the literature[188, 189]. The addition of V_2O_5 would facilitate the formation of stable structure on the substrate interfacial, which improved the corrosion resistance significantly[188]. V_2O_5 could react with the substrates and formed intermetallic alloy V-Fe-Cr. It works as an interfacial physical barrier to further alloy penetration[189]. In this research, low background of the spectrum indicates less oxidation of the wear track. It seems that the existence of V_2O_5 prohibits the oxidation process of the steel surface. This result indicated the promising antiwear performance. Figure 4.15 shows the illustration of V_2O_5 lubricating mechanism.

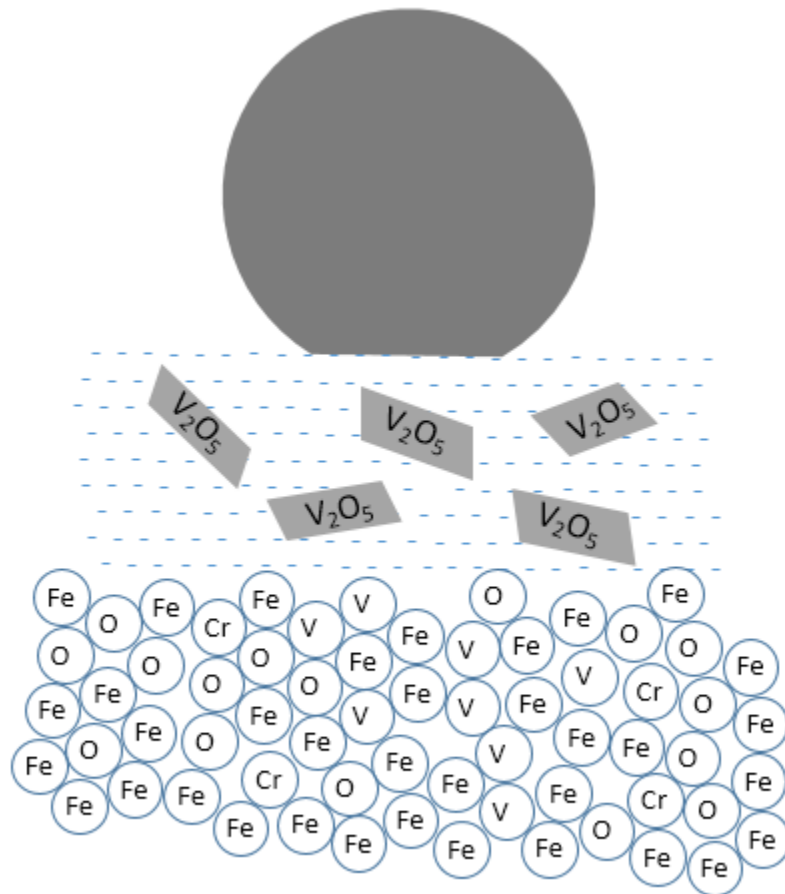


Figure 4.15 Illustration of the lubricating mechanism of V_2O_5

4.3 Summary

In the first section, an alternative nanolubricant is developed to replace commercial ZDDP-containing lubricants. We investigated the effects of α -ZrP nanoparticles as additives in lubricants. Tribological studies were carried out using a pin-on-disk configuration in a reciprocating motion. Experimental results showed superior tribological performance of the sheet-like nanoparticles: when compared with ZDDP, α -ZrP showed 50% reduction in friction and 30% in wear. XPS spectroscopic analysis

indicates that a uniform anti-wear tribofilm composed of Fe_2O_3 , ZrO_2 and $\text{Zr}(\text{PO}_4)_2$ is formed. This zirconium based tribofilm is characterized by a lower surface roughness and improved load bearing capability than ZDDP tribofilm. The low-phosphorous-content-lubricant additives have strong potential as a substitute for ZDDP.

In the second section, the feasibility of using V_2O_5 nanoparticles as a lubricant additive has been studied. Rheological properties and tribological performance show promising results. The amount of 0.2 wt% V_2O_5 could reduce the viscosity of base oil for 5.9%. According to the experimentally generated Stribeck curve, light mineral oil with 0.1 wt% V_2O_5 shows the lowest overall friction coefficient. Viscosity and friction reduction were found being attributed to its sheet like morphology. In the case of antiwear performance, 0.2 wt% V_2O_5 shows the lowest wear rate, which is 44% reduction compare to the base oil. Through Raman spectrum and EDS analysis, it has been postulated that vanadium oxide nanoparticles interacted with steel surface forming intermetallic alloy V-Fe-Cr resulting in enhancement of wear protection.

CHAPTER V

IN SITU CHARACTERIZATION OF NANOPARTICLE-ENHANCED GROWTH OF TRIBOFILMS³

This chapter investigates the kinetics of a tribofilm formed on a pair of bearing steels (E52100). Strategically-selected-illuminative nanoparticles of NaYF₄ were added to a base oil in order to enable their tracking. Electrical conductivity was monitored during sliding that was found to be linked to the state of the interface and the tribofilm. Further characterization identified tribochemical reaction products of Y₂O₃ that exhibited superior tribological performance. In comparison with mineral oil as the base lubricant, the addition of NaYF₄ resulted in the reduction of wear of 82%. This work discovered three stages to form a tribofilm: running in, reactive, and growth. Interestingly, the formation of a tribofilm was more dominated by frictional force than applied load. This is significant because we can now use alternative strategies to generate quality tribofilms.

5.1 Tribofilm formation

In order to observe the status of the tribofilm, we firstly tracked the evolution of friction and contact resistance against time. Results of the base oil and the base oil + 1

³ Part of this chapter is reproduced by permission of "*In situ* Investigation of the Growth of a Tribofilm Consisting NaYF₄ Fluorescent Nanoparticles" by Wei Dai, Yunyun Chen, Kyungjun Lee, Alexander M. Sinyukov, Masfer Alkahtani, Philip R. Hemmer and Hong Liang. *Tribology Transactions*, *accepted* (2017). (Copyright © 2017 Informa UK Limited, all rights reserved)

wt% NaYF₄ are shown in Figure 5.1. In the case of base oil (Figure 5.1 (a)), friction coefficient was found to increase linearly to 0.32 from 0 to 25 min. It then fluctuated from 25 min to 50 min. Eventually, it decreased gradually after 100 min. The decrease in friction was due to the formation of a tribofilm and its composition would be revealed by Raman spectrum discussed in the tribochemical interaction section. Simultaneously, contact resistance fluctuated from 0 min to 100 min and was then followed by a sharp increase from 0.3 Ω to 25 Ω within 12 min. After sliding for 130min, contact resistance of base oil samples turned out to be stable. The value was around 100 Ω . Likewise, NaYF₄ demonstrated a similar trend with base oil (Figure 5.1 (b)). However, the friction coefficient of NaYF₄ was lower than that of the base oil, while contact resistance was much higher. Further investigation was carried out and discussion was provided next.

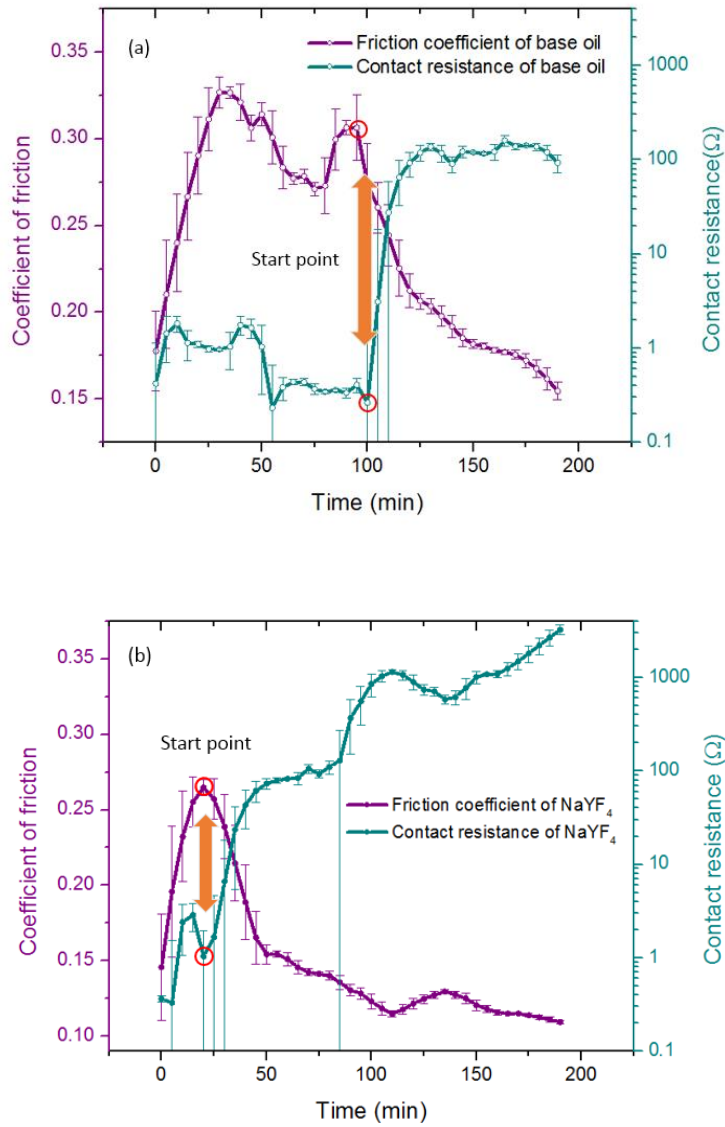


Figure 5.1 Friction coefficient and contact resistance change during the sliding process: (a) base oil (b) base oil + 1 wt% NaYF₄.

5.2 The performance of a tribofilm

5.2.1 Friction reduction

Interestingly, the correspondence between friction coefficient and contact resistance was observed as shown in Figure 5.1. When there was an increase (or

decrease) in friction, a decrease (or increase) of the contact resistance was observed accordingly. The change in friction could be due to the tribofilm formed on the wear track. There is an inverse correlation between friction coefficient and contact resistance. The quantitative relationship was revealed in Figure 5.2. In the case of base oil, the friction coefficient shows a linear correlation with the contact resistance. A higher contact resistance leads to lower friction. However, the contact resistance of the system containing NaYF₄ shows a logarithmic correlation with friction. When the contact resistance is higher than 100 Ω , friction tends to be stable. Such different correlation indicates potential variation in the characteristics and performance of tribofilms.

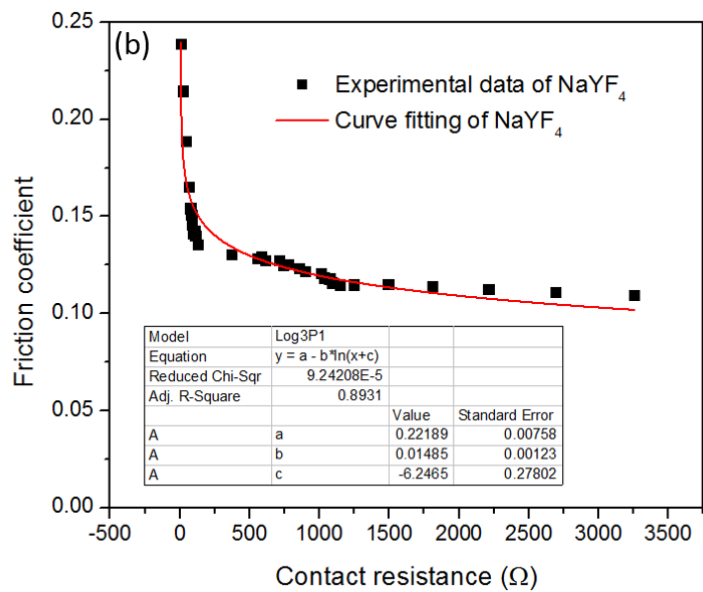
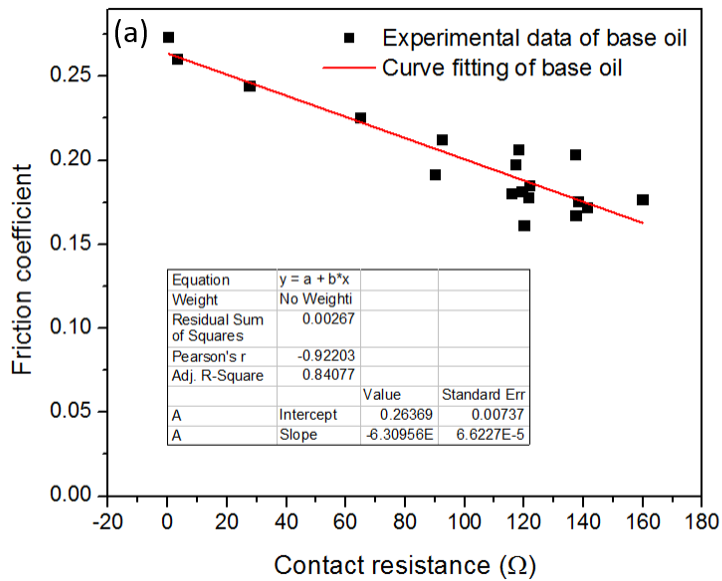


Figure 5.2 Correlation between the friction coefficient and contact resistance: (a) base oil (b) base oil + 1 wt% NaYF₄.

5.2.2 Wear reduction

To understand the nature of tribofilms, SEM characterization was conducted on the wear track. Figure 5.3 shows the SEM images and cross sectional profile of the wear track obtained through base oil with a series of NaYF₄ concentrations. Lower magnification images show the whole picture of wear track while higher magnification images exhibit the surface morphology of center and edge of the wear track. According to the result of base oil (Figure 5.3 (a) (b) (c)), a deep groove could be observed from the center of wear track with the characteristics of severe abrasive wear. The edge of wear track seems to have been subjected to severe adhesive wear with the evidence of material removal and deformation. The width of the wear track is 550 μm . With the addition of 0.3 wt% NaYF₄ (Figure 5.3 (d) (e) (f)), the deep groove disappeared and less abrasive and adhesive wear was seen. When additive concentration reached 0.6 wt% (Figure 5.3 (g) (h) (i)), the width of the wear track was reduced to 408 μm and the dominant mode was abrasive wear. When the concentration further increase to 1 wt% (Figure 5.3 (j) (k) (l)), a smaller width of wear track could be overserved and wear track surfaces were very smooth. As a result, the sample with 1 wt% NaYF₄ demonstrates the best antiwear performance in terms of wear track width and surface morphology. Wear volume could be reduced as much as 82% compared with the base oil, as shown in Figure 5.4. The following discussion will focus on the base oil with 1 wt% NaYF₄, since it demonstrates the best tribological performance. It is noted that we did not provide wear scar images due to their similar surfaces with smooth morphology and matching diameter with the width of wear tracks.

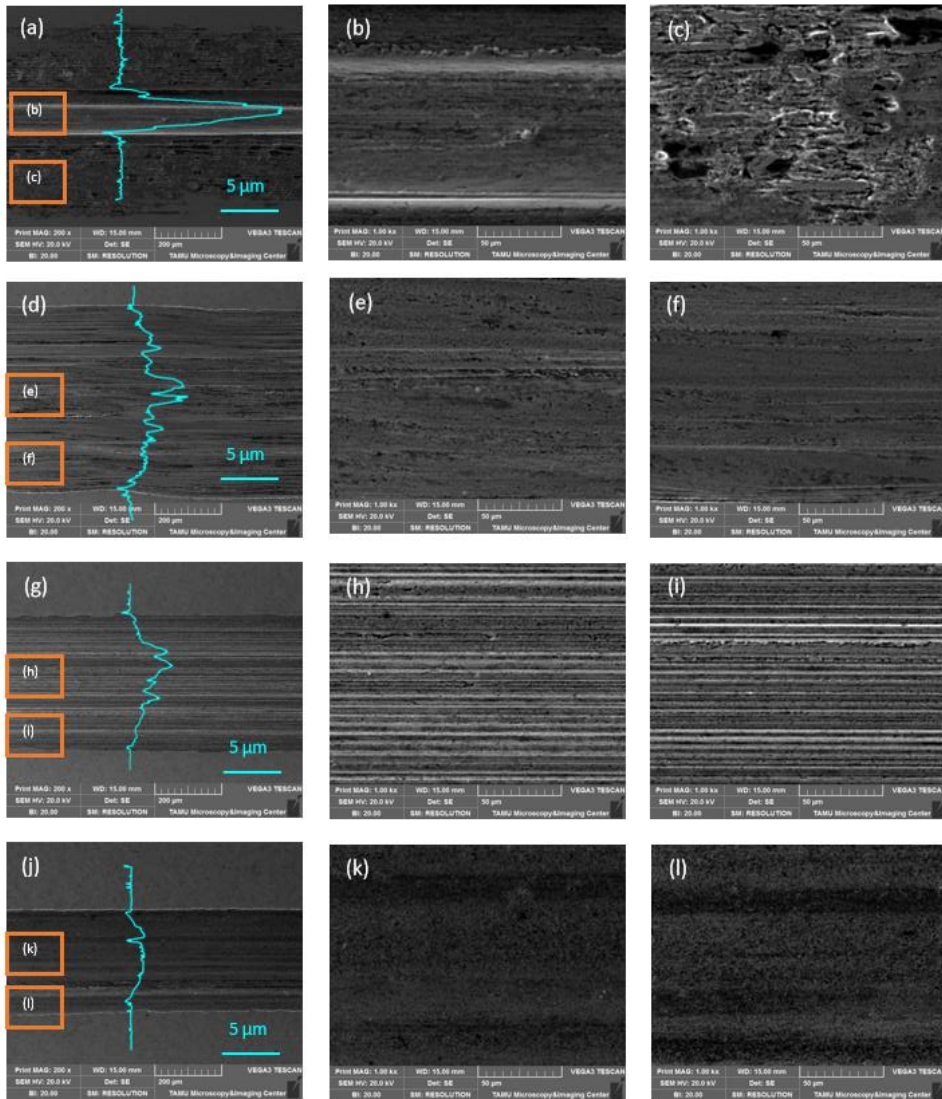


Figure 5.3 SEM images and cross section profile of wear track from samples with different NaYF_4 concentration. (a) base oil (d) base oil + 0.3 wt% NaYF_4 (g) base oil + 0.6 wt% NaYF_4 (j) base oil + 1 wt% NaYF_4 . (b)(e)(h)(k) and (c)(f)(i)(l) show the center and edge images of the corresponding wear tracks under higher magnification.

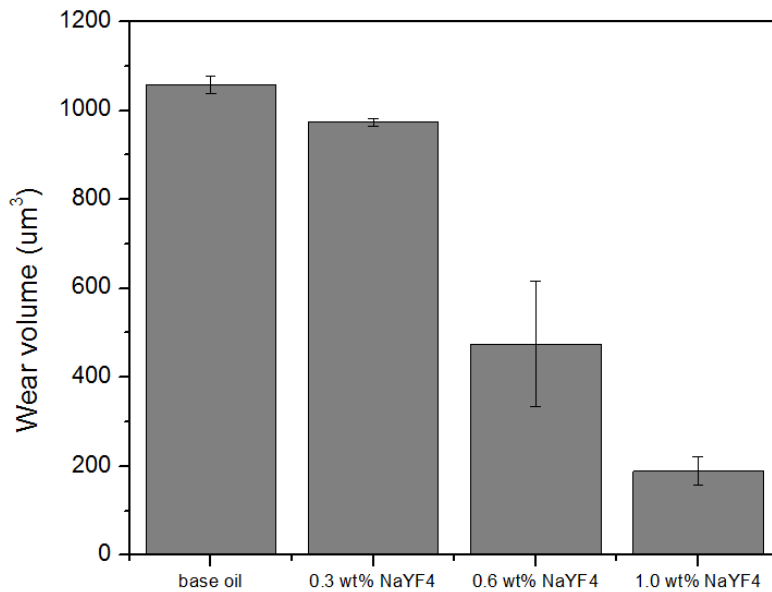


Figure 5.4 The wear volume of wear tracks of base oil containing NaYF₄ with various concentrations.

5.2.3 Sliding-induced redistribution of nanoparticles

Because of their illuminating properties, NaYF₄ nanoparticles were observed using a laser confocal scanning microscope and their distribution was mapped throughout sliding, as shown in Figure 5.5. This figure exhibits the wear track images of base oil containing 1 wt% NaYF₄ after sliding up to 3 hrs. Blue color shows higher intensity while red color shows lower intensity (unit a.u.). Due to the fluorescence properties of NaYF₄, light intensity reflects the concentration of nanoparticles. Blue or red colors correspond to the high or low concentration of NaYF₄, respectively. At the initial state, sliding at 0 hr, uniformly distributed nanoparticles were observed on the surface. After sliding for 0.5 h, light intensity of inside of wear track appeared higher than that outside the wear track. After sliding for 3 hrs, light intensity difference between

that on wear track and outside was more significant, indicating less particles inside of the wear track. They clearly show the evolution of nanoparticles distribution during the sliding process. For the base oil and samples with lower concentrations, the distribution of nanoparticles could not be seen clearly due to the low fluorescence intensity. These images proved that NaYF₄ was gradually consumed with the increase in sliding distance. This might be the result of the tribochemical reaction that occurred during the sliding. To prove this, further investigation was conducted.

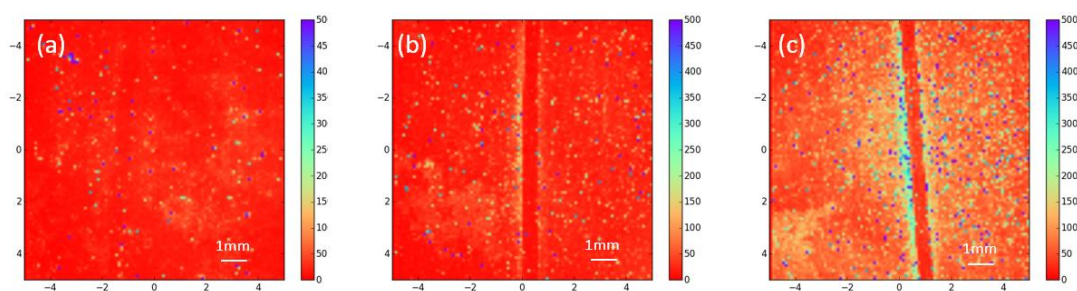


Figure 5.5 Confocal scanning microscope images of wear track of base oil + 1 wt% NaYF₄ after different sliding distance: (a) 0 h (b) 0.5 h (c) 3 h.

To prove the motion of nanoparticles, EDS was conducted on the wear track of base oil + 1 wt% NaYF₄. The EDS spectrum (Figure 5.6) revealed that the wear track, i.e., where the tribofilm was formed containing C, Fe, O, and Y. The C and Fe are attributed to the substrate while Y comes from nanoparticles. It indicates that NaYF₄ might be broken down due to tribochemical reaction during sliding.

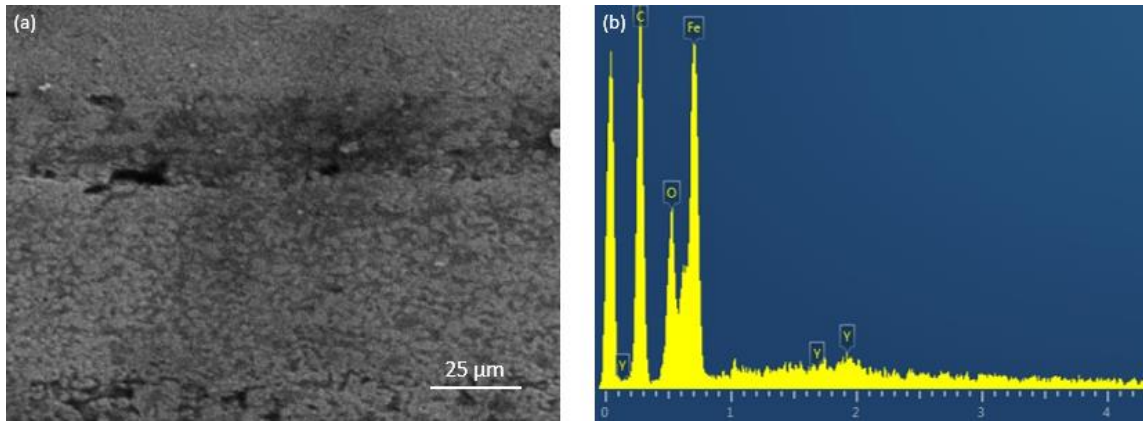


Figure 5.6 EDS spectrum of wear track of base oil + 1 wt% NaYF₄ (a) SEM image of wear track (b) EDS spectrum.

5.3 Tribochemical interaction

In order to identify the tribochemical reactions occurred in sliding process, Raman was conducted on the wear track. Figure 5.7(a) and (b) show the spectrum deconvolution of base oil and base oil containing 1 wt% NaYF₄. In the case of base oil, characteristic peaks of 545 cm⁻¹, 655 cm⁻¹, 1145 cm⁻¹ and 1325 cm⁻¹ correspond to Cr₂O₃, Fe₃O₄, C-C and Fe₂O₃ respectively[182, 184-186, 190]. Among them, Cr₂O₃, Fe₃O₄ and Fe₂O₃ are the products of tribochemical reactions while C-C is attributed to the mineral oil. In the case of NaYF₄, the tribofilm contained not only Cr₂O₃, Fe₃O₄, C-C and Fe₂O₃, but also characteristic peaks of Y₂O₃ and oleic acid. Peaks located at 655 cm⁻¹, 706 cm⁻¹ could be found in the fluoresce spectrum of Y₂O₃[191-194]. In addition, peak located 900 cm⁻¹(C=O), 980 cm⁻¹(C=C), 1067 cm⁻¹(C-C), and 1262 cm⁻¹(C-C) could be attributed to oleic acid[195-197]. Y₂O₃ has a 2D morphology. The van der Waals force between adjacent layers of Y₂O₃ will enable the relative motion during the sliding process, which is beneficial to improve lubrication [139, 193]. The formation of Y₂O₃ in

the tribofilm could explain the superior tribological performance of NaYF₄. On the other hand, Y₂O₃ itself is not luminescent such that it will not affect the NaYF₄ distribution measurement during sliding. Figure 5.7(c) and (d) show wear track spectrum of both cases after sliding for 0.5h, 1h, 2h and 3h respectively. In the case of base oil, peak intensity of Fe₃O₄ and Fe₂O₃ increased with time from 0.5 h to 2h while spectrums of 2h and 3h were similar. It indicates that the tribofilm of base oil started to grow from 0.5h to 2h and became stable after 2h. However, based on the deconvolution results, peaking intensity of Y₂O₃ was found continued increase. This leads to the spectrum change on wear tracks obtained through NaYF₄ sliding for 0.5h to 3h. The continued growth of the tribofilm in the duration from 0.5h to 3h resulted in higher contact resistance and a thicker film.

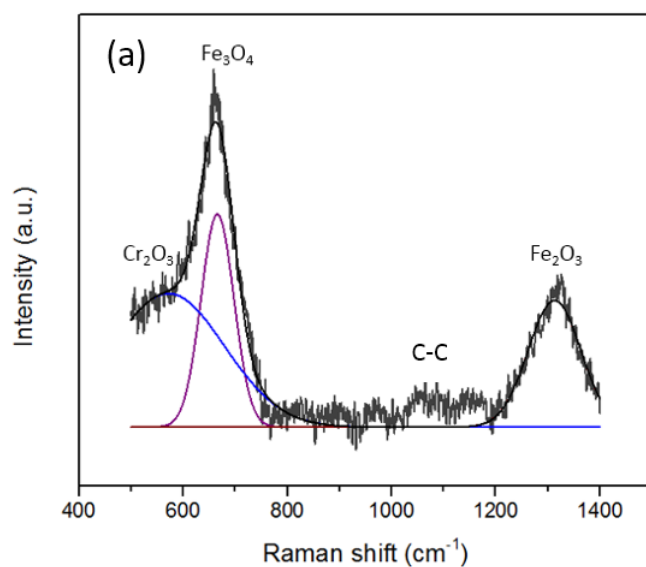


Figure 5.7 Raman spectrum of the wear track (a) deconvolution of base oil wear track spectrum (b) deconvolution of base oil + 1 wt% NaYF₄ wear track spectrum (c) wear track spectrum of base oil after sliding for 0.5h, 1h, 2h and 3h (d) wear track spectrum of base oil +1 wt% NaYF₄ after sliding for 0.5h, 1h, 2h and 3h.

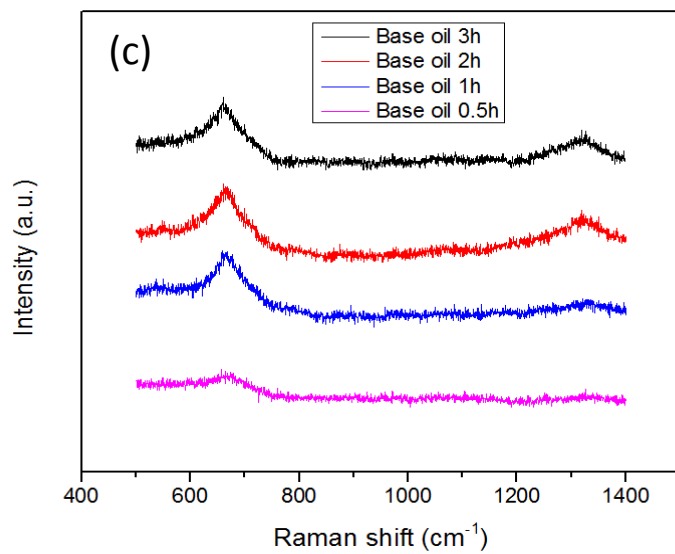
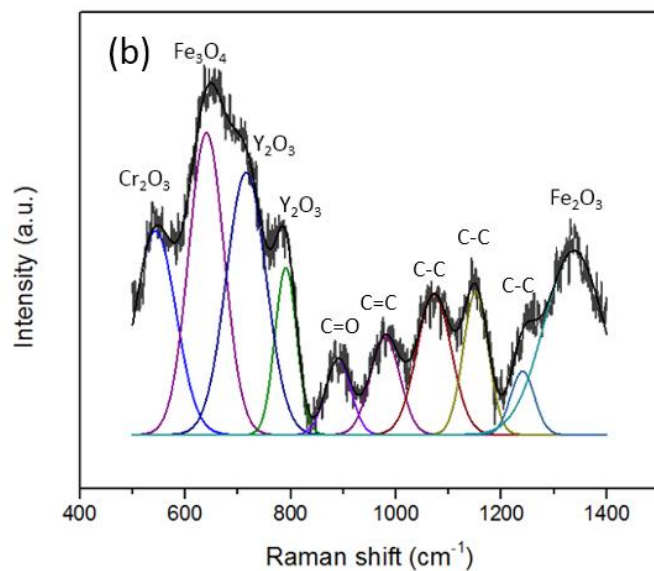


Figure 5.7 Continued.

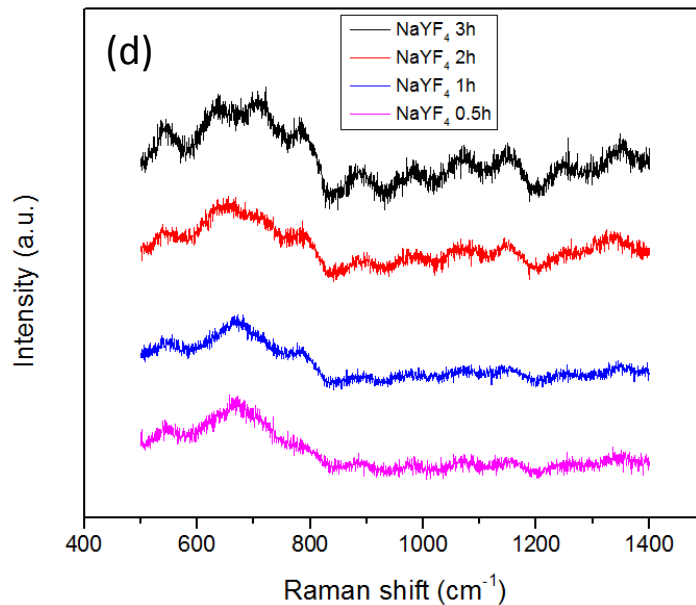


Figure 5.7 Continued.

5.4 Kinetics of tribofilm formation

The kinetic mechanisms of tribofilm formation and growth are discussed in this section. According to Figure 5.1, the start point of the tribofilm formation for a base oil and a base oil + NaYF₄ have been labeled. In case of base oil, the film started to form at 100 min, while the system containing NaYF₄ nanoparticles showed formation at 25 min. This means that the tribofilm formation is accelerated by NaYF₄ for at least four times than that in base oil. In addition, we could observe that when the contact resistance reaches 100 Ω , it became stable. In case of base oil, the final contact resistance will be stable at around 100 Ω with the increase in sliding distance, while in case of NaYF₄, the contact resistance continued to increase. Even after reaching a high value of 1,000 Ω , the resistance continued to increase. The high contact resistance reflects the nature of the

tribofilm. Raman characterization earlier showed evidence of oxide Y_2O_3 . The more oxide and thicker layer, the higher contact resistance. The tribofilm formed through $NaYF_4$ resulted in the decrease in friction coefficient.

Based on discussion above, the correlation of friction (f) and contact resistance (R) of tribofilm containing $NaYF_4$ could be formulated as: $R \propto \exp(-f)$. The contact resistance reflects the formation of a tribofilm, which is the product of tribochemical reaction. The value of resistance is related with the materials and shape: $R = \rho l / A$, where ρ is the electrical resistivity of the material, l is the length and A is the cross-sectional area. On the other hand, friction is an energy dissipation process. The physical meaning can be explained as $NaYF_4$ derived tribochemical reaction is induced by input mechanical power during sliding. In order to prove this, the correlation between reaction rate and mechanical power was obtained as shown in Figure 5.8. The tribochemical reaction rate was calculated as the first derivative of contact resistance versus time. Based on our previous study, we assume the reaction rate is uniform on the wear track [169]. Moreover, mechanical power was calculated as the product of frictional force and sliding speed. Correlating with the results shown in Figure 5.8, it was found that at the moment when the mechanical power achieved 0.015w, tribofilm started to form and then grow at a high reaction rate. However, the continuously increased mechanical power would lead to the excessive removal of the tribofilm. This indicates two competing mechanisms, the tribofilm formation and subsequent wear. This process is important to maintain a kinetically balanced tribofilm that undergoes formation, tribochemical interaction, and wear. A question arose regarding the surface morphology

of the tribofilm. Based on the SEM images of the wear track, and our previous study[169], the effects of roughness is believed to take lesser role because of the smooth surface. The higher the surface roughness, the higher the contact resistance, and the higher the friction coefficient. In our results, however, the COF becomes lower as soon as the tribofilm is formed. This is consistent with our previous study [169] where the roughness of a tribofilm formed due to addition of nanoparticles was around 50 nm. The addition of nanoparticles will not increase the surface roughness of the wear track. Our results proved otherwise. It means that the surface roughness of a tribofilm formed NPs would not increase during the sliding.

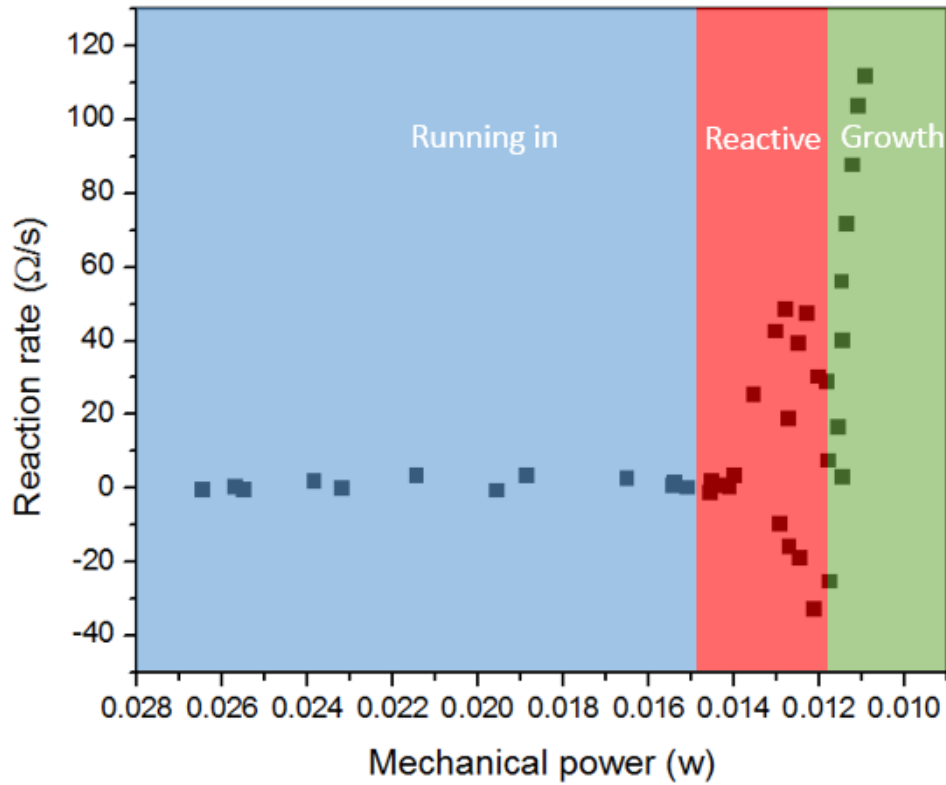


Figure 5.8 NaYF₄ derived tribochemical reaction rate as a function of input mechanical power.

To better understand the behavior in the reactive regimes, further data analysis was conducted. The running in and growth regimes were dominated by the tribofilm removal and formation, respectively. However, the reactive regime was the synergic effect of both removal and formation. The data in the reactive regime could be decomposed to two curves: one is for tribofilm removal and the other is for tribofilm formation, as shown in Figure 5.9. With the decrease of mechanical power, the removal effect was weaker while the formation effect was stronger.

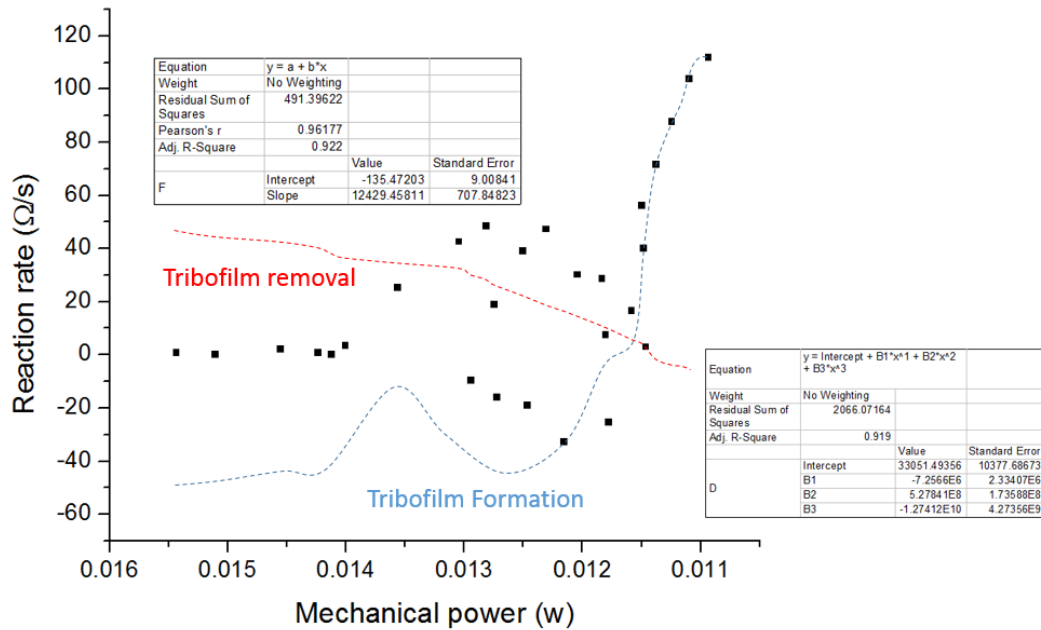


Figure 5.9 The formation and removal of tribofilm in the reactive regime

In order to understand the effects of contact pressure and/or shear stress on the fate of tribofilm, we further analyzed the results. The contact pressure was estimated using Hertzian contact theory while the surface shear stress was calculated using measured frictional force divided by the contact area. Results are shown in Figure 5.10(a). It is apparent and understandable that the contact pressure was found to decrease with time. While the frictional shear stress increased at the beginning due to running-in period, and then decreased continuously (as shown in Figure 5.10(a)). Figure 5.10(b) shows the 3D plot of NaYF₄ contact pressure, shear stress and reaction rate against time. At the beginning, i.e., the running period, the reaction rate was low due to

the dominance of material removal under a high contact pressure and shear stress. After the running period, the tribofilm formation and materials removal were competing with each other, entering the second stage where the contact pressure and shear stress were found fluctuating. In this period, tribochemical interaction was continuously triggered as evidenced in the increased electrical contact resistance. The high resistance means more oxides or ceramics to be formed due to tribochemical reactions. One interesting ephemeron was observed that the surface frictional shear stress correlates the reaction rate much more closely than that of contact pressure. This indicates that the tribochemical reactions and subsequent tribofilm formation are dominated more by rubbing than applied force. This is different from what has been previously reported[198].

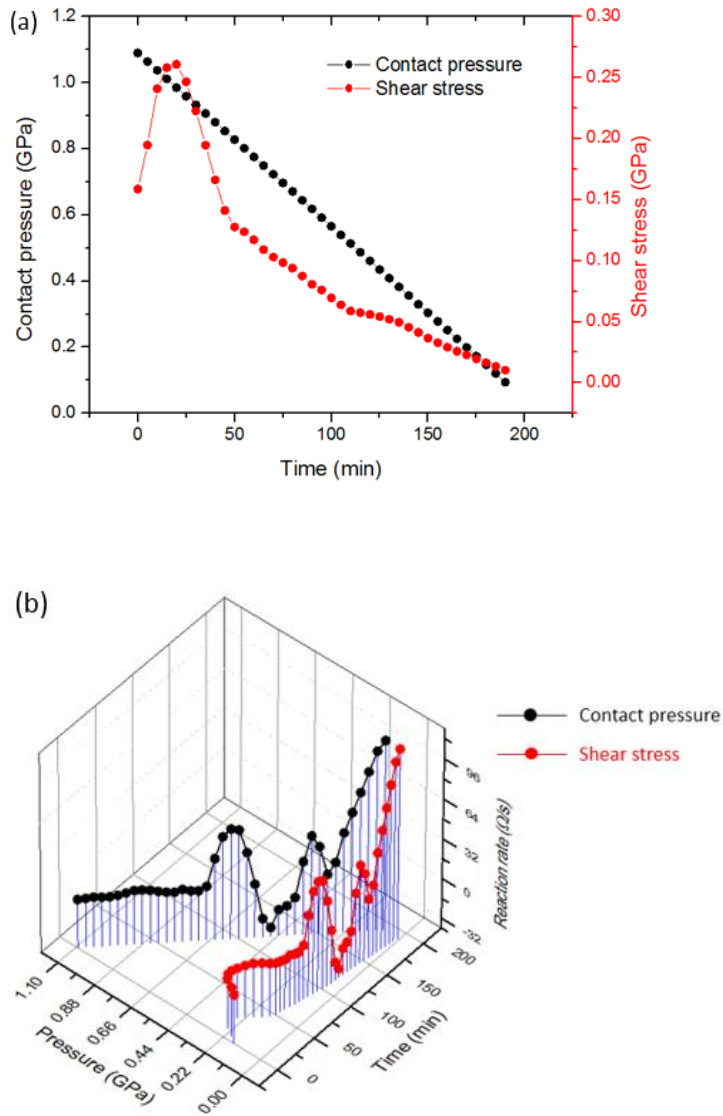


Figure 5.10 NaYF₄ contact pressure and shear stress as a function of sliding time. (b) NaYF₄ 3D plot of contact pressure, shear stress and reaction rate changing with sliding time.

Based on the discussion above, the nature of formation and growth tribofilms can be illustrated in Figure 5.11. There are three characteristic stages of the evolving tribofilm: (a) Initial stage where running in was observed: the contact resistance is lower

than 1Ω when the substrate was not covered by a film leading to low contact resistance. In this period the tribochemical reaction and tribofilm formation were lower than material removal due to wear. (b) Tribochemical reactive stage where formation and wear compete: at the second stage the contact resistance reached between 1Ω and 100Ω where the surface was partially covered. The tribofilm starts to be formed completely and the film formation is competing with removal. (c) Growing stage where formation of the tribofilm dominates over wear: the contact resistance was higher than 100Ω . In this period, a fast increase in contact resistance was observed and rubbing surface was fully covered by the film. The tribofilm is mainly composed of oxides. The formation of the tribofilm would increase the contact resistance as illustrated in Figure 5.11. This was further proven by the reduction in friction due to introduction of Y_2O_3 . There was a tendency to achieve a kinetic balance between the tribofilm formation and wear. The value of contact resistance might be different for various lubricants, but the three stages could be universal any tribofilms that contain oxides.

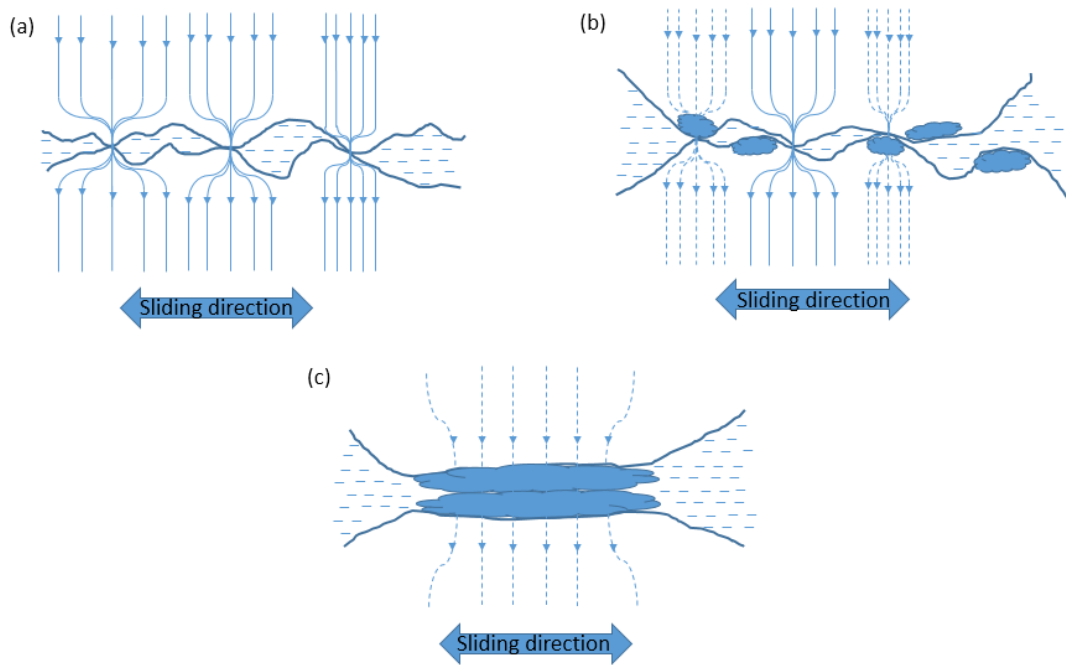


Figure 5.11 Illustration of three periods during the sliding process: (a) Running in stage: contact resistance $< 1 \Omega$ (b) Reactive stage: $1 \Omega < \text{contact resistance} < 100 \Omega$ (c) Growing stage: contact resistance $> 100 \Omega$.

5.5 Summary

In this chapter, a kinetic study of tribofilm formation and growth was conducted using an *in situ* approach via electrical contact resistance and illuminative nanoparticles during pin-on-disk experiments. Characterization using EDS and Raman spectroscopy identified the chemical composition of tribofilms. Some interesting new behavior were observed. In particular, the formation and growth of a tribofilm is more sensitive to frictional force than applied load. It means that to form a smooth and uniform tribofilm, controlling friction is recommended.

The correlation between friction and contact resistance has been established. In the case of NaYF_4 -containing tribofilm, there is a logarithmic relationship. The

tribochemical reaction rate was found exponential to the input mechanical power. The formation and growth of the tribofilm has three characteristics stages. Running in stage: where contact resistance $< 1 \Omega$. Reactive, i.e., competing stage: where $1 \Omega < \text{contact resistance} < 100 \Omega$. Finally, the growing stage, where contact resistance $> 100 \Omega$. The tribochemical reaction products contain oxides that were responsible for the increased electrical resistance.

This chapter presented a powerful tool to study the behavior of lubricant additive particles. Via measuring the electrical contact resistance during the sliding process, the formation of NaYF₄-containing tribofilm was monitored and the kinetic of film-growth was revealed. Due to its fluorescence properties, confocal scanning image of NaYF₄-containing wear track showed transportation and tribochemical reactions occurred on the substrate. The formation of Y₂O₃ during the sliding process leads to the superior performance of NaYF₄ with the reduction of wear as much as 82% compared to the base oil. Based on the understanding obtained in this study, it is highly possible to control the formation and growth of a kinetically balanced tribofilm through input mechanical power and design of additive chemistry. The discovery about the behavior of tribofilms is anticipated to be similar to many other material systems consisting oxides. Metal nanoparticles are prone to be oxidized. This would be a good material system for future study.

CHAPTER VI

MECHANISMS OF FLUID-DRAG REDUCTION VIA 3D-PRINTED SHARK SKINS

This chapter investigates the lubricating dynamics between nanoparticles and textured surfaces. A methodology was developed to evaluate morphological parameters and to enable studying in the effects of scale orientation on fluidic behavior of water. The scale orientation of a shark skin was defined as the angle between the ridges and the direction of fluid flow. Textured surfaces with a series orientation of scales were designed and fabricated using 3D printing of acrylonitrile butadiene styrene (ABS). The fluidic performance was evaluated using a rheometer. Results showed that the shark-skin-like surface with 90 degree orientation of scales exhibited the lowest viscosity drag. Its maximum viscosity reduction was 9%. A viscosity map was constructed based on fluid dynamic principals. It revealed that the drag reduction effect of a shark-skin-like surface was attributed to the low velocity gradient. This was further proven using diamond nitrogen-vacancy sensing where florescent diamond particles distributed evenly when the velocity gradient was at the lowest. The understanding could be used as guidance for future surface design.

6.1 Morphological characteristics

First of all, morphological characteristics of shark-skinned surfaces were analyzed based on the spacing and height of ridges. Three-dimensionally (3D) printed

shark-skinned surfaces were shown in Figure 6.1. Designed features were clearly printed. Other than the smooth surface, 3 shark-skinned surfaces with different shark skin scale orientation were designed considering the flowing direction of rheometer spindle. The performance of shark-skinned surface was closely related with the height (h) and spacing (s) of ridges. The height of ridge is uniform for all the shark-skinned surface, which is 0.4 mm. Spaces of ridges vary for the shark-skinned surface with different orientation of shark skin scale. For the parallel and mix ones, the space between ridges is 1 mm. For the perpendicular one, spaces between ridges are not uniform, ranging from 1~2 mm. Therefore, the average height versus spacing ratio (h/s) for parallel and mix surface is 0.67. The average h/s ratio for perpendicular surface is 0.27.

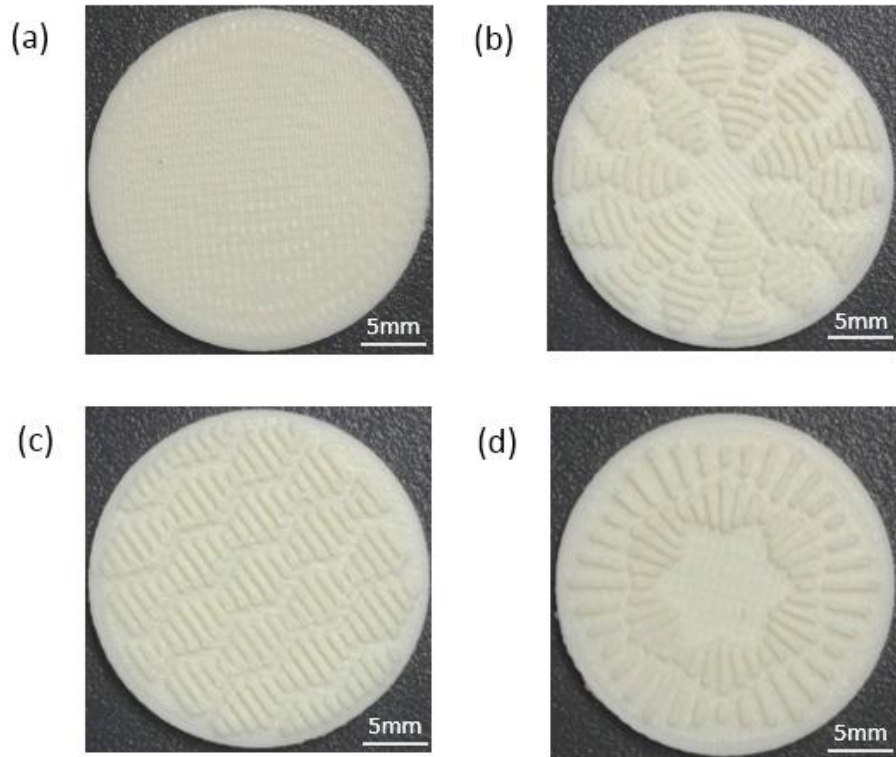


Figure 6.1 3D printed shark-skinned surfaces with different scale orientation: (a) smooth, (b) parallel (0 degree), (c) mix (45 degree), and (d) perpendicular (90 degree).

6.2 Fluidic performance

The next step we investigate the fluidic performance of shark-skinned surfaces to reveal the effect of scale orientation. Figure 6.2 shows the viscosity of water flowing over different shark-skinned surfaces under different shear rates. Generally speaking, water is Newtonian fluid, which indicates that its viscosity is constant under various shear rates. Due to the new set up of rheometer, however, centrifugal force will increase with the increase of shear rate, thereby leading to higher shear stress. Therefore, the viscosity of water will increase with the increase of shear rate. In Figure 6.2, when the

shear rate was lower than 300 s^{-1} , smooth surface showed lower viscosity than shark-skinned surfaces, which indicated the regime of laminar flow. The surface with parallel shark skin scale showed the highest viscosity. When the shear rate was higher than 300 s^{-1} , smooth surface showed a much higher viscosity than shark-skinned surfaces, which indicated the turbulent flow regime. The shark-skinned surface with perpendicular shark skin scale showed the lowest viscosity. In the regime of laminar flow, ridges of the shark-skinned surface block the movement of fluid, which leads to higher drag. Drag reduction effect of shark skin shark-skinned surface could only be found in the regime of turbulent flow. Drag of fluid increased dramatically due to the existence of the vortices. Formation of vortices is complicated and not fully understood. The higher contact area between the vortices and surface, the higher shear stress and fluid drag. In the case of shark-skinned surface, vortices usually exist on the top of the ridges, other than the valleys of ridges. Therefore, vortices only contact with the edge of ridges instead of the whole surface, leading to less fluid drag compared with the smooth surface. This mechanism has already been proved by the visualization of fluid flow[199].

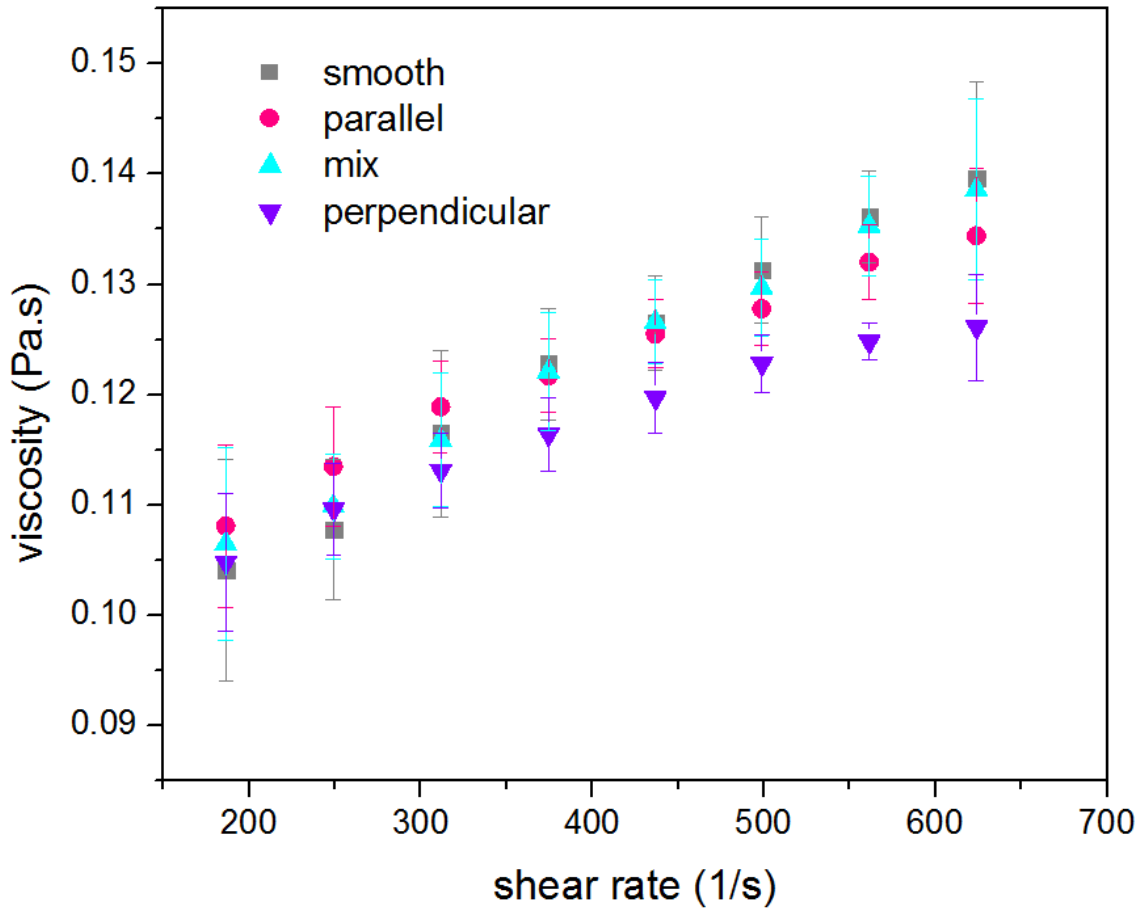


Figure 6.2 Viscosity of water flowing over different shark-skinned surfaces under different shear rate

6.3 The mechanism of drag reduction

To reveal the mechanism of drag reduction of shark-skinned surfaces, the distribution of diamond particles was studied using laser scanning microscope. After the viscosity test under the shear rate of 400 s^{-1} , the distribution of diamond particles on shark-skinned surfaces with different shark skin orientation were provided in Figure 6.3. The 3D distribution of particle (using ImageJ software) could be found in Figure 6.4. The peak intensity corresponds to the amount of diamond particles on the surface. From

the four images, we found the majority of diamond particles were located at the center of the surface. This is due to the rotational movement and centrifugal force of the spindle. Spindle center shows the lowest velocity while spindle edge shows the highest velocity. In this case, more diamond particles (higher peak intensity) indicated lower fluid velocity while less diamond particles (lower peak intensity) indicated higher fluid velocity. As a result, diamond particles distribution could be correlated with fluid velocity gradient on the shark-skinned surface.

In order to quantitatively analyze the uniformity of particle distribution, line scan was conducted across the center of the shark skin surfaces. Profiles could be found in Figure 6.5. The uniformity of particle distribution was calculated as the reciprocal of deviation of light intensity. Lower deviation of light intensity indicated higher uniformity of particle distribution and lower gradient of velocity. At least 4 different line scan of each sample were collected and results could be found in Figure 6.6. Perpendicular scale orientation showed the highest uniformity of particle distribution, which indicated the lowest gradient of velocity. The drag is, in fact, a measure of the energy required to transfer momentum between the fluid and the surface. Velocity gradient will create in the adjacent layers of fluid. The lower gradient of velocity will indicated less energy required for momentum transfer between adjacent layers of fluid, which leads to lower drag and viscosity of fluid. The distribution of diamond particle could explain the good reduction effect of viscosity of shark-skinned surfaces experimentally. It is a powerful tool to study the performance of other shark-skinned surfaces as well.

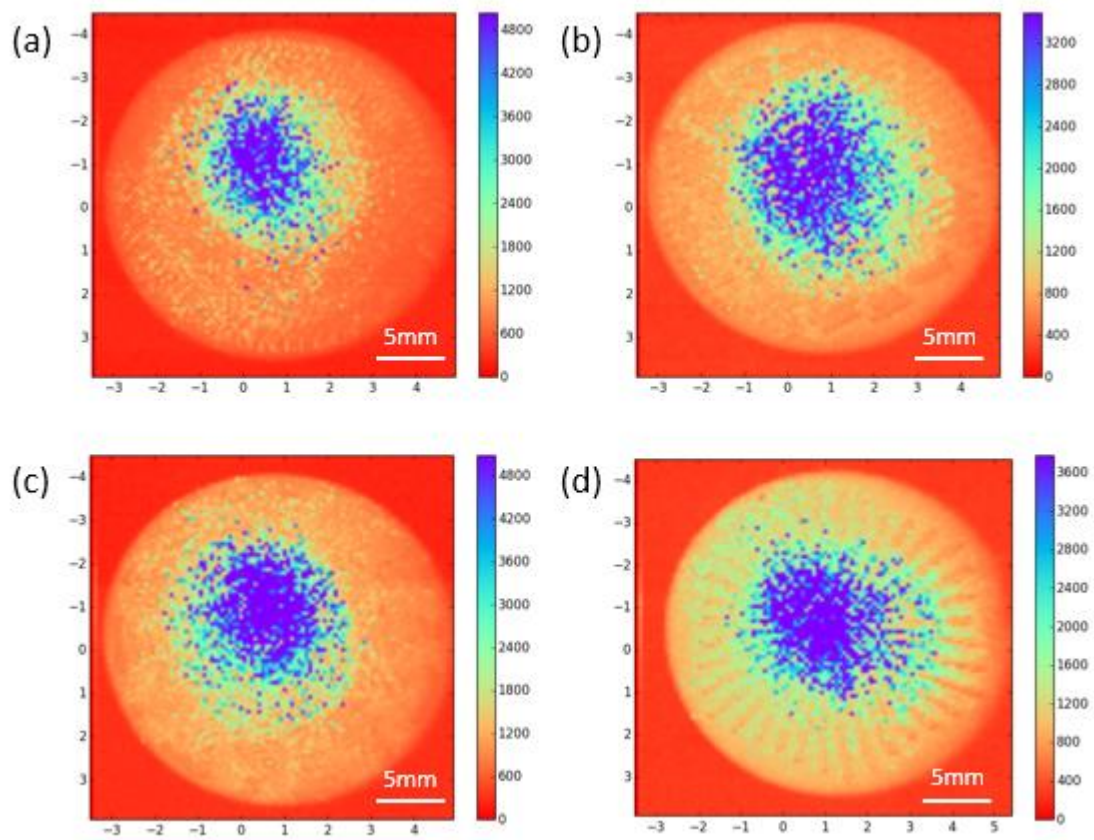


Figure 6.3 Diamond particle distribution on shark-skinned surface with different scale orientation after the viscosity test under 400 s^{-1} : (a) smooth, (b) parallel (0 degree), (c) mix (45 degree), and (d) perpendicular (90 degree).

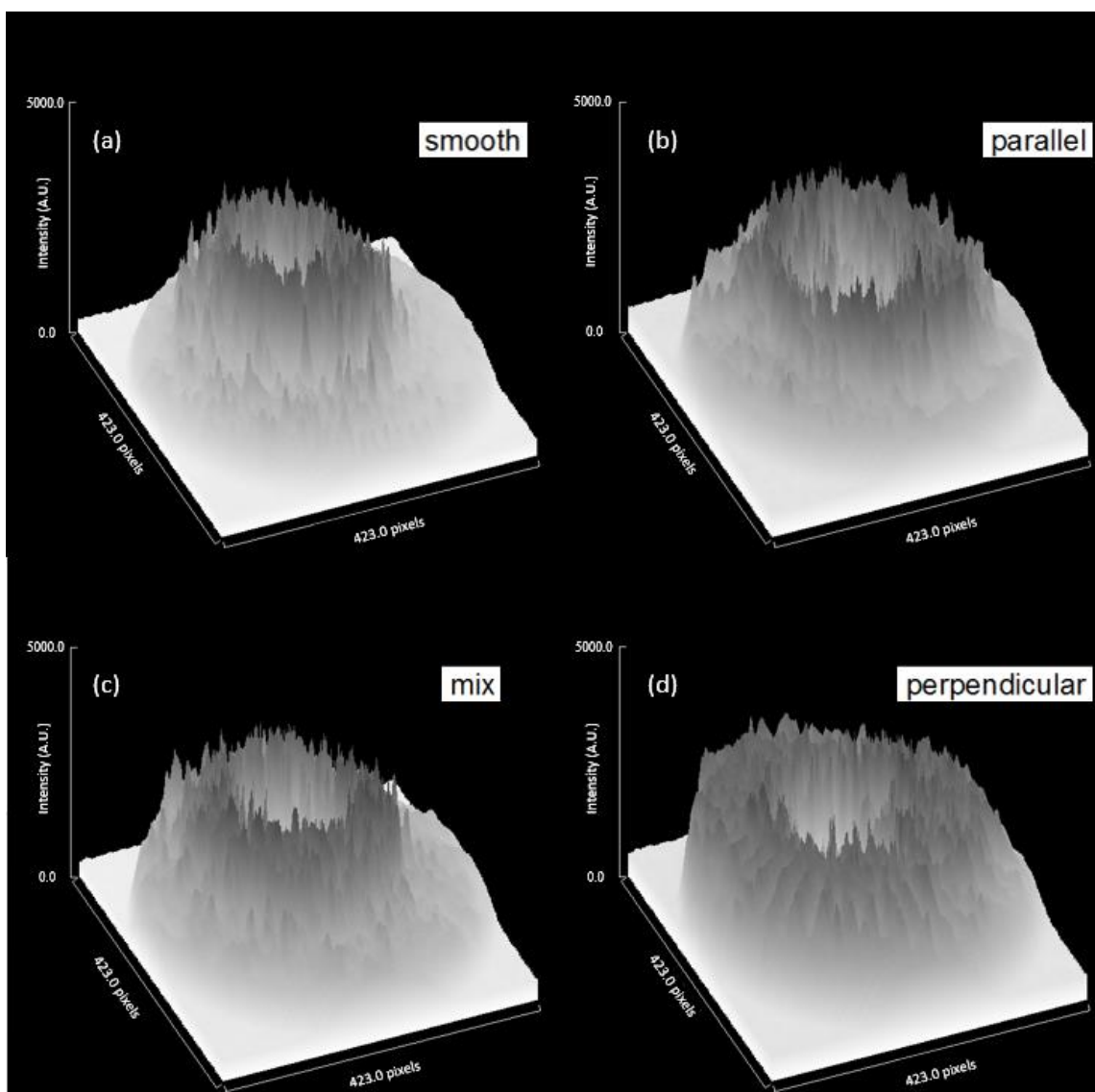


Figure 6.4 3D diamond particles distribution on textured surface with different shark skin orientation after the viscosity test under 400 s⁻¹: (a) smooth, (b) parallel (0 degree), (c) mix (45 degree), and (d) perpendicular (90 degree)

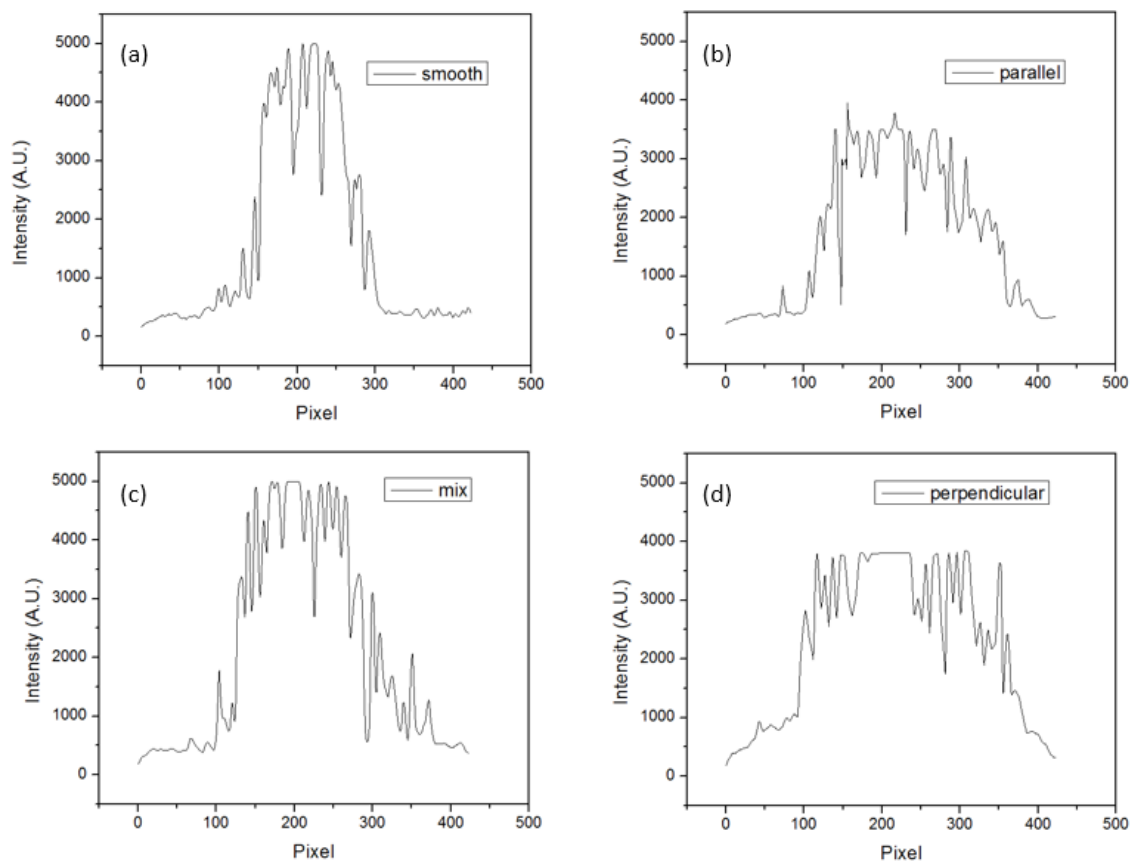


Figure 6.5 Line scan profile of diamond particle distribution on surfaces with different scale orientation after the viscosity test under 400 s^{-1} .

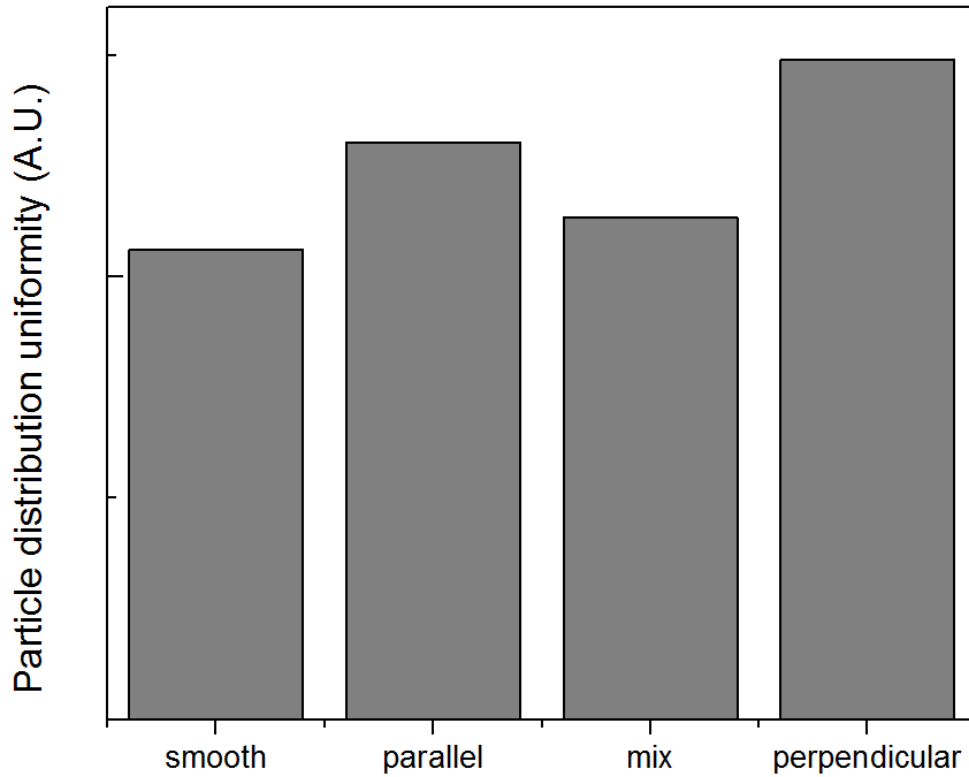


Figure 6.6 Diamond particle distribution uniformity comparison of textured surface with different shark skin orientation after the viscosity test under 400 s^{-1} : (a) smooth, (b) parallel (0 degree), (c) mix (45 degree), and (d) perpendicular (90 degree)

To study the fluidic performance of smooth surface, Reynolds number is examined against surface parameters. To differentiate the laminar flow regime and turbulent flow regime: $Re = \frac{uL}{\nu}$, where u , L and ν are fluid velocity, characteristic linear dimension and fluid kinematic viscosity, respectively. For the fluid flow over a flat plate, the transition Reynolds number is around 500,000. For fluid flow with lower Reynolds number, the flow is in the laminar regime. For that with the higher Reynolds number, it is in turbulent regime[200]. Likewise, in order to evaluate the drag reduction

performance of shark-skinned surface with different dimensions, the dimensionless parameter S^+ was introduced. It represents an effective Reynolds number considering ridges' spacing[201]: $S^+ = \frac{S}{v} \sqrt{\frac{\tau_w}{\rho}}$, where S , ρ , v and τ_w are the spacing between adjacent ridges, fluid density, fluid kinematic viscosity and average shear stress of the whole shark-skinned surface.

Eventually, in order to analyze the effect of viscosity reduction quantitatively, performances of shark-skinned surfaces compared with the smooth surface under various S^+ number were provided in Figure 6.7. X axis showed the S^+ number ranging from 0.3 to 0.9, and Y axis showed the ratio of shark-skinned surface viscosity to smooth surface viscosity. A ratio is higher or lower than 1, indicating the viscosity increase or decrease effect of shark-skinned surface respectively. All the three shark-skinned surfaces showed a similar trend. Viscosity reduction effect was getting more and more significant with the increase of S^+ number. In the case of parallel oriented shark-skinned surface, the S^+ transition number was 0.6. Mix orientated shark-skinned surface didn't show too much viscosity reduction effect, the S^+ transition number was around 0.55. For the case of perpendicular oriented shark-skinned surface, the S^+ transition number was 0.52.

Considering the orientation of shark skin ridges upon the fluid flow direction, we can label the parallel, mix and perpendicular pattern as 0 degree, 45 degree and 90 degree, respectively. Due to the orientation symmetry, 0 degree and 45 degree should have the same behavior with 180 degree and 135 degree, respectively. Eventually, the viscosity map of shark-skinned surface considering orientation and S^+ number could be concluded in Figure 6.8. In the red regime, viscosity of shark-skinned surface would increase

compared with smooth surface while it would decrease in the blue regime. Shark-skinned surface with 90 degree orientation showed the largest viscosity reduction. In this viscosity map, we could estimate the behavior of shark-skinned surface with different dimensions, scale orientation, and flow conditions. Moreover, a design of shark-skinned surface with better performance could be achieved using this map.

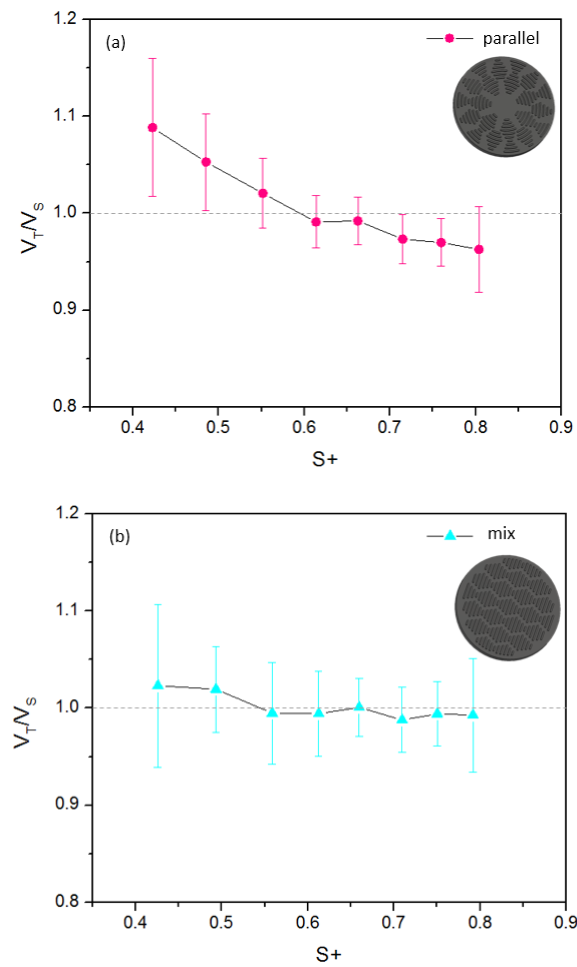


Figure 6.7 The viscosity reduction effect of shark-skinned surface compared with smooth surface under various S^+ number: (a) parallel, (b) mix and (c) perpendicular.

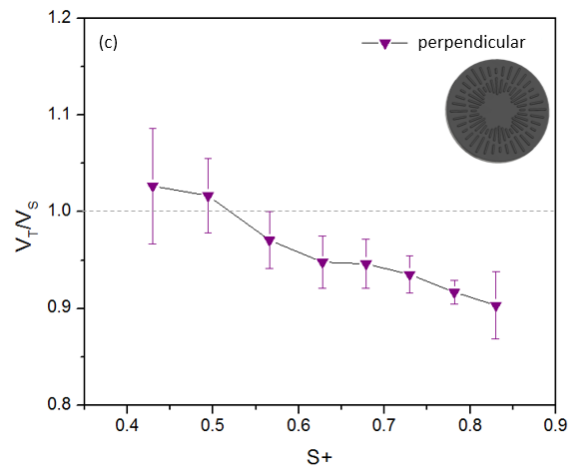


Figure 6.7 Continued

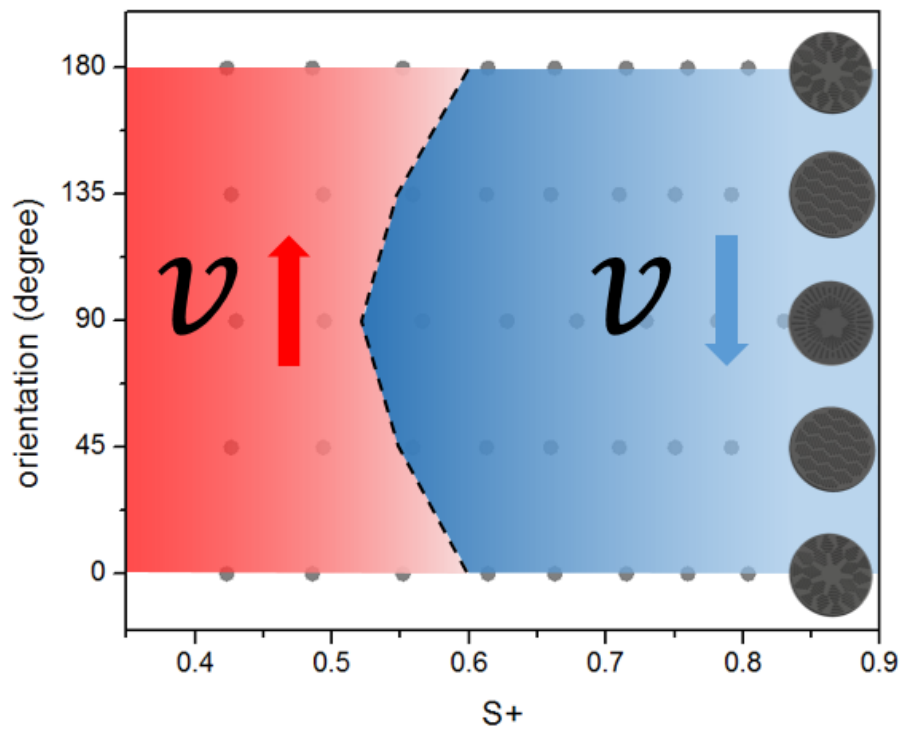


Figure 6.8 The viscosity map of shark-skinned surface with different shark skin orientation (from 0 degree to 180 degree)

6.4 Summary

In this chapter, the physical interaction between the nanoparticles and sharkskin like surface was investigated. Effects of scale orientation on the performance of shark-skin-like surfaces were studied. Compared with the smooth surface, the shark-skinned surface with 90 degree orientation of scales showed the lowest viscosity drag. The maximum viscosity reduction was 9%. This was further proven by the diamond nitrogen-vacancy sensing experiments. Diamond particles worked as tracking particles in fluid. Their distributions were found closely related with surface velocity gradients. The shark-skinned surface with 90 degree orientation scale showed a more uniform particles' distribution, which indicated to a lower velocity gradient. Less momentum transfer between adjacent fluid layers leads to a lower fluid drag. Eventually, a viscosity map of shark-skinned surface with different scale orientation was created. It will facilitate the design of shark-skinned surface with better performance. The understanding generated in this study could be used as guideline for future study in surface design and texturing.

CHAPTER VII

CONCLUSION AND RECOMMENDATION

7.1 Conclusion

This research investigated the tribological characteristics and roles of nanoparticles in lubrication. Tribological performance and rheological properties of nanoparticles were discussed in terms of friction, wear and viscosity. Moreover, chemical and physical interaction between the nanoparticles and lubricating system were interpreted in terms of kinetics and dynamics, respectively.

Tribological performance and rheological properties of α -ZrP and V_2O_5 were evaluated as additives in lubricants. In the case of α -ZrP, it showed 50% reduction in friction and 30% in wear compared to ZDDP. The promising performance was due to the tribofilm formation on the wear track, which composed of Fe_2O_3 , ZrO_2 and $Zr(PO_4)_2$. In the case of V_2O_5 , nanoparticles could reduce the viscosity, friction and wear of base oil for 5.9%, 33% and 44%, respectively. Through Raman spectrum and EDS analysis, it has been postulated that vanadium oxide nanoparticles interacted with steel surface forming intermetallic alloy V-Fe-Cr resulting in enhancement of wear protection.

Tribofilms play an important role in lubrication. A kinetic study of tribofilm formation and growth was conducted using an *in situ* approach via electrical contact resistance and illuminative nanoparticles during pin-on-disk experiments. The correlation between friction and contact resistance has been established. In the case of $NaYF_4$ -containing tribofilm, there is a logarithmic relationship. The tribochemical

reaction rate was found exponential to the input mechanical power. The formation and growth of the tribofilm has three characteristics stages. Running in stage: where contact resistance $< 1 \Omega$. Reactive, i.e., competing stage: where $1 \Omega < \text{contact resistance} < 100 \Omega$. Finally, the growing stage, where contact resistance $> 100 \Omega$. The tribochemical reaction products contain oxides that were responsible for the increased electrical resistance. Based on the understanding obtained in this study, it is highly possible to control the formation and growth of a kinetically balanced tribofilm through input mechanical power and design of additive chemistry. The discovery about the behavior of tribofilms is anticipated to be similar to many other material systems consisting oxides. Metal nanoparticles are prone to be oxidized. This would be a good material system for future study.

For the lubricating dynamics, the physical interaction between the nanoparticles and lubricating systems were investigated. Effects of scale orientation on the performance of shark-skin-like surfaces were studied. Compared with the smooth surface, the shark-skinned surface with 90 degree orientation of scales showed the lowest drag. The maximum reduction of viscosity was 9%. This was further proven by the diamond nitrogen-vacancy sensing experiments. Diamond particles worked as tracking particles in fluid. Their distributions were found closely related with surface velocity gradients. The shark-skinned surface with 90 degree orientation scale showed a more uniform distribution of diamond particles, which indicated to a lower gradient of velocity. Less momentum transfer between adjacent layers of fluid leads to a lower drag. Eventually, a viscosity map of shark-skinned surface with different scale orientation was

created. It will facilitate the design of shark-skinned surface with better performance. The understanding generated in this study could be used as guideline for future study in surface design and texturing.

To summarize, there are three key achievements in this research.

- 1) As additives in lubricants, nanoparticles exhibited promising performance in terms of tribology and rheology. For example, α -ZrP nanoparticles exhibited 50% reduction in friction and 30% in wear compared to conventional toxic additive ZDDP. The V_2O_5 nanoparticles could reduce the viscosity, friction and wear of base oil for 5.9%, 33% and 44%, respectively.
- 2) A universal method using electrical contact for *in situ* monitoring of the formation of tribofilms was developed and the mechanisms of tribofilm growth was revealed. It was discovered that the growth of a tribofilm was triggered by the input mechanical power. The growth involves three stages, running-in, reactive, and growth.
- 3) A novel approach to track nanoparticles particles was developed. Using this method, mechanisms of drag reduction of sharkskin like surface was studied. The distribution of particles on textured surface was found closely related with surface velocity gradients. The shark-skinned surface with 90 degree orientation scale showed a more uniform distribution of diamond particles, which indicated to a lower gradient of velocity. Less momentum transfer between adjacent layers of fluid leads to a lower drag. It will enable the novel design of textured surface.

7.2 Future Recommendation

Based on the discoveries of this work, recommended future study are:

- 1) Effects of various working environments: most experiments of this research are conducted under the room temperature. In industry, lubricants are applied under a wide temperature range. For example, vehicle engine lubricants are employed under 200 ~ 300 °C. Moreover, lubricants in this research are tested in oil. The water based lubricants should be developed as well, which could be applied on machinery. Therefore, it is necessary to evaluate the nanoparticles in various working environments.
- 2) Tribofilm models of other lubricants: in this research, the tribofilm model of nanoparticles has been developed. Likewise, tribofilms models of other lubricants, including ionic liquids and organic compounds, could be built via contact resistance measurement. Moreover, this characterization method could be extended to other interfacial kinetic study.
- 3) Design and evaluation of textured surface: based on the viscosity map, sharkskin like surface with lower drag could be designed. The evaluation method should be further improved to mimic the real working environment, such as evaluating the performance under the linear motion and sea water condition.

REFERENCES

- [1] Stachowiak G, Batchelor AW. Engineering Tribology: Butterworth-Heinemann; 2013.
- [2] Bohner GE, Krimmel JA, Schmidt-Collérus JJ. Properties of Polyester Fluids with Desirable Synthetic Lubricant Characteristics. *Journal of Chemical and Engineering Data*. 7:547-53 (1962).
- [3] Niedzielski EL. Neopentyl Polyol Ester Lubricants-Bulk Property Optimization. *Industrial & Engineering Chemistry Product Research and Development*. 15:54-8 (1976).
- [4] Cohen G, Murphy C, O'rear J, Ravner H, Zisman W. Aliphatic Esters-Properties and Lubricant Applications. *Industrial & Engineering Chemistry*. 45:1766-75 (1953).
- [5] Rudnick LR. Lubricant Additives: Chemistry and Applications: CRC press; 2009.
- [6] Ahmed NS, Nassar AM. Lubricating Oil Additives: InTech; 2011.
- [7] Khalkar S, Bhowmick D, Pratap A. Synthesis and Effect of Fatty Acid Amides as Friction Modifiers in Petroleum Base Stock. *Journal of Oleo Science*. 62:901-4 (2013).
- [8] Zhang J, Yang S, Liu W, Xue Q. The Mechanisms of Boundary Lubrication and Antioxidation of Bromobenzo-15-Crown-5 as Novel Additive. *Wear*. 236:303-7 (1999).
- [9] Saccomando DJ, Vickerman RJ, Bartley SL, Kocsis JA. Aromatic Imides and Esters as Lubricant Additives. Google Patents. p. 2012.

- [10] He Z, Song Y, Shao H, Zhan W, Ren T. A Study of the Synergistic Effect of a Triazine-Dithiocarbamate Derivative with Tcp in Vegetable Oil. *Lubrication Science*. 21:287-97 (2005).
- [11] Tonck A, Martin JM, Kapsa P, Georges JM. Boundary Lubrication with Anti-Wear Additives: Study of Interface Film Formation by Electrical Contact Resistance. *Tribol Int*. 12:209-13 (1979).
- [12] Spikes H. Low- and Zero-Sulphated Ash, Phosphorus and Sulphur Anti-Wear Additives for Engine Oils. *Lubr Sci*. 20:103-36 (2008).
- [13] Qian Z, Minnikanti VS, Archer LA. Surface Segregation of Highly Branched Polymer Additives in Linear Hosts. *J Polym Sci Part B Polym Phys*. 46:1788-801 (2008).
- [14] Leonov AI, Prokunin AN. Nonlinear Phenomena in Flows of Viscoelastic Polymer Fluids: Chapman and Hall; 1994.
- [15] Kajdas C. Additives for Metalworking Lubricants-a Review. *Lubr Sci*. 1:345-409 (1989).
- [16] Ratoi M, Spikes HA. Lubricating Properties of Aqueous Surfactant Solutions. *Tribol Trans*. 42:479-86 (1999).
- [17] Hamblin PC, Kristen U, Chasan D. Ashless Antioxidants, Copper Deactivators and Corrosion Inhibitors: Their Use in Lubricating Oils. *Lubr Sci*. 2:287-318 (1990).
- [18] Kang J, Fu R-D, Luan G-H, Dong C-L, He M. In-Situ Investigation on the Pitting Corrosion Behavior of Friction Stir Welded Joint of Aa2024-T3 Aluminium Alloy. *Corros Sci*. 52:620-6 (2010).

- [19] Sharma BK, Doll KM, Erhan SZ. Ester Hydroxy Derivatives of Methyl Oleate: Tribological, Oxidation and Low Temperature Properties. *Bioresource technology*. 99:7333-40 (2008).
- [20] Minami I, Kubo T, Nanao H, Mori S, Sagawa T, Okuda S. Investigation of Tribo-Chemistry by Means of Stable Isotopic Tracers, Part 2: Lubrication Mechanism of Friction Modifiers on Diamond-Like Carbon. *Tribology Transactions*. 50:477-87 (2007).
- [21] Müller M, Topolovec-Miklozic K, Dardin A, Spikes HA. The Design of Boundary Film-Forming Pma Viscosity Modifiers. *Tribology Transactions*. 49:225-32 (2006).
- [22] Stambaugh R, Kinker B. Viscosity Index Improvers and Thickeners. Chemistry and Technology of Lubricants: Springer; 2010. p. 153-87.
- [23] Khodaei-Tehrani M, Niazi A. Quantum Chemical Studies on the Corrosion Inhibition of Some Hector Bases on Mild Steel in Acidic Medium. *Oriental Journal of Chemistry*. 31:423-9 (2015).
- [24] Johnson MD, Korcek S, Zinbo M. Inhibition of Oxidation by Zdtp and Ashless Antioxidants in the Presence of Hydroperoxides at 160° C-Part I. SAE Technical Paper. p. 1983.
- [25] Ingold K. Inhibition of the Autoxidation of Organic Substances in the Liquid Phase. *Chemical Reviews*. 61:563-89 (1961).
- [26] El Naga HA, Salem A. Effect of Worn Metals on the Oxidation of Lubricating Oils. *Wear*. 96:267-83 (1984).
- [27] Kreuz K. Diesel Engine Chemistry-as Applied to Lubricant Problems. *Lubrication*. 56:77-& (1970).

- [28] Kreuz K. Gasoline Engine Chemistry-as Applied to Lubricant Problems. *Lubrication*. 55:53-& (1969).
- [29] Nelson KD, Plavac F. Sulfurized Polyisobutylene Based Wear and Oxidation Inhibitors. Google Patents. p. 2005.
- [30] Fouda A, Mohamed A. Substituted Phenols as Corrosion Inhibitors for Copper in Nitric Acid. *Materials and Corrosion*. 39:23-6 (1988).
- [31] Schilling A. Motor Oils and Engine Lubrication: Scientific Publications; 1972.
- [32] Hessell ET, Abramshe RA, Gallacher LV. Compositions of Group Ii and/or Group Iii Base Oils and Alkylated Fused and/or Polyfused Aromatic Compounds. Google Patents. p. 2009.
- [33] Kasper FK, Tanahashi K, Fisher JP, Mikos AG. Synthesis of Poly (Propylene Fumarate). *Nature Protocols*. 4:518-25 (2009).
- [34] Tang Z, Li S. A Review of Recent Developments of Friction Modifiers for Liquid Lubricants (2007–Present). *Current Opinion in Solid State and Materials Science*. 18:119-39 (2014).
- [35] Rapoport L, Leshchinsky V, Lvovsky M, Nepomnyashchy O, Volovik Y, Tenne R. Mechanism of Friction of Fullerenes. *Industrial lubrication and tribology*. 54:171-6 (2002).
- [36] Wu Y, Tsui W, Liu T. Experimental Analysis of Tribological Properties of Lubricating Oils with Nanoparticle Additives. *Wear*. 262:819-25 (2007).
- [37] Chiñas-Castillo F, Spikes H. Mechanism of Action of Colloidal Solid Dispersions. *Journal of Tribology*. 125:552-7 (2003).

- [38] Hu ZS, Lai R, Lou F, Wang L, Chen Z, Chen G, et al. Preparation and Tribological Properties of Nanometer Magnesium Borate as Lubricating Oil Additive. *Wear*. 252:370-4 (2002).
- [39] Xiaodong Z, Xun F, Huaqiang S, Zhengshui H. Lubricating Properties of Cyanex 302-Modified MoS₂ Microspheres in Base Oil 500sn. *Lubrication Science*. 19:71-9 (2007).
- [40] Ginzburg B, Shibaev L, Kireenko O, Shepelevskii A, Baidakova M, Sitnikova A. Antiwear Effect of Fullerene C 6 0 Additives to Lubricating Oils. *Russian Journal of Applied Chemistry*. 75:1330-5 (2002).
- [41] Zhou J, Yang J, Zhang Z, Liu W, Xue Q. Study on the Structure and Tribological Properties of Surface-Modified Cu Nanoparticles. *Materials Research Bulletin*. 34:1361-7 (1999).
- [42] Rastogi R, Yadav M, Bhattacharya A. Application of Molybdenum Complexes of 1-Aryl-2, 5-Dithiohydrazodicarbonamides as Extreme Pressure Lubricant Additives. *Wear*. 252:686-92 (2002).
- [43] Liu G, Li X, Qin B, Xing D, Guo Y, Fan R. Investigation of the Mending Effect and Mechanism of Copper Nano-Particles on a Tribologically Stressed Surface. *Tribology Letters*. 17:961-6 (2004).
- [44] Tao X, Jiazheng Z, Kang X. The Ball-Bearing Effect of Diamond Nanoparticles as an Oil Additive. *Journal of Physics D: Applied Physics*. 29:2932 (1996).

- [45] Fangsuwannarak K, Triratanasirichai K. Effect of Metalloid Compound and Bio-Solution Additives on Biodiesel Engine Performance and Exhaust Emissions. *American Journal of Applied Sciences*. 10:1201 (2013).
- [46] Khond VW, Kriplani V. Effect of Nanofluid Additives on Performances and Emissions of Emulsified Diesel and Biodiesel Fueled Stationary Ci Engine: A Comprehensive Review. *Renewable and Sustainable Energy Reviews*. 59:1338-48 (2016).
- [47] Sajeevan AC, Sajith V. Diesel Engine Emission Reduction Using Catalytic Nanoparticles: An Experimental Investigation. *Journal of Engineering*. 2013 (2013).
- [48] Sajith V, Sobhan C, Peterson G. Experimental Investigations on the Effects of Cerium Oxide Nanoparticle Fuel Additives on Biodiesel. *Advances in Mechanical Engineering*. 2:581407 (2010).
- [49] Abdel-Hadi EA-H, Taher SH, Torki AHM, Hamad SS. Heat Transfer Analysis of Vapor Compression System Using Nano CuO-R134a. *International Conference on Advanced Materials Engineering: IPCSIT*; 80-4. p. 2011.
- [50] Wang X, Xu X, S. Choi SU. Thermal Conductivity of Nanoparticle-Fluid Mixture. *Journal of Thermophysics and Heat Transfer*. 13:474-80 (1999).
- [51] Bartelt K, Park Y, Liu L, Jacobi A. Flow-Boiling of R-134a/Poe/Cuo Nanofluids in a Horizontal Tube. (2008).
- [52] Bi S, Guo K, Liu Z, Wu J. Performance of a Domestic Refrigerator Using Tio 2-R600a Nano-Refrigerant as Working Fluid. *Energy Conversion and Management*. 52:733-7 (2011).

- [53] Zhang W, Demydov D, Jahan MP, Mistry K, Erdemir A, Malshe AP. Fundamental Understanding of the Tribological and Thermal Behavior of Ag–MoS₂ Nanoparticle-Based Multi-Component Lubricating System. *Wear*. 288:9-16 (2012).
- [54] Ma J, Mo Y, Bai M. Effect of Ag Nanoparticles Additive on the Tribological Behavior of Multialkylated Cyclopentanes (Macs). *Wear*. 266:627-31 (2009).
- [55] Ghaednia H, Babaei H, Jackson RL, Bozack MJ, Khodadadi J. The Effect of Nanoparticles on Thin Film Elasto-Hydrodynamic Lubrication. *Applied Physics Letters*. 103:263111 (2013).
- [56] Luo T, Wei X, Huang X, Huang L, Yang F. Tribological Properties of Al₂O₃ Nanoparticles as Lubricating Oil Additives. *Ceramics International*. 40:7143-9 (2014).
- [57] Kedzierski MA. Effect of Concentration on R134a/Al₂O₃ Nanolubricant Mixture Boiling on a Reentrant Cavity Surface. *International Journal of Refrigeration*. 49:36-48 (2015).
- [58] Peña-Parás L, Taha-Tijerina J, Garza L, Maldonado-Cortés D, Michalczewski R, Lapray C. Effect of CuO and Al₂O₃ Nanoparticle Additives on the Tribological Behavior of Fully Formulated Oils. *Wear*. 332-333:1256-61 (2015).
- [59] Jiao D, Zheng S, Wang Y, Guan R, Cao B. The Tribology Properties of Alumina/Silica Composite Nanoparticles as Lubricant Additives. *Applied Surface Science*. 257:5720-5 (2011).
- [60] Luo T, Wei X, Zhao H, Cai G, Zheng X. Tribology Properties of Al₂O₃/TiO₂ Nanocomposites as Lubricant Additives. *Ceramics International*. 40:10103-9 (2014).

- [61] Flores-Castañeda M, Camps E, Camacho-López M, Muhl S, García E, Figueroa M. Bismuth Nanoparticles Synthesized by Laser Ablation in Lubricant Oils for Tribological Tests. *Journal of Alloys and Compounds*. 643:S67-S70 (2015).
- [62] Manning T, Field R, Klingaman K, Fair M, Bolognini J, Crownover R, et al. Innovative Boron Nitride-Doped Propellants. *Defence Technology*. (2015).
- [63] Xu N, Zhang M, Li W, Zhao G, Wang X, Liu W. Study on the Selectivity of Calcium Carbonate Nanoparticles under the Boundary Lubrication Condition. *Wear*. 307:35-43 (2013).
- [64] Shen T, Wang D, Yun J, Liu Q, Liu X, Peng Z. Tribological Properties and Tribochemical Analysis of Nano-Cerium Oxide and Sulfurized Isobutene in Titanium Complex Grease. *Tribology International*. 93:332-46 (2016).
- [65] Yang G, Zhang Z, Zhang S, Yu L, Zhang P. Synthesis and Characterization of Highly Stable Dispersions of Copper Nanoparticles by a Novel One-Pot Method. *Materials Research Bulletin*. 48:1716-9 (2013).
- [66] Hu H, Peng H, Ding G. Nucleate Pool Boiling Heat Transfer Characteristics of Refrigerant/Nanolubricant Mixture with Surfactant. *International Journal of Refrigeration*. 36:1045-55 (2013).
- [67] Pan Q, Zhang X. Synthesis and Tribological Behavior of Oil-Soluble Cu Nanoparticles as Additive in Sf15w/40 Lubricating Oil. *Rare Metal Materials and Engineering*. 39:1711-4 (2010).

- [68] Yu H-l, Xu Y, Shi P-j, Xu B-s, Wang X-l, Liu Q. Tribological Properties and Lubricating Mechanisms of Cu Nanoparticles in Lubricant. *Transactions of Nonferrous Metals Society of China*. 18:636-41 (2008).
- [69] Wang XL, Yin YL, Zhang GN, Wang WY, Zhao KK. Study on Antiwear and Repairing Performances About Mass of Nano-Copper Lubricating Additives to 45 Steel. *Physics Procedia*. 50:466-72 (2013).
- [70] Zhang B-S, Xu B-S, Xu Y, Gao F, Shi P-J, Wu Y-X. Cu Nanoparticles Effect on the Tribological Properties of Hydrosilicate Powders as Lubricant Additive for Steel–Steel Contacts. *Tribology International*. 44:878-86 (2011).
- [71] Zhang C, Zhang S, Yu L, Zhang Z, Wu Z, Zhang P. Preparation and Tribological Properties of Water-Soluble Copper/Silica Nanocomposite as a Water-Based Lubricant Additive. *Applied Surface Science*. 259:824-30 (2012).
- [72] Kedzierski MA, Gong M. Effect of Cuo Nanolubricant on R134a Pool Boiling Heat Transfer. *International Journal of Refrigeration*. 32:791-9 (2009).
- [73] Shenoy BS, Binu KG, Pai R, Rao DS, Pai RS. Effect of Nanoparticles Additives on the Performance of an Externally Adjustable Fluid Film Bearing. *Tribology International*. 45:38-42 (2012).
- [74] Kang X, Wang B, Zhu L, Zhu H. Synthesis and Tribological Property Study of Oleic Acid-Modified Copper Sulfide Nanoparticles. *Wear*. 265:150-4 (2008).
- [75] Peng DX, Kang Y, Hwang RM, Shyr SS, Chang YP. Tribological Properties of Diamond and SiO₂ Nanoparticles Added in Paraffin. *Tribology International*. 42:911-7 (2009).

- [76] Elomaa O, Hakala TJ, Myllymäki V, Oksanen J, Ronkainen H, Singh VK, et al. Diamond Nanoparticles in Ethylene Glycol Lubrication on Steel–Steel High Load Contact. *Diamond and Related Materials*. 34:89-94 (2013).
- [77] Padgurskas J, Rukuiza R, Prosyčėvas I, Kreivaitis R. Tribological Properties of Lubricant Additives of Fe, Cu and Co Nanoparticles. *Tribology International*. 60:224-32 (2013).
- [78] Zhou G, Zhu Y, Wang X, Xia M, Zhang Y, Ding H. Sliding Tribological Properties of 0.45% Carbon Steel Lubricated with Fe₃O₄ Magnetic Nano-Particle Additives in Baseoil. *Wear*. 301:753-7 (2013).
- [79] Rabaso P, Ville F, Dassenoy F, Diaby M, Afanasiev P, Cavoret J, et al. Boundary Lubrication: Influence of the Size and Structure of Inorganic Fullerene-Like MoS₂ Nanoparticles on Friction and Wear Reduction. *Wear*. 320:161-78 (2014).
- [80] Zhao J, He Y, Wang Y, Wang W, Yan L, Luo J. An Investigation on the Tribological Properties of Multilayer Graphene and MoS₂ Nanosheets as Additives Used in Hydraulic Applications. *Tribology International*. 97:14-20 (2016).
- [81] Greco A, Mistry K, Sista V, Eryilmaz O, Erdemir A. Friction and Wear Behaviour of Boron Based Surface Treatment and Nano-Particle Lubricant Additives for Wind Turbine Gearbox Applications. *Wear*. 271:1754-60 (2011).
- [82] Li S, Qin H, Zuo R, Bai Z. Tribological Performance of Mg/Al/Ce Layered Double Hydroxides Nanoparticles and Intercalated Products as Lubricant Additives. *Applied Surface Science*. 353:643-50 (2015).

- [83] Lahouij I, Vacher B, Martin J-M, Dassenoy F. If- MoS₂ Based Lubricants: Influence of Size, Shape and Crystal Structure. *Wear*. 296:558-67 (2012).
- [84] Tenne R. Fullerene-Like Materials and Nanotubes from Inorganic Compounds with a Layered (2-D) Structure. *Colloids and Surfaces A: Physicochemical and Engineering Aspects*. 208:83-92 (2002).
- [85] Rapoport L, Feldman Y, Homyonfer M, Cohen H, Sloan J, Hutchison J, et al. Inorganic Fullerene-Like Material as Additives to Lubricants: Structure–Function Relationship. *Wear*. 225:975-82 (1999).
- [86] Li S, Qin H, Zuo R, Bai Z. Friction Properties of La-Doped Mg/Al Layered Double Hydroxide and Intercalated Product as Lubricant Additives. *Tribology International*. 91:60-6 (2015).
- [87] Hou X, He J, Yu L, Li Z, Zhang Z, Zhang P. Preparation and Tribological Properties of Fluorosilane Surface-Modified Lanthanum Trifluoride Nanoparticles as Additive of Fluoro Silicone Oil. *Applied Surface Science*. 316:515-23 (2014).
- [88] Xu Y, Hu E, Hu K, Xu Y, Hu X. Formation of an Adsorption Film of MoS₂ Nanoparticles and Dioctyl Sebacate on a Steel Surface for Alleviating Friction and Wear. *Tribology International*. 92:172-83 (2015).
- [89] Kalin M, Kogovšek J, Remškar M. Nanoparticles as Novel Lubricating Additives in a Green, Physically Based Lubrication Technology for Dlc Coatings. *Wear*. 303:480-5 (2013).

- [90] Kalin M, Kogovšek J, Remškar M. Mechanisms and Improvements in the Friction and Wear Behavior Using MoS₂ Nanotubes as Potential Oil Additives. *Wear*. 280-281:36-45 (2012).
- [91] Zhang ZJ, Zhang J, Xue QJ. Synthesis and Characterization of a Molybdenum Disulfide Nanocluster. *The Journal of Physical Chemistry*. 98:12973-7 (1994).
- [92] Santillo G, Deorsola FA, Bensaid S, Russo N, Fino D. Mos₂ Nanoparticle Precipitation in Turbulent Micromixers. *Chemical Engineering Journal*. 207-208:322-8 (2012).
- [93] Xie H, Jiang B, He J, Xia X, Pan F. Lubrication Performance of MoS₂ and SiO₂ Nanoparticles as Lubricant Additives in Magnesium Alloy-Steel Contacts. *Tribology International*. 93:63-70 (2016).
- [94] Nunn N, Mahbooba Z, Ivanov MG, Ivanov DM, Brenner DW, Shenderova O. Tribological Properties of Polyalphaolefin Oil Modified with Nanocarbon Additives. *Diamond and Related Materials*. 54:97-102 (2015).
- [95] Meng Y, Su F, Chen Y. Synthesis of Nano-Cu/Graphene Oxide Composites by Supercritical Co₂-Assisted Deposition as a Novel Material for Reducing Friction and Wear. *Chemical Engineering Journal*. 281:11-9 (2015).
- [96] Dubey MK, Bijwe J, Ramakumar SSV. Nano-Ptfe: New Entrant as a Very Promising Ep Additive. *Tribology International*. 87:121-31 (2015).
- [97] Chou R, Battez AH, Cabello JJ, Viesca JL, Osorio A, Sagastume A. Tribological Behavior of Polyalphaolefin with the Addition of Nickel Nanoparticles. *Tribology International*. 43:2327-32 (2010).

- [98] Ye P, Jiang X, Li S, Li S. Preparation of NiMoS₂ Nanoparticle and Investigation of Its Tribological Behavior as Additive in Lubricating Oils. *Wear*. 253:572-5 (2002).
- [99] Chen Y, Zhang Y, Zhang S, Yu L, Zhang P, Zhang Z. Preparation of Nickel-Based Nanolubricants Via a Facile in Situ One-Step Route and Investigation of Their Tribological Properties. *Tribology Letters*. 51:73-83 (2013).
- [100] Gu K, Chen B, Chen Y. Preparation and Tribological Properties of Lanthanum-Doped TiO₂ Nanoparticles in Rapeseed Oil. *Journal of Rare Earths*. 31:589-94 (2013).
- [101] Abad MD, Sánchez-López JC. Tribological Properties of Surface-Modified Pd Nanoparticles for Electrical Contacts. *Wear*. 297:943-51 (2013).
- [102] Sánchez-López JC, Abad MD, Kolodziejczyk L, Guerrero E, Fernández A. Surface-Modified Pd and Au Nanoparticles for Anti-Wear Applications. *Tribology International*. 44:720-6 (2011).
- [103] Rico EF, Minondo I, Cuervo DG. Rolling Contact Fatigue Life of Aisi 52100 Steel Balls with Mineral and Synthetic Polyester Lubricants with Ptfе Nanoparticle Powder as an Additive. *Wear*. 266:671-7 (2009).
- [104] Rico EF, Minondo I, Cuervo DG. The Effectiveness of Ptfе Nanoparticle Powder as an Ep Additive to Mineral Base Oils. *Wear*. 262:1399-406 (2007).
- [105] Yadgarov L, Petrone V, Rosentsveig R, Feldman Y, Tenne R, Senatore A. Tribological Studies of Rhenium Doped Fullerene-Like MoS₂ Nanoparticles in Boundary, Mixed and Elasto-Hydrodynamic Lubrication Conditions. *Wear*. 297:1103-10 (2013).

- [106] Boshui C, Kecheng G, Jianhua F, Jiang W, Jiu W, Nan Z. Tribological Characteristics of Monodispersed Cerium Borate Nanospheres in Biodegradable Rapeseed Oil Lubricant. *Applied Surface Science*. 353:326-32 (2015).
- [107] Yu HL, Xu Y, Shi PJ, Wang HM, Zhao Y, Xu BS, et al. Tribological Behaviors of Surface-Coated Serpentine Ultrafine Powders as Lubricant Additive. *Tribology International*. 43:667-75 (2010).
- [108] Zhao F, Bai Z, Fu Y, Zhao D, Yan C. Tribological Properties of Serpentine, $\text{La}(\text{OH})_3$ and Their Composite Particles as Lubricant Additives. *Wear*. 288:72-7 (2012).
- [109] Bobbo S, Fedele L, Fabrizio M, Barison S, Battiston S, Pagura C. Influence of Nanoparticles Dispersion in Poe Oils on Lubricity and R134a Solubility. *International Journal of Refrigeration*. 33:1180-6 (2010).
- [110] Li X, Cao Z, Zhang Z, Dang H. Surface-Modification in Situ of Nano- SiO_2 and Its Structure and Tribological Properties. *Applied Surface Science*. 252:7856-61 (2006).
- [111] Zhang S, Hu L, Feng D, Wang H. Anti-Wear and Friction-Reduction Mechanism of Sn and Fe Nanoparticles as Additives of Multialkylated Cyclopentanes under Vacuum Condition. *Vacuum*. 87:75-80 (2013).
- [112] Li Z, Hou X, Yu L, Zhang Z, Zhang P. Preparation of Lanthanum Trifluoride Nanoparticles Surface-Capped by Tributyl Phosphate and Evaluation of Their Tribological Properties as Lubricant Additive in Liquid Paraffin. *Applied Surface Science*. 292:971-7 (2014).
- [113] Krishna Sabareesh R, Gobinath N, Sajith V, Das S, Sobhan CB. Application of TiO_2 Nanoparticles as a Lubricant-Additive for Vapor Compression Refrigeration

- Systems – an Experimental Investigation. *International Journal of Refrigeration*. 35:1989-96 (2012).
- [114] Binu KG, Shenoy BS, Rao DS, Pai R. A Variable Viscosity Approach for the Evaluation of Load Carrying Capacity of Oil Lubricated Journal Bearing with TiO₂ Nanoparticles as Lubricant Additives. *Procedia Materials Science*. 6:1051-67 (2014).
- [115] Ye W, Cheng T, Ye Q, Guo X, Zhang Z, Dang H. Preparation and Tribological Properties of Tetrafluorobenzoic Acid-Modified TiO₂ Nanoparticles as Lubricant Additives. *Materials Science and Engineering: A*. 359:82-5 (2003).
- [116] Zulkifli NWM, Kalam MA, Masjuki HH, Yunus R. Experimental Analysis of Tribological Properties of Biolubricant with Nanoparticle Additive. *Procedia Engineering*. 68:152-7 (2013).
- [117] Peña-Parás L, Taha-Tijerina J, García A, Maldonado D, Nájera A, Cantú P, et al. Thermal Transport and Tribological Properties of Nanogreases for Metal-Mechanic Applications. *Wear*. 332-333:1322-6 (2015).
- [118] Kao M-J, Lin C-R. Evaluating the Role of Spherical Titanium Oxide Nanoparticles in Reducing Friction between Two Pieces of Cast Iron. *Journal of Alloys and Compounds*. 483:456-9 (2009).
- [119] Tan K-H, Awala H, Mukti RR, Wong K-L, Ling TC, Mintova S, et al. Zeolite Nanoparticles as Effective Antioxidant Additive for the Preservation of Palm Oil-Based Lubricant. *Journal of the Taiwan Institute of Chemical Engineers*. 58:565-71 (2016).

- [120] Song X, Zheng S, Zhang J, Li W, Chen Q, Cao B. Synthesis of Monodispersed ZnAl₂O₄ Nanoparticles and Their Tribology Properties as Lubricant Additives. *Materials Research Bulletin*. 47:4305-10 (2012).
- [121] Hernandez Battez A, Fernandez Rico JE, Navas Arias A, Viesca Rodriguez JL, Chou Rodriguez R, Diaz Fernandez JM. The Tribological Behaviour of ZnO Nanoparticles as an Additive to Pao6. *Wear*. 261:256-63 (2006).
- [122] Alves SM, Barros BS, Trajano MF, Ribeiro KSB, Moura E. Tribological Behavior of Vegetable Oil-Based Lubricants with Nanoparticles of Oxides in Boundary Lubrication Conditions. *Tribology International*. 65:28-36 (2013).
- [123] Ma S, Zheng S, Cao D, Guo H. Anti-Wear and Friction Performance of ZrO₂ Nanoparticles as Lubricant Additive. *Particuology*. 8:468-72 (2010).
- [124] He X, Xiao H, Choi H, Díaz A, Mosby B, Clearfield A, et al. A-Zirconium Phosphate Nanoplatelets as Lubricant Additives. *Colloids and Surfaces A: Physicochemical and Engineering Aspects*. 452:32-8 (2014).
- [125] Moshkovith A, Perfiliev V, Lapsker I, Fleischer N, Tenne R, Rapoport L. Friction of Fullerene-Like WS₂ Nanoparticles: Effect of Agglomeration. *Tribology Letters*. 24:225-8 (2006).
- [126] Henry CR. Morphology of Supported Nanoparticles. *Progress in surface science*. 80:92-116 (2005).
- [127] Huitink D, Zarrin T, Sanders M, Kundu S, Liang H. Effects of Particle-Induced Crystallization on Tribological Behavior of Polymer Nanocomposites. *Journal of Tribology*. 133:021603 (2011).

- [128] Huitink D, Kundu S, Park C, Mallick B, Huang JZ, Liang H. Nanoparticle Shape Evolution Identified through Multivariate Statistics. *The Journal of Physical Chemistry A*. 114:5596-600 (2010).
- [129] Joly-Pottuz L, Martin J, Dassenoy F, Belin M, Montagnac G, Reynard B, et al. Pressure-Induced Exfoliation of Inorganic Fullerene-Like WS₂ Particles in a Hertzian Contact. *Journal of Applied Physics*. 99:3524 (2006).
- [130] Joly-Pottuz L, Ohmae N. Carbon-Based Nanolubricants. *Nanolubricants*.93-147 (2008).
- [131] Tevet O, Von-Huth P, Popovitz-Biro R, Rosentsveig R, Wagner HD, Tenne R. Friction Mechanism of Individual Multilayered Nanoparticles. *Proceedings of the National Academy of Sciences*. 108:19901-6 (2011).
- [132] Rapoport L, Leshchinsky V, Lapsker I, Volovik Y, Nepomnyashchy O, Lvovsky M, et al. Tribological Properties of WS₂ Nanoparticles under Mixed Lubrication. *Wear*. 255:785-93 (2003).
- [133] Fischer A. Well-Founded Selection of Materials for Improved Wear Resistance. *Wear*. 194:238-45 (1996).
- [134] Rapoport L, Bilik Y, Feldman Y, Homyonfer M, Cohen S, Tenne R. Hollow Nanoparticles of WS₂ as Potential Solid-State Lubricants. *Nature*. 387:791-3 (1997).
- [135] Rapoport L, Nepomnyashchy O, Lapsker I, Verdyan A, Soifer Y, Popovitz-Biro R, et al. Friction and Wear of Fullerene-Like WS₂ under Severe Contact Conditions: Friction of Ceramic Materials. *Tribology Letters*. 19:143-9 (2005).

- [136] Joly-Pottuz L, Dassenoy F, Belin M, Vacher B, Martin J, Fleischer N. Ultralow-Friction and Wear Properties of If- WS₂ under Boundary Lubrication. *Tribology Letters*. 18:477-85 (2005).
- [137] Berman D, Erdemir A, Sumant AV. Graphene: A New Emerging Lubricant. *Materials Today*. 17:31-42 (2014).
- [138] Onodera T, Morita Y, Suzuki A, Koyama M, Tsuboi H, Hatakeyama N, et al. A Computational Chemistry Study on Friction of H-MoS₂. Part I. Mechanism of Single Sheet Lubrication. *The Journal of Physical Chemistry B*. 113:16526-36 (2009).
- [139] He X, Xiao H, Kyle JP, Terrell EJ, Liang H. Two-Dimensional Nanostructured Y₂O₃ Particles for Viscosity Modification. *Applied Physics Letters*. 104:163107 (2014).
- [140] Spear JC, Ewers BW, Batteas JD. 2d-Nanomaterials for Controlling Friction and Wear at Interfaces. *Nano Today*. 10:301-14 (2015).
- [141] Xiao H, Dai W, Kan Y, Clearfield A, Liang H. Amine-Intercalated A-Zirconium Phosphates as Lubricant Additives. *Applied Surface Science*. 329:384-9 (2015).
- [142] Sun L, Boo WJ, Sue H-J, Clearfield A. Preparation of A-Zirconium Phosphate Nanoplatelets with Wide Variations in Aspect Ratios. *New Journal of Chemistry*. 31:39-43 (2007).
- [143] He XL, Xiao HP, Choi HH, Diaz A, Mosby B, Clearfield A, et al. Alpha-Zirconium Phosphate Nanoplatelets as Lubricant Additives. *Colloid Surface A*. 452:32-8 (2014).
- [144] Xiao HP, Dai W, Kan YW, Clearfield A, Liang H. Amine-Intercalated Alpha-Zirconium Phosphates as Lubricant Additives. *Appl Surf Sci*. 329:384-9 (2015).

- [145] Pan J, Li M, Luo Y, Wu H, Zhong L, Wang Q, et al. Synthesis and Sers Activity of V_2O_5 Nanoparticles. *Applied Surface Science*. 333:34-8 (2015).
- [146] Hamrock BJ, Dowson D. Ball Bearing Lubrication: The Elastohydrodynamics of Elliptical Contacts. (1981).
- [147] Wills JG. Lubrication Fundamentals: Marcel Dekker Inc; 1980.
- [148] Spikes H. The History and Mechanisms of Zddp. *Tribol Lett*. 17:469-89 (2004).
- [149] Kim Y-J, Baik S-I, Bertolucci-Coelho L, Mazzaferro L, Ramirez G, Erdermir A, et al. Atom-Probe Tomography of Tribological Boundary Films Resulting from Boron-Based Oil Additives. *Scripta Materialia*. (2015).
- [150] Ma HB, Li J, Chen H, Zuo GZ, Yu Y, Ren TH, et al. Xps and Xanes Characteristics of Tribofilms and Thermal Films Generated by Two P- and/or S-Containing Additives in Water-Based Lubricant. *Tribology International*. 42:940-5 (2009).
- [151] Zhou SG, Wang LP, Xue QJ. Controlling Friction and Wear of Nc-Wc/a-C(Al) Nanocomposite Coating by Lubricant/Additive Synergies. *Surf Coat Tech*. 206:2698-705 (2012).
- [152] Nan F, Xu Y, Xu BS, Gao F, Wu YX, Tang XH. Effect of Natural Attapulgitic Powders as Lubrication Additive on the Friction and Wear Performance of a Steel Tribo-Pair. *Appl Surf Sci*. 307:86-91 (2014).
- [153] Cai Z-b, Meyer Iii HM, Ma C, Chi M, Luo H, Qu J. Comparison of the Tribological Behavior of Steel–Steel and Si_3N_4 –Steel Contacts in Lubricants with Zddp or Ionic Liquid. *Wear*. 319:172-83 (2014).

- [154] Fan KZ, Li J, Ma HB, Wu H, Ren TH, Kasrai M, et al. Tribological Characteristics of Ashless Dithiocarbamate Derivatives and Their Combinations with Zddp as Additives in Mineral Oil. *Tribology International*. 41:1226-31 (2008).
- [155] Totolin V, Minami I, Gabler C, Doorr N. Halogen-Free Borate Ionic Liquids as Novel Lubricants for Tribological Applications. *Tribology International*. 67:191-8 (2013).
- [156] Burkinshaw M, Neville A, Morina A, Sutton M. The Lubrication of Both Aluminium-Silicon and Model Silicon Surfaces with Calcium Sulphonate and an Organic Antiwear Additive. *Tribology International*. 67:211-6 (2013).
- [157] Wang S, Yue W, Fu ZQ, Wang CB, Li XL, Liu JJ. Study on the Tribological Properties of Plasma Nitrided Bearing Steel under Lubrication with Borate Ester Additive. *Tribology International*. 66:259-64 (2013).
- [158] Yu HL, Xu Y, Shi PJ, Wang HM, Wei M, Zhao KK, et al. Microstructure, Mechanical Properties and Tribological Behavior of Tribofilm Generated from Natural Serpentine Mineral Powders as Lubricant Additive. *Wear*. 297:802-10 (2013).
- [159] Ma H, Li J, Chen H, Zuo G, Yu Y, Ren T, et al. Xps and Xanes Characteristics of Tribofilms and Thermal Films Generated by Two P-and/or S-Containing Additives in Water-Based Lubricant. *Tribology international*. 42:940-5 (2009).
- [160] Taylor L, Spikes H. Friction-Enhancing Properties of Zddp Antiwear Additive: Part I—Friction and Morphology of Zddp Reaction Films. *Tribol T*. 46:303-9 (2003).

- [161] Joly-Pottuz L, Dassenoy F, Belin M, Vacher B, Martin JM, Fleischer N. Ultralow-Friction and Wear Properties of If-WS₂ under Boundary Lubrication. *Tribol Lett.* 18:477-85 (2005).
- [162] Pawlak Z, Kaldonski T, Pai R, Bayraktar E, Oloyede A. A Comparative Study on the Tribological Behaviour of Hexagonal Boron Nitride (H-Bn) as Lubricating Micro-Particles—an Additive in Porous Sliding Bearings for a Car Clutch. *Wear.* 267:1198-202 (2009).
- [163] Majumdar D, Chatterjee D, Ghosh S, Blanton T. X-Ray Photoelectron Spectroscopic Studies on Ceramic Composites Containing Ytria-Stabilized Zirconia and Alumina. *Appl Surf Sci.* 68:189-95 (1993).
- [164] Arfelli M, Mattogno G, Ferragina C, Massucci MA. Xps Characterization of Gamma-Zirconium Phosphate and of Some of Its Intercalation Compounds - a Comparison with the Alpha-Zirconium Phosphate Analogs. *J Includ Phenom Mol.* 11:15-27 (1991).
- [165] Martin JM. Antiwear Mechanisms of Zinc Dithiophosphate: A Chemical Hardness Approach. *Tribol Lett.* 6:1-8 (1999).
- [166] Zhou Q, Huang J, Wang J, Yang Z, Liu S, Wang Z, et al. Preparation of a Reduced Graphene Oxide/Zirconia Nanocomposite and Its Application as a Novel Lubricant Oil Additive. *RSC Advances.* 5:91802-12 (2015).
- [167] Dai W, Kheireddin B, Gao H, Liang H. Roles of Nanoparticles in Oil Lubrication. *Tribology International.* 102:88-98 (2016).

- [168] Kimura Y, Wakabayashi T, Okada K, Wada T, Nishikawa H. Boron Nitride as a Lubricant Additive. *Wear*. 232:199-206 (1999).
- [169] Dai W, Kheireddin B, Gao H, Kan Y, Clearfield A, Liang H. Formation of Anti-Wear Tribofilms Via A-Zrp Nanoplatelet as Lubricant Additives. *Lubricants*. 4:28 (2016).
- [170] Abdul-Kareem HK, Silveston P, Hudgins R. Forced Cycling of the Catalytic Oxidation of Co over a V_2O_5 Catalyst—I: Concentration Cycling. *Chemical Engineering Science*. 35:2077-84 (1980).
- [171] Liu J, Xia H, Xue D, Lu L. Double-Shelled Nanocapsules of V_2O_5 -Based Composites as High-Performance Anode and Cathode Materials for Li Ion Batteries. *Journal of the American Chemical Society*. 131:12086-7 (2009).
- [172] Chen Z, Augustyn V, Wen J, Zhang Y, Shen M, Dunn B, et al. High-Performance Supercapacitors Based on Intertwined Cnt/ V_2O_5 Nanowire Nanocomposites. *Advanced materials*. 23:791-5 (2011).
- [173] Li Y, Yao J, Uchaker E, Yang J, Huang Y, Zhang M, et al. Leaf-Like V_2O_5 Nanosheets Fabricated by a Facile Green Approach as High Energy Cathode Material for Lithium-Ion Batteries. *Advanced Energy Materials*. 3:1171-5 (2013).
- [174] Sathiya M, Prakash A, Ramesha K, Tarascon JM, Shukla A. V_2O_5 -Anchored Carbon Nanotubes for Enhanced Electrochemical Energy Storage. *Journal of the American Chemical Society*. 133:16291-9 (2011).

- [175] Takahashi K, Limmer SJ, Wang Y, Cao G. Synthesis and Electrochemical Properties of Single-Crystal V_2O_5 Nanorod Arrays by Template-Based Electrodeposition. *The Journal of Physical Chemistry B*. 108:9795-800 (2004).
- [176] Kumagai N, Tanno K, Nakajima T, Watanabe N. Structural Changes of Nb_2O_5 and V_2O_5 as Rechargeable Cathodes for Lithium Battery. *Electrochimica Acta*. 28:17-22 (1983).
- [177] Fateh N, Fontalvo G, Mitterer C. Tribological Properties of Reactive Magnetron Sputtered V_2O_5 and $V_n-V_2O_5$ Coatings. *Tribology Letters*. 30:21-6 (2008).
- [178] Erdemir A. A Crystal-Chemical Approach to Lubrication by Solid Oxides. *Tribology Letters*. 8:97-102 (2000).
- [179] Huang Y, Ibrahim AMM, Shi X, Radwan AR, Zhai W, Yang K, et al. Tribological Characterization of Nial Self-Lubricating Composites Containing V_2O_5 Nanowires. *Journal of Materials Engineering and Performance*. 25:4941-51 (2016).
- [180] Shen Q, Shi X, Yang K, Zou J, Zhai W, Huang Y. Tribological Performance of Tial Matrix Composites Containing Silver and V_2O_5 Nanowires at Elevated Temperatures. *RSC Advances*. (2016).
- [181] Zhang W, Zhou M, Zhu H, Tian Y, Wang K, Wei J, et al. Tribological Properties of Oleic Acid-Modified Graphene as Lubricant Oil Additives. *Journal of Physics D: Applied Physics*. 44:205303 (2011).
- [182] Maslar J, Hurst W, Bowers W, Hendricks J, Aquino M, Levin I. In Situ Raman Spectroscopic Investigation of Chromium Surfaces under Hydrothermal Conditions. *Applied Surface Science*. 180:102-18 (2001).

- [183] Oh SJ, Cook D, Townsend H. Characterization of Iron Oxides Commonly Formed as Corrosion Products on Steel. *Hyperfine Interactions*. 112:59-66 (1998).
- [184] Sousa P, Silvestre A, Popovici N, Conde O. Morphological and Structural Characterization of CrO₂/Cr₂O₃ Films Grown by Laser-Cvd. *Applied Surface Science*. 247:423-8 (2005).
- [185] Wei Q, Li Z, Zhang Z, Zhou Q. Facile Synthesis Of. Alpha.-Fe₂O₃ Nanostructured Films with Controlled Morphology. *Materials Transactions*. 50:1351-4 (2009).
- [186] De Faria D, Venâncio Silva S, De Oliveira M. Raman Microspectroscopy of Some Iron Oxides and Oxyhydroxides. *Journal of Raman Spectroscopy*. 28:873-8 (1997).
- [187] Tuinstra F, Koenig JL. Raman Spectrum of Graphite. *The Journal of Chemical Physics*. 53:1126-30 (1970).
- [188] XI J-h, XIE Y-j, YAO G-c, LIU Y-h. Effect of Additive on Corrosion Resistance of NiFe₂O₄ Ceramics as Inert Anodes. *Transactions of Nonferrous Metals Society of China*. 18:356-60 (2008).
- [189] AdabiFiroozjaei E, Koshy P, Sorrell CC. Effects of V₂O₅ Addition on the Corrosion Resistance of Andalusite-Based Low-Cement Castables with Molten Al-Alloy. *Journal of the European Ceramic Society*. 32:1463-71 (2012).
- [190] Santos E, Martinho H, Annes K, Leite R, Milazzotto M. Rapid and Noninvasive Technique to Assess the Metabolomics Profile of Bovine Embryos Produced in Vitro by Raman Spectroscopy. *Biomedical Optics Express*. 6:2830-9 (2015).

- [191] Zhu W, Wu Y, Leto A, Du J, Pezzotti G. Cathodoluminescence and Raman Spectroscopic Analyses of Nd-or Yb-Doped Y_2O_3 Transparent Ceramics. *The Journal of Physical Chemistry A*. 117:3599-607 (2013).
- [192] Li M, Feng Z, Ying P, Xin Q, Li C. Phase Transformation in the Surface Region of Zirconia and Doped Zirconia Detected by Uv Raman Spectroscopy. *Physical Chemistry Chemical Physics*. 5:5326-32 (2003).
- [193] He X, Chen Y, Zhao H, Sun H, Lu X, Liang H. Y_2O_3 Nanosheets as Slurry Abrasives for Chemical-Mechanical Planarization of Copper. *Friction*. 1:327-32 (2013).
- [194] Chen Y, Choi H, Liang H. Effects of Metal Ions on the Shape-Controlled-Hydrothermal Synthesis and Upconversion Luminescence Properties of $Y_4O(OH)_9NO_3/Y_2O_3: Er^{3+}, Yb^{3+}$. *Journal of Nanoscience and Nanotechnology*. 17:1870-6 (2017).
- [195] Zhang X, Roeffaers MB, Basu S, Daniele JR, Fu D, Freudiger CW, et al. Label-Free Live-Cell Imaging of Nucleic Acids Using Stimulated Raman Scattering Microscopy. *ChemPhysChem*. 13:1054-9 (2012).
- [196] Brozek-Pluska B, Musial J, Kordek R, Bailo E, Dieing T, Abramczyk H. Raman Spectroscopy and Imaging: Applications in Human Breast Cancer Diagnosis. *Analyst*. 137:3773-80 (2012).
- [197] Chen B-C, Sung J, Wu X, Lim S-H. Chemical Imaging and Microspectroscopy with Spectral Focusing Coherent Anti-Stokes Raman Scattering. *Journal of Biomedical Optics*. 16:021112--8 (2011).

- [198] Gosvami N, Bares J, Mangolini F, Konicek A, Yablon D, Carpick R. Mechanisms of Antiwear Tribofilm Growth Revealed in Situ by Single-Asperity Sliding Contacts. *Science*. 348:102-6 (2015).
- [199] Lee S-J, Lee S-H. Flow Field Analysis of a Turbulent Boundary Layer over a Riblet Surface. *Experiments in Fluids*. 30:153-66 (2001).
- [200] Munson BR, Young DF, Okiishi TH. Fundamentals of Fluid Mechanics. Wiley. 3 (1990).
- [201] Walsh MJ. Riblets as a Viscous Drag Reduction Technique. *AIAA journal*. 21:485-6 (1983).